Doctorate Dissertation

博士論文

Tsunami Source Estimation from Transoceanic Waveforms

(遠地波形による津波波源の推定)

A Dissertation Submitted for Degree of Doctor of Philosophy

July 2018

平成３０年７月博士（理学）申請

Department of Earth and Planetary Science, Graduate School of Science,

The University of Tokyo

東京大学大学院理学系研究科地球惑星科学専攻

Tungcheng Ho

何　東政

Abstract

In the present dissertation, we demonstrate the process of applying transoceanic tsunami waveforms in source inversion. First, we improve the existing phase correction method by incorporating the effects of ocean density stratification, the actual tsunami ray path, and the actual bathymetry. Second, we validate the improved method and the application of far-field tsunami data by the 2011 Tohoku earthquake tsunami. Third, we recover the source of the 1960 Chile earthquake by jointly inverting the near-field geodetic and tsunami data, and the newly available far-field tsunami data.

In Chapter 1, we review the tsunami inversion method and the previous method for phase correction. Due to the arrival time and waveform differences between observations and long-wave simulations after long distance traveling, the far-field data could not be used until the problems were solved by the phase correction method.

In Chapter 2, we further improve the accuracy of the existing phase correction method by adding the effects of ocean density stratification, actual ray path, and actual water depth. In our analysis, the existing method amounts to about 73% correction in our improved method. The new considered effects of ocean density stratification, actual ray path, and actual bathymetry, contribute to about 13%, 4.5%, and 9.5%, respectively.

Chapter 3 demonstrates that the improved method provides a more accurate estimate for the waveform inversion and forward prediction of far-field data. We also clarify the advantage and limit of far-field data. We perform single and multiple time window inversions for the 2011 Tohoku tsunami using far-field data corrected by different methods to investigate the initial sea surface displacement. The inversion results show that Green's functions corrected by improved method better fit observed waveforms. We also apply the improved method to forward simulation. Our results show good agreements between the observed and computed waveforms at both near-field and far-field tsunami gauges, as well as satellite altimeter data.

In Chapter 4, we recover the source feature of the 1960 Chile earthquake. With the improved phase correction method in Chapter 2 and Chapter 3, we solve the systematic arrival time problem. In addition, we apply the nonlinear inversion NOMAD (Nonlinear Optimization by Mesh Adaptive Direct Search) with the OTA (Optimal Time Alignment) method to correct the random arrival time difference problems caused by the instrumental problem, local effect, or other unknown response. Our results show that a rupture extended about 800 km with a width of about 150 km at the shallow region. Three asperities with slips of 33 m, 29 m, and 33 m appear at north, central, and south area, respectively. The estimated magnitude is about Mw 9.4. Our results also indicate that the south peak contributes to the large uplift of south coasts, e.g. Guamblin Island, and the later high amplitude tsunami wave phase at Honolulu.

Chapter 5 is the summary of this dissertation. Our study may provide a reference for using far-field tsunami data. We hope that the tsunami source research and forecast for transoceanic tsunami may be developed from our study.

Acknowledgements

I would like to express my sincere appreciation to the people supporting me during my doctoral journey.

First and foremost, I would like to heartily thank my supervisor Prof. Kenji Satake for his great support in research and school life. I have gotten his warm help since I was preparing the entrance exam. I sincerely appreciate his valuable advice in research discussions and paper writings. Even though he is busy sometimes, I can always get his kind help and instruction. I cannot achieve my doctorate without his earnest guidance and help. I would like to express my gratitude to him for conducting me the comprehensive study of geophysics and tsunami and providing me with many opportunities to attend conferences, which broadened my academic perspective.

I would like to express my deepest gratitude to Prof. Shingo Watada for his guidance and teaching for the most important part of my researches. His valuable suggestions provide significant help in my study. I would also like to greatly appreciate his patient instruction which enhanced my knowledge of geophysics and the basis of my study.

I am sincerely grateful to Prof. Koketsu for his valuable advice on my study in our seminars and his significant help in managing my defense. His kind help is essential for this dissertation. I also appreciate his careful checking and suggestions for this dissertation. I would like to convey my great thanks to Prof. Satoshi Ide for his valuable suggestions on my study and review for this dissertation. His valuable suggestions and comments indicated essential points for improving my study. I sincerely gratitude to Prof. Toshiyuki Hibiya for checking and pointed out the insufficient part of this dissertation. His comments provided a different point of views on my study. I sincerely thank to Prof. Shingo Yoshida for his advice to this dissertation. This dissertation becomes more complete with his advice and review.

I would like to greatly appreciate the kind encouragement and teaching from Prof. Hitoshi Kawakatsu. He encouraged me in my course and research and his class strengthened my background knowledge of seismology. My sincere thanks are extended to Prof. Takashi Furumura for his suggestions and comments in our seminars. His kind guidance encouraged me to join the Earthquake Research Institute. I would like to thank Prof. Hiroe Miyake for her questions and comments in the seminars which made me more understand my study. My thanks are extended to Prof. Takuto Maeda for his instructions and comments in the seminars which improved my background knowledge on my research. I am grateful to Prof. Hiroshi Tsuruoka for his management of the supercomputer EIC. My researches were performed on the EIC system of ERI.

I have to express my great thanks to Mr. Satoshi Kusumoto, who is my friend, classmate, and essential tutor. He gave me the greatest help in my life in Japan. He kindly helped me

with many life problems, communicate with companies, and provided me with accommodation in the very beginning few weeks in Japan. I am also very grateful to him for conveying important information from the school. His kind help made my life running smoothly in Japan. I would also like to thank Mr. Osamu Sandanbata for his help in the exam and daily life. He shared his note that helped my study and passed the entrance exam. I also deeply thank Dr. Aditya Riadi Gusman for his kind instructions and valuable suggestions and comments on my study. His suggestions notably improved my researches. My appreciation also goes to the guidance and many help from Iyan E. Mulia, who shared his experiences and knowledge with me. I am grateful to Dr. Mohammad Heidarzadeh, Dr. Md Jakir Hossen, Dr. Takeo Ishibe, and Dr. Tomoko Goto for sharing his knowledge and friendly help in school. I would also like to thanks to other members of Satake Laboratory and secretary Ms. Mayumi Takashima, for their help.

The supports from Earthquake Research Institute, Department of Earth and Planetary Science, and School of Science, the University of Tokyo are sincerely appreciated, especially for foreign student supporting center. The financial support from JASSO is also appreciated.

I am very grateful to the supervisor of my master degree, Prof. Tso-Ren Wu at the Institute of Hydrology and Ocean Sciences, National Central University, Taiwan. He taught me the essential knowledge of hydrodynamics and many skills about numerical simulation.

I would like to thank my parents and my brother for supporting my decision. With their warm consideration and support, I can concentrate on my study. Finally, I would like to express my gratitude to my wife Dr. Yikai Hsieh, who is also my partner in pursuing our doctoral degree in Japan. Thanks for always supporting me.

Table of Contents

Chapter 1 Introduction 1

1.1 Tsunami Simulation and Inversion 1

1.2 Arrival Time Discrepancy Problem and Solutions 1

1.2.1 Arrival Time Discrepancy at Transoceanic Tsunami 1

1.2.2 Solutions for Arrival Time Discrepancy 2

1.3 Applications of the Phase Correction Method 4

1.4 Objectives 4

Chapter 2 The Improved Phase Correction Method 7

2.1 The Phase Correction Method 7

2.1.1 Tsunami Normal Mode in A Self-Gravitating Elastic PREM 8

2.1.2 Other Factors Affecting Tsunami Propagation 9

2.1.3 Tsunami Propagation in 1-D Earth Models 9

2.2 Effect of Ocean Density Stratification 11

2.3 Great Circle and Actual Ray Path 13

2.4 Effect of Actual Bathymetry 16

2.5 Comparison of the Above Effects 17

2.6 Summary 20

Chapter 3 Validation: the 2011 Tohoku Earthquake Tsunami 21

3.1 Introduction 21

3.2 Data 23

3.2.1 Tsunami Waveform Data 23

3.2.2 Elevation Correction for GPS Buoy Data 27

3.2.3 Seafloor Deformation Correction for OBP Gauges 27

3.2.4 Satellite Altimeter Data 28

3.3 Tsunami Simulation and Inversion 28

3.3.1 Tsunami Simulation 28

3.3.2 Inversion Method 29

3.4 Inversion for the 2011 Tohoku Earthquake Tsunami 30

3.4.1 Single Time Window Inversion 30

3.4.2 Forward Prediction from Inverted Results 33

3.4.3 Multiple Time Window Inversion 39

3.4.4 Forward Prediction from Multiple Time Window Inverted Results 44

3.5 Conclusions 45

Chapter 4 Application: the 1960 Chile Earthquake Tsunami 47

4.1 Introduction 48

4.2 Data 50

4.2.1 Tsunami Waveform Data 50
4.2.2 Geodetic Data 51
4.3 Methods 53
4.3.1 Tsunami Simulation 53
4.3.2 Phase Correction 53
4.3.3 Inversion Method 54
4.4 Resolution Analysis 55
4.4.1 Resolution Test 55
4.4.2 Optimal Time Alignment (OTA) Test 59
4.5 Source Estimation for the 1960 Chile Earthquake 62
4.5.1 Joint Inversion of Tsunami Waveforms and Geodetic Data 62
4.5.2 The Slip Distribution 68
4.6 Conclusions 70
Chapter 5 Summary 71
Chapter 6 References 73

List of Tables

Table 3.1 Near-Field Tsunami Stations Used in The Present Study 25
Table 3.2 Far-Field Tsunami Stations Used in The Present Study 26
Table 3.3 Estimated Vertical Offsets for GPS Buoys 27

List of Figures

Figure 2.1. (a) Dispersion relations of the tsunami phase velocity computed for various spherical Earth models with an ocean layer of D = 4 km. The dashed line shows a nondispersive constant long-wave tsunami speed given by $\omega k = gD$, where g = 9.822 m/s^2. The dash-dotted line expresses the linear surface gravity wave given by $\omega k = gk\tanh kD$. All normal modes were computed with the physical dispersion defined in the PREM model. (b) Difference of the three modified PREM phase velocities relative to the RREM with a 4 km deep ocean. (Watada et al., 2014) 8

Figure 2.2. Averaged ocean density profile which is used for the ocean layer in the PREM ocean model. 12

Figure 2.3. (a) Phase velocity differences normalized by the ocean depth (= 4 km). (b) Phase velocity difference normalized by the long wave velocity ($gD0$)) at an ocean depth of 4 km. The blue line indicates the case with stratification, and the red line indicates the case without stratification. 12

Figure 2.4. (a) Least travel time from A (source) to the entire domain. (b) Least travel time from B (station) to the entire domain. (c) Map of $tA + tB$. The color bar indicates $log10tA + tB$ in minutes. The white line shows the ray path from A to B. The contour interval is 20 minutes. The gray star indicates the epicenter of the 2011 Tohoku earthquake, and the gray inverse triangle indicates station DART 51425. 15

Figure 2.5. (a) Normalized phase velocity differences as expressed in equation (2.2) for $D0$= 0.5 km and every 2.0 km from 2.0 km to 10.0 km. (b) Phase velocity difference normalized by long wave velocity ($gD0$) at different ocean depths. Note that the density stratification effect is included. 16

Figure 2.6. Observed waveform (black) and synthetic waveforms with different phase correction schemes (described in text) at DART 43412 off the west coast of Mexico for the 2011 Tohoku tsunami. The cyan line indicates the predicted long waves computed using the inverted result of the present study (described in section 5.2). The magenta line indicates the predicted waveform corrected using scheme 1. The waveform corrected using scheme 2 is indicated by the green line. The blue line indicates the waveform corrected using scheme 3. The red line indicates the waveform corrected by scheme 4. The effect of ocean density stratification is included in schemes 2, 3, and 4. 18

Figure 2.7. Travel time shifts corrected by the four schemes for all stations. (a) Travel time shifts of scheme 1 and scheme 4 relative to LLW. (b) The travel time shift of scheme 2 relative to scheme 1 ($\Delta tscheme2 - \Delta tscheme1$) shows the density stratification effect. (c) The travel time shift of scheme 3 relative to scheme 2 is caused by the distance difference $\Delta L = Lpath - LGC$. (d) The travel time shifts of scheme 4 relative to scheme 3 ($\Delta tscheme4 - \Delta tscheme3$) shows the difference between the actual bathymetry and a constant depth. The symbols indicate different average depths $Davg$ along the path. 19

Figure 3.1. (a) Entire simulation domain and (b) source area. In (a), the far-field stations are indicated by red dots, and the near-field stations are indicated by yellow dots. The magenta, orange, and yellow dashed paths indicate the satellite tracks of ENVISAT, Jason-1, and Jason-2, respectively. The solid line of each path shows the intervals used in the present study. In (b), the OBP-type stations, the GPS buoys, and the wave gauges are indicated by orange rectangles,

yellow triangles, and magenta circles, respectively. The black dots indicate the locations of unit sources, and the red line represents the trench. 24

Figure 3.2. Inverted sea surface displacements using Green's functions of different station groups and different correction schemes. (a)-(d) LLW without phase correction, (e)-(h) phase corrected using scheme 1, and (i)-(l) phase corrected using scheme 4. Each column shows a different station group. (a), (e), and (i) Near-field stations only, (b), (f), and (j) far-field stations only, (c), (g), and (k) near-field and far-field deep-ocean stations, and (d), (h), and (l) all stations. 32

Figure 3.3. NRMS misfit between observed and inverted synthetic waveforms for single and multiple time window inversion (described in section 5.3) using all stations. The single time window inverted sea surface displacements correspond to Figure 3.2d, Figure 3.2h, and Figure 3.2l, respectively. 33

Figure 3.4. Forward simulation results using the AIM and observed waveforms (black line) for (a) near-field stations and (b) far-field stations. The green lines indicate linear long waves. The blue lines indicate the synthetic waveforms corrected using scheme 1, and the red lines indicate the waveforms corrected using scheme 4. 36

Figure 3.5. NRMS misfits of forward predictions from four inverted models (NIM, FIM, DIM, and AIM). The green, blue, and yellow bars indicate the misfits of forward simulation at all stations, near-field stations, and far-field stations, respectively. 38

Figure 3.6. Travel time difference between observed and predicted waveforms for all stations. The predicted waveforms are computed using the AIM. The green circles indicate the differences between linear long waves and the observations. The blue circles indicate the differences between the synthetic waveforms corrected using scheme 1 and the observations. The red circles indicate the differences between synthetic waveforms corrected using scheme 4 and the observations. 38

Figure 3.7. Observed (black line) and synthetic tsunami wavefields obtained using the AIM along the tracks. The green lines indicate the synthetic wavefields of the LLW. The blue and red lines indicate the phase-corrected wavefields using schemes 1 and 4, respectively. The horizontal axes indicate the latitude along each track. 39

Figure 3.8. Multiple time window inversion results from (a) near-field stations where the waveforms are corrected by scheme 4. The bottom right plot in each figure shows the cumulative displacement of all time windows. 41

Figure 3.9. NRMS misfits of forward predictions from four multiple time window inverted models (MW-NIM, MW-FIM, MW-DIM, and MW-AIM). The green, blue, and yellow bars indicate the misfits of forward simulation at all stations, near-field stations, and far-field stations, respectively. 45

Figure 4.1. The entire computation domain. The red star shows the epicenter of the 1960 Chile earthquake. Red dots indicate far-field stations and yellow dots for near-field stations. 51

Figure 4.2. Distribution of unit sources (black dots), and geodetic data of coastal elevation positions (brown crosses) and leveling data along a highway (blue line). Red lines indicate the trenches. 52

Figure 4.3. The vertical displacement of (a) assumed checkerboard source and joint inversion result of (b) without assumed time shifts and (c) with assumed time shifts. 55

Figure 4.4. The synthetic geodetic data from the assumed source (black) and inversion (red). 56

Figure 4.5. The synthetic waveforms from assumed source (black) and inversion (red) at near-field. 56
Figure 4.6. The synthetic waveforms from assumed source (black) and inversion (red) at far-field. 57
Figure 4.7. The synthetic geodetic data from the assumed source (black) and inversion (red). 59
Figure 4.8. The synthetic waveforms from assumed source (black) and inversion (red) at near-field. The numbers at upper left corner indicate the random pre-assigned time shift (black) and predicted time shift by OTA (red). 60
Figure 4.9. The synthetic waveforms from assumed source (black) and inversion (red) at far-field. The numbers at upper left corner indicate the random pre-assigned time shift (black) and predicted time shift by OTA (red). 60
Figure 4.10. Estimated vertical displacements from the joint tsunami and geodetic data (a) without the OTA method, and (b) with the OTA method. 62
Figure 4.11. The observed (black) and synthetic (red) tsunami waveforms at near-field. The gray bars indicate the used time window for inversion. 63
Figure 4.12. The observed (black) and synthetic (red) tsunami waveforms at far-field. The gray bars indicate the used time window for inversion. 63
Figure 4.13. Coastal elevation and leveling data of observed (black) and synthetic (red). 65
Figure 4.14. The observed (black) and synthetic (red) tsunami waveforms at near-field. The gray bars indicate the used time window for inversion. The red numbers at lower left corner indicate the estimated time shift by OTA. 65
Figure 4.15. The observed (black) and synthetic (red) tsunami waveforms at far-field. The gray bars indicate the used time window for inversion. The red numbers at lower left corner indicate the estimated time shift by OTA. 66
Figure 4.16. The observed (black) and synthetic waveforms (dotted red line), and the synthetic waveforms from the north+central patch (blue) and south patch (green) at far-field. The blue bars indicate the used time window for inversion. 68
Figure 4.17. Slip distribution estimated from the inverted vertical displacement. The blue star shows the epicenter. The red lines represent the trenches. 69

List of Abbreviations and Acronyms

D	Ocean depth
DART	Deep-ocean Assessment and Reporting of Tsunamis
c	Phase velocity
E	Young's modulus
f	Coriolis coefficient
Far-field	Observations that travel time larger than 3 hours
g	Gravitational acceleration
GPS	Global Positioning System
η	Wave height
LLW	Linear Long Wave
L_{GC}	Great circle length
L_{path}	Actual ray path length
Mw	Moment magnitude scale
Near-field	Observations that travel time smaller than 3 hours
NOMAD	Nonlinear Optimization by Mesh Adaptive Direct Search
OBP	Ocean Bottom Pressure
OTA	Optimal Time Alignment
Ω	The angular frequency of the Earth’s rotation
P	Depth-integrated flow along longitude
PREM	Preliminary Reference Earth Model
Q	Depth-integrated flow along latitude
R	Earth’s radius
RMS	Root mean square
σ	Standard deviation
μ	shear modulus
ν	Poisson's ratio
ω	Angular frequency

Ψ_o	Initial wave phase
$\Delta\Psi$	Phase difference
φ	Longitude
θ	Latitude

Chapter 1 Introduction

1.1 Tsunami Simulation and Inversion

Tsunami waveforms have been widely used for source inversions since Satake (1987). The characteristic scale or the wavelength of a tsunami varies from tens to hundreds of kilometers, which is much larger than the ocean depth of a few kilometers. As such, the long wave theory has been adopted for tsunami propagation. In addition, when a tsunami propagates in a deep ocean, the ocean depth is much larger than the wave height. Thus, the equations can be linearized (Satake, 1995). This linear characteristic enables tsunami waveform inversion, which assumes that the observed waveforms are the superposition of simulated waveforms.

The tsunami waveforms simulated from assumed unit sources are used as the Green's functions for the waveform inversion to estimate the slip distributions (Gusman et al., 2012; Satake, 1987) or the initial sea surface displacements (Saito et al., 2010; Satake et al., 2005). The phase velocity of linear long waves depends only on the local water depth. Using global bathymetry data, e.g., Weatherall et al. (2015), the linear long wave is usually computed accurately.

1.2 Arrival Time Discrepancy Problem and Solutions

1.2.1 Arrival Time Discrepancy at Transoceanic Tsunami

Although tsunami simulations are usually accurate, especially travel time, systematic discrepancies of travel times between observed and synthetic waveforms at far-field stations have been reported since the tsunami triggered by the 1960 Chile earthquake (Imamura et al., 1987, 1990).

For the 2004 Indian Ocean tsunami, two bottom pressure gauges recorded tsunami waves 19 hours after the earthquake with delays of 10 min and 15 min relative to a simulation (Rabinovich et al., 2011; Rabinovich et al., 2017). In the 2010 Maule earthquake tsunami, ocean bottom pressure gauges, offshore GPS buoys in Japan, and Deep-ocean Assessment and Reporting of Tsunamis (DART) stations located in the north and west Pacific Ocean observed delays of up to 30 min compared with the predicted waveforms (Fujii & Satake, 2013; Kato et al., 2011; Saito et al., 2010). In addition to the travel time delay, a small depression preceding the leading wave was also found (Eblé et al., 2015; Rabinovich et al., 2013).

After the 2011 Tohoku earthquake, the tsunami waves propagated over the entire Pacific Ocean and were recorded by more than twenty far-field DART stations located off the coasts of Alaska, Hawaii, western North and South America, and Oceania. Simons et al. (2011) mentioned the disagreement of the tsunami first arrival time at DART stations close to Japan with distant DART stations located off the coasts of Alaska and the western USA. To solve this problem, they introduced a time shift for each of eight far-field DART stations in their joint inversion. Tang et al. (2012) noted the travel time errors between observation and their forecast for far-field stations. Watada et al. (2014) pointed out the systematic travel time delays of the 2010 Maule and 2011 Tohoku earthquake tsunamis, and a small depression before the leading wave is commonly observed only at far-field stations.

1.2.2 Solutions for Arrival Time Discrepancy

The factors that account for the travel time delay and preceding depression have been discussed and explained in previous studies.

Tsai et al. (2013) derived the tsunami phase velocity incorporating the static elastic Earth deformation and variable water density in approach of energy conservation. For the elastic Earth deformation effect (hereafter, elastic effect in this section), by solving the elasticity problem (eqn. (5) in Tsai et al., 2013), they derived the tsunami speed incorporated the elastic effect. In addition, they derived the tsunami speed incorporated the variable water density effect (eqn. (24) in Tsai et al., 2013) by solving the linearized momentum equation and continuity equation (eqn. (16) and (17) in Tsai et al., 2013).

Their result suggests a dispersive correction from the elastic effect and a non-dispersive correction from the variable water density effect. The elastic effect reduces the tsunami speed by 0.2%-1.0% as the wavelength increases from 200 km to 1000 km. The variable water density effect slows the tsunami by about 0.5% independent of tsunami wavelength.

Watada (2013) evaluated the effect of variable density by the compressibility effect of seawater and the density stratification effect separately. He derived a tsunami phase

velocity in a uniform density compressible ocean (eqn. (27) in Watada), which is identical to the one derived by normal mode tsunami computation of Okal (1982). This result was compared to the tsunami phase velocity derived for a density-stratified compressible ocean (eqn. (29) in Watada, 2013), which is identical to the result of Tsai et al. (2013). He explained the difference of those two estimates comes from the assumption of the ocean density profile.

His result shows that, for a 4 km deep ocean, the compressible homogeneous ocean reduces ~0.29% tsunami speed compared to incompressible homogeneous ocean, which is due to the elastic energy stored in compressible water. And the compressible density-stratified ocean reduces ~0.44% tsunami speed. He indicates the difference between those two ocean models shows the 0.15% is due to the density stratification mainly by the hydrostatic compression. A simple case of two-layer incompressible liquid with different density also shows the effect of stratified density (Stokes, 1880; Lamb, 1945). The case of two-layer, incompressible different density liquid, is shown in eqn. (31) and (32) in Watada (2013), which is equal to the one from Lamb (1945). With the assumption of long waves, the equation can be approximated to eqn. (35) in Watada (2013), which is equal to the one derived by Stokes (1880).

Following the work of Tsai et al. (2013), Allgeyer and Cummins (2014) extended and developed a shallow water equation model including the effect of elastic loading of the Earth and linear ocean density profiles. Their model reduced the travel time discrepancy between simulation and observation, and well predicted the tsunami arrival time at far-field. They concluded that the ocean stratification accounts for only the travel time delay and that the elastic loading effect accounts for the travel time delay and preceding depression. However, the effect of the gravitational potential change was not included in their model.

Using the normal mode theory for a spherically symmetric Earth model covered by an ocean layer (e.g., Watada & Kanamori, 2010), Watada et al. (2014) demonstrated that the elasticity of the Earth and ocean and the gravitational potential change associated with the tsunami motion cause the travel time delay and preceding depression. They also examined the effects of bathymetry data, grid size, governing equations (Boussinesq and shallow water equation), advection, bottom friction, Coriolis force and elliptic Earth, and showed that those effects are insignificant except elliptic Earth.

Rather than extending the tsunami normal mode theory to a laterally heterogeneous Earth model with actual bathymetry, they proposed a simple phase correction method that converts the computed waveforms of linear long waves into dispersive waveforms. By applying this method, the travel time delay between their synthetic and observed waveforms was greatly reduced. Their method also reproduced the preceding depression observed before the arrival of the first tsunami peak.

1.3 Applications of the Phase Correction Method

The phase correction method (Watada et al., 2014) has been applied to far-field data in tsunami source studies. Gusman et al. (2015) applied the phase correction in their slip inversion for the 2014 Iquique, Chile, earthquake. They noted that, with the phase correction, the far-field tsunami data can be used for tsunami waveform inversions. Yoshimoto et al. (2016) used the phase-corrected far-field DART data in the waveform inversion to study the slip distribution of the 2010 Chile Maule earthquake. They concluded that the slip distributions from the near-field DART and from the far-field DART were similar to that from all DART data. Gusman et al. (2016) used the phase correction method to simulate the dispersive propagation of the 2012 Haida Gwaii earthquake tsunami. They found that the dispersion effects on amplitude reduction are more significant for shorter wavelengths and that the average travel time delay is approximately 1 min per 1,300 km.

1.4 Objectives

In this study, we demonstrate the tsunami source estimation using transoceanic waveforms.

Tsunami observations are generally distributed onshore (e.g. tidal gauges, wave gauges, or buoys), or offshore (e.g. ocean bottom pressure gauges such as DART) in a moderate distance. For a tsunami event, the observations are usually one-side distributed. Tsunami source inversion usually suffers from data azimuthal problem except for some events with well-established observations, e.g. the 2011 Tohoku earthquake.

Like teleseismic waves, the transoceanic tsunami waves provide additional source information. With the explanation of arrival time discrepancy for transoceanic tsunami, the far-field data can be used in tsunami forecasting and source estimation.

In the present dissertation, we exploited the far-field tsunami data in source estimation. We improved the existing phase correction method and validated it the by the 2011 Tohoku earthquake tsunami. Then we applied the improved method to the 1960 Chile earthquake to estimate the source by the newly available tsunami data.

The structure of this dissertation is as follows:

- Chapter 2:
  To improve the existing phase correction method. We examined the existing phase correction method and improved it by adding the effects of water stratification, actual ray path, and actual depth. We then analyzed the improvement of each factor.
- Chapter 3:

The improved phase correction method had been validated by applying to the 2011 Tohoku earthquake tsunami. We applied the improved method to invert the source of the 2011 Tohoku earthquake tsunami. We analyzed the difference between the existing method and our improved method in different datasets (near-field, far-field, and all data).

- Chapter 4:
  We applied the improved phase correction to investigate the source of the 1960 Chile earthquake. The OTA method was also used to deal with the random arrival time discrepancy problems. We successfully reconstructed the tsunami waveforms and geodetic data, and the source of the 1960 Chile earthquake was well estimated.
- Chapter 5:
  The summaries of the above chapters are listed in Chapter 5.

Chapter 2

The Improved Phase Correction Method

In this chapter, we improved the existing phase correction method by incorporating the effects of ocean density stratification, the actual tsunami ray path, and actual bathymetry. The improved phase correction method accounted for almost all the travel time delay at far-field stations. The previously considered effects amounted to approximately 73% for correction of the travel time delay, while the ocean density stratification, actual ray path, and actual bathymetry, contributed to approximately 13%, 4.5%, and 9.5% on average, respectively.

2.1 The Phase Correction Method

The phase correction method proposed by Watada et al. (2014) is a very efficient method to produce synthetic tsunami waveforms for waveform inversions. In this method, the tsunami waveforms were first simulated by the linear long wave (LLW) theory using actual bathymetry. The simulated waveforms were then converted into dispersive waves. The phase of the computed tsunami waveform was corrected by the dispersion relation constructed from the tsunami normal modes, in which the tsunami waves were regarded as propagating dispersive surface gravity waves in the top fluid layer of a self-gravitating elastic preliminary reference Earth model (PREM). The effects of the elasticity of the Earth, seawater compressibility, and the gravitational potential change associated with the tsunami motion are included in the normal mode method. Thus, these effects can be included in the conversion.

2.1.1 Tsunami Normal Mode in A Self-Gravitating Elastic PREM

The normal mode theory includes the effects of the elasticity of the Earth and the ocean layer and the gravitational potential change caused by the tsunami motion. These effects slow down the tsunami phase velocity including long period and short period components. The dispersion relation of each effect was examined by Watada et al. (2014).

Figure 2.1a shows the tsunami phase velocity for various spherical Earth models in Watada et al. (2014). The black line in Figure 2.1a shows the dispersion curve computed for PREM, in which the top layer is a constant density ocean layer. The blue line shows the dispersion curve for the incompressible ocean layer in the PREM. The green line indicates the dispersion curve for ignored gravitational potential variation during tsunami motion. And the red line represents the dispersion for a rigid Earth.

The effects of elastic Earth, compressible ocean, and gravity potential change compared in Watada et al. (2014) are shown in Figure 2.1b. The ocean compressibility effect is nearly constant for the period longer than 1000 sec as shown by the blue line in Figure 2.1b. The ocean compressibility shows the largest effect when the period is shorter than ~2000 sec. However, when the period is longer than ~2000 sec, the elastic effect become the largest effect (red line in Figure 2.1b). The gravity potential change effect is larger than ocean compressibility as the period longer than ~5000 sec (green line in Figure 2.1b).

The dispersion in the long period explains the phase reversal before the leading wave. Figure 2.1b indicates that the dispersion in long period (>1000 sec) is mainly caused by the effect of elastic Earth, and then the gravity potential change effect.

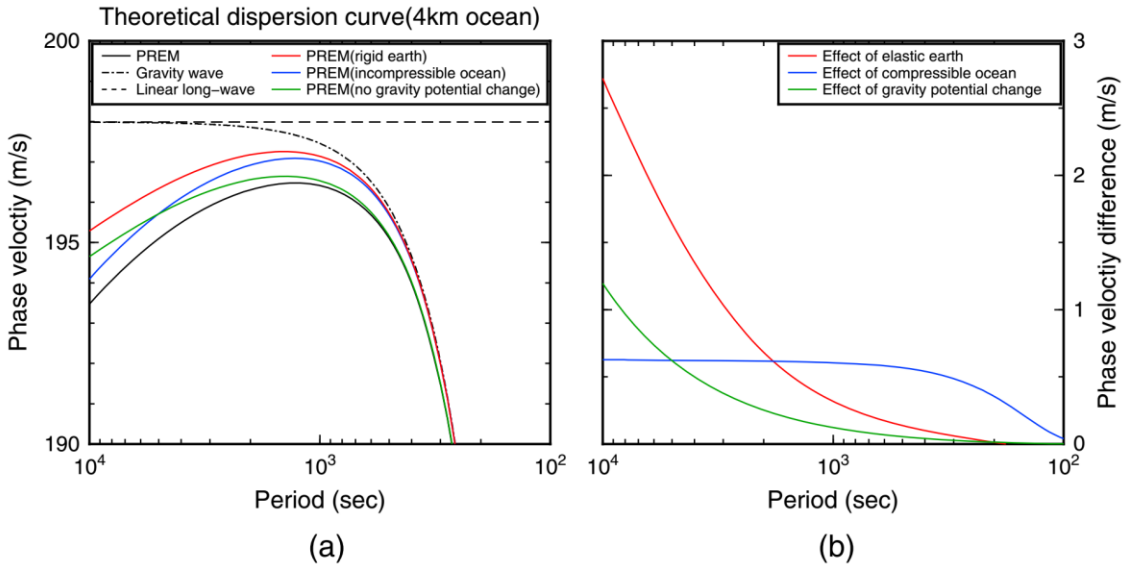

Figure 2.1. (a) Dispersion relations of the tsunami phase velocity computed for various spherical Earth models with an ocean layer of D = 4 km. The dashed line shows a nondispersive constant long-wave tsunami speed given by $\frac{\omega}{k} = \sqrt{gD}$, where g = 9.822 m/s^2. The dash-dotted line expresses the linear surface gravity wave given by $\frac{\omega}{k} =$

$\sqrt{\frac{g}{k}\tanh kD}$. All normal modes were computed with the physical dispersion defined in the PREM model. (b) Difference of the three modified PREM phase velocities relative to the RREM with a 4 km deep ocean. (Watada et al., 2014)

2.1.2 Other Factors Affecting Tsunami Propagation

Watada et al. (2014) comprehensively examined the effects of different bathymetry data, grid sizes, nonlinear effects, the Coriolis force effect, and the non-spherical gravity and shape of the Earth.

For bathymetry effect, they computed tsunami simulation using 1 arc-min bathymetry data ETOPO1 and GEBCO, respectively. The tsunami travel time differences between these two bathymetries are less than 1 minute. They also performed simulation using different grid size and confirmed that grid size does not cause the arrival time delay.

The tsunami delay is recorded by DART stations, which locates at deep ocean where nonlinear effects are very small and negligible (Liu, 2009). Nonlinear effects were also confirmed not the main reason for the tsunami delay (Figure S5 in Watada et al., 2014).

The Coriolis force is usually incorporated in large domain tsunami simulations, but the tsunami arrival delay was still observed (e.g., Saito, Matsuzawa, et al., 2010; Tang et al., 2012). Watada et al. (2014) compared the simulation with and without Coriolis force and indicated the Coriolis force effect on the tsunami arrival is insignificant (Figure S6 in Watada et al., 2014).

The major differences between elliptic Earth and spherical Earth are the radius and the gravity. Compare to the reference gravity in a spherical Earth, the elliptic Earth's gravity is smaller in low-latitude regions and larger in high-latitude regions. Watada et al. (2014) showed that combining those two factors (radius and gravity) causes a few minutes tsunami arrival delay (Figure S7 and S8 in Watada et al., 2014). However, the elliptic Earth cannot explain most observed arrival delay.

Ocean currents effect is also discussed in Watada et al. (2014). They pointed out ocean currents mainly move at a speed of about 10 cm/s, and the strong currents are concentrated at the upper ocean layer within few hundred meters and with widths of about 100 km. In addition, with the counterflow of the currents (Talley et al., 2011), the travel time anomalies caused by the currents would be reduced.

2.1.3 Tsunami Propagation in 1-D Earth Models

Following Watada et al. (2014), the tsunami waveform $u(x,t)$ observed at distance x and time t is expressed in the frequency domain as (equation 4.40 of Lay & Wallace, 1995):

$$u(x,t) = \frac{1}{\pi}\int_0^\infty \hat{u}(x,\omega)\cos\big(\Psi(x,\omega)\big)\,d\omega$$

where $\hat{u}(x,\omega)$ is the amplitude spectrum, and $\Psi(x,\omega)$ is the phase spectrum, which is expressed as

$$\Psi(x,\omega) = \omega t + \Psi_o - \frac{\omega x}{c(D(x),\omega)}$$

where $c(D(x),\omega)$ is the phase velocity of the tsunami propagating at x over an ocean of depth $D(x)$ with angular frequency ω, and Ψ_o is the initial phase of ω. Then, the phase difference $\Delta\Psi(dx,\omega)$ between linear long waves and dispersive waves is written over small distance dx as

$$\Delta\Psi(dx,\omega) = \frac{\Delta c(D(x),\omega)\omega}{gD(x)}\,dx, \tag{2.1}$$

where Δc is the phase velocity difference between linear long waves and dispersive waves, and $D(x)$ is the ocean depth at location x. To obtain equation (2.1), we assumed that $\Delta c \ll \sqrt{gD}$. For long waves, the velocity difference Δc normalized by the ocean depth is about constant for different depths (Figure 7 in Watada et al., 2014). The normalized phase velocity difference can then be approximated by the reference depth D_0 and phase velocity difference Δc_0

$$\frac{\Delta c(D(x),\omega)}{D(x)} = \frac{\Delta c_0(D_0,\omega)}{D_0}, \tag{2.2}$$

and equation (2.1) can be approximated as

$$\Delta\Psi(dx,\omega) = \frac{\Delta c(D(x),\omega)\omega}{gD(x)}\,dx = \frac{\Delta c_0(D_0,\omega)\omega}{gD_0}\,dx. \tag{2.3}$$

The phase velocity c_0 is calculated using the normal mode theory for the modified 1-D PREM, in which the top layer is the ocean layer with the reference depth $D_0 = 4$ km with constant density.

The phase shift $\Delta\Psi(x,\omega)$ from a source to a station is obtained as:

$$\Delta\Psi(x,\omega) = \int_0^x \Delta\Psi(dx,\omega) = \frac{\Delta c_0(\omega)\omega}{gD_0}L, \tag{2.4}$$

$$L = \int_0^x dx$$

where L is the distance from the epicenter to the station, which is approximated by the great circle length L_{GC} in Watada et al. (2014).

2.2 Effect of Ocean Density Stratification

The original PREM ocean model has a constant-density ocean layer. Based on the study of the density stratification effect on tsunami propagation speed (Watada, 2013), Watada et al. (2014) assumed the effect of water density stratification to be small and used a constant-density ocean in the PREM ocean model.

According to Watada et al. (2013), the ocean density stratification slows down the tsunami speed by 0.44% compared to the incompressible homogeneous ocean in a 4 km deep ocean. About 0.29% of the speed reduction is due to the ocean elasticity, which stores the energy in the water. And ~0.15% of the reduction is due to the water density stratification. An and Liu (2016) derived the theoretical solutions of the dispersion relation for the effects of water viscosity, ocean stratification, and numerical dispersion. For the stratification effect, they showed the tsunami phase velocity to be related with the density difference.

In the present study, we included the effect of the density stratification in the ocean layer of the 1-D PREM. The World Ocean Atlas 2009 (WOA09, Boyer et al., 2009) provides 1° × 1° world time-averaged depth profiles, which are composed of 33 vertical nodes from the sea surface to a depth of 5,500 meters. The ocean density was calculated using the pressure, salinity, and temperature data of WOA09 with the TEOS-10 toolbox (McDougall & Barker, 2011). We computed a mean vertical density profile by taking the average of the profiles in the domain represented in Figure 3.1a. The averaged vertical density profile (Figure 2.2) was adopted for the ocean layer in the PREM ocean model. For ocean deeper than 5,500 m, we calculated the densities following the ocean density relation of Watada (2013).

Figure 2.3a shows the normalized phase velocity difference given in equation (2.2) with and without adding ocean density stratification at a depth of 4 km. After adding the stratification effect, the normalized phase velocity difference is increased by approximately 0.1×10^{-3} (1/s) or approximately 16% on average over the period from 10 to 200 min. Figure 2.3b indicates the phase velocity reduction at a depth of 4 km. The average velocity reduction is approximately 1.1% without stratification and approximately 1.3% with stratification over the period from 10 to 200 min.

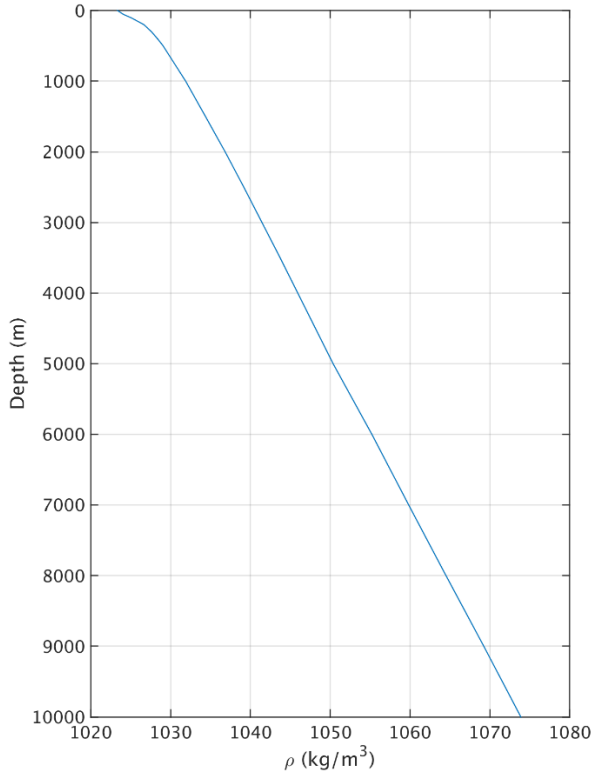

Figure 2.2. Averaged ocean density profile which is used for the ocean layer in the PREM ocean model.

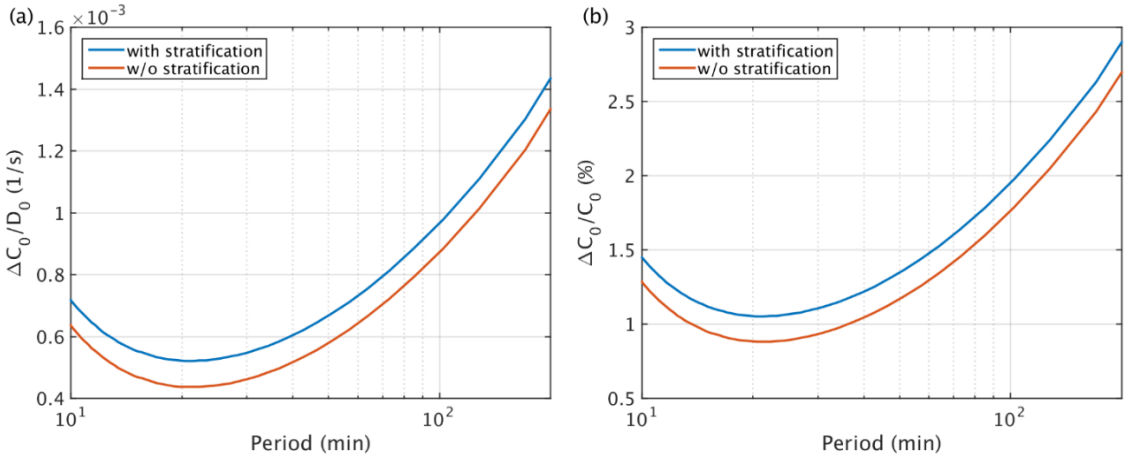

Figure 2.3. (a) Phase velocity differences normalized by the ocean depth (= 4 km). (b) Phase velocity difference normalized by the long wave velocity ($\sqrt{gD_0}$)) at an ocean depth of 4 km. The blue line indicates the case with stratification, and the red line indicates the case without stratification.

2.3 Great Circle and Actual Ray Path

In the present study, the approximation of the ray path length L_{GC} along the great circle in equation (2.4) was replaced by the actual ray path L_{path}. The great circle length is the minimum distance between two points on the earth. Approximation by the great circle length implies the phase difference $\Delta\Psi$ in Watada et al. (2014) is minimized. To attain the actual ray path, we traced the ray path from the epicenter to each station.

The ray tracing can be classified into two types of problem: initial value problem and boundary value problem. The initial value ray tracing, e.g. shooting method (Jacob 1970), is used to understand wave propagation and energy concentration (Woods & Okal, 1987; Satake 1988). To study the relationship between two points, the boundary value problem, e.g. bending method (Pereyra et al., 1980; Um & Thurber, 1987; Koketsu et al., 1998), is used for two-point tracing.

For two-point ray tracing for tsunami, we simply used the existing tsunami travel time calculator to achieve the tracing between two points. Assume there is a ray path of minimum travel time from the source (A) to the station (B), $\overline{AB}$. Then, according to Fermat's principle, this is the least travel time τ_{AB} from A to B. The reverse path from B to A is equal to that from A to B, i.e., $\overline{AB} = \overline{BA}$, and $\tau_{AB} = \tau_{BA} = T$.

The procedure used to find the ray path involves three steps. In the first step, we calculated the least travel times t_A and t_B from A and B, respectively, to the entire computation domain (Figure 2.4a and Figure 2.4b). Here, t_A and t_B were calculated using Tsunami Travel Time (TTT, Geoware), which calculates the travel time of the tsunami wave front for all accessible points on the map. The travel time from A to B is given by $t_A(B) = \tau_{AB} = T$, and, similarly, $t_B(A) = T$. Note that $t_A(A) = t_B(B) = 0$. Hence, for $t_A + t_B$ at point A, $t_A(A) + t_B(A) = T$, and for point B, $t_B(B) + t_A(B) = T$. Therefore, the minimum value of $t_A + t_B$, $min(t_A + t_B)$, is equal to T, such that

$$min(t_A + t_B) = T \tag{2.5}$$

is satisfied at the points along the actual ray path. In the second step, we calculated $t_A + t_B$ for the entire domain, as shown in Figure 2.4c. In the final step, we traced the path from B to A toward the direction about normal to the contour of t_A along the points with minimum values (white line in Figure 2.4c) and obtained the actual path between A and B.

To clarify the uncertainty of the ray tracing, we performed the reverse tracing to estimate the inconsistency. The average difference between the two path lengths (from B to A and from A to B) was approximately 0.05% for all the stations used herein, and the maximum difference was approximately 0.5%. The TTT assumes the traveling speed of the linear long waves. The phase velocity reduction of real tsunamis from the long wave speed is

very small in the characteristic period of an earthquake tsunami (Watada et al., 2014). Therefore, we assume that the ray path length for real tsunami is the same as that of long period waves.

The phase difference $\Delta\Psi$ between the actual ray path L_{path} and the great circle length L_{GC} on a constant-depth ocean is

$$\Delta\Psi_{path} - \Delta\Psi_{GC} = \frac{\Delta c_0(\omega)\omega}{gD_0}\Delta L, \qquad (2.6)$$
$$\Delta L = \left(L_{path} - L_{GC}\right).$$

The length of the actual ray path L_{path}, the great circle L_{GC}, and the length difference ΔL are listed in Tables 1 and 2. For far-field stations, differences of up to 500 km are estimated.

Note that we traced the two-point ray path under the linear long wave assumption. In linear lone wave assumption, the tsunami wave velocity depends only on the water depth and no wave dispersion is considered, so the ray paths are identical for waves in different frequencies.

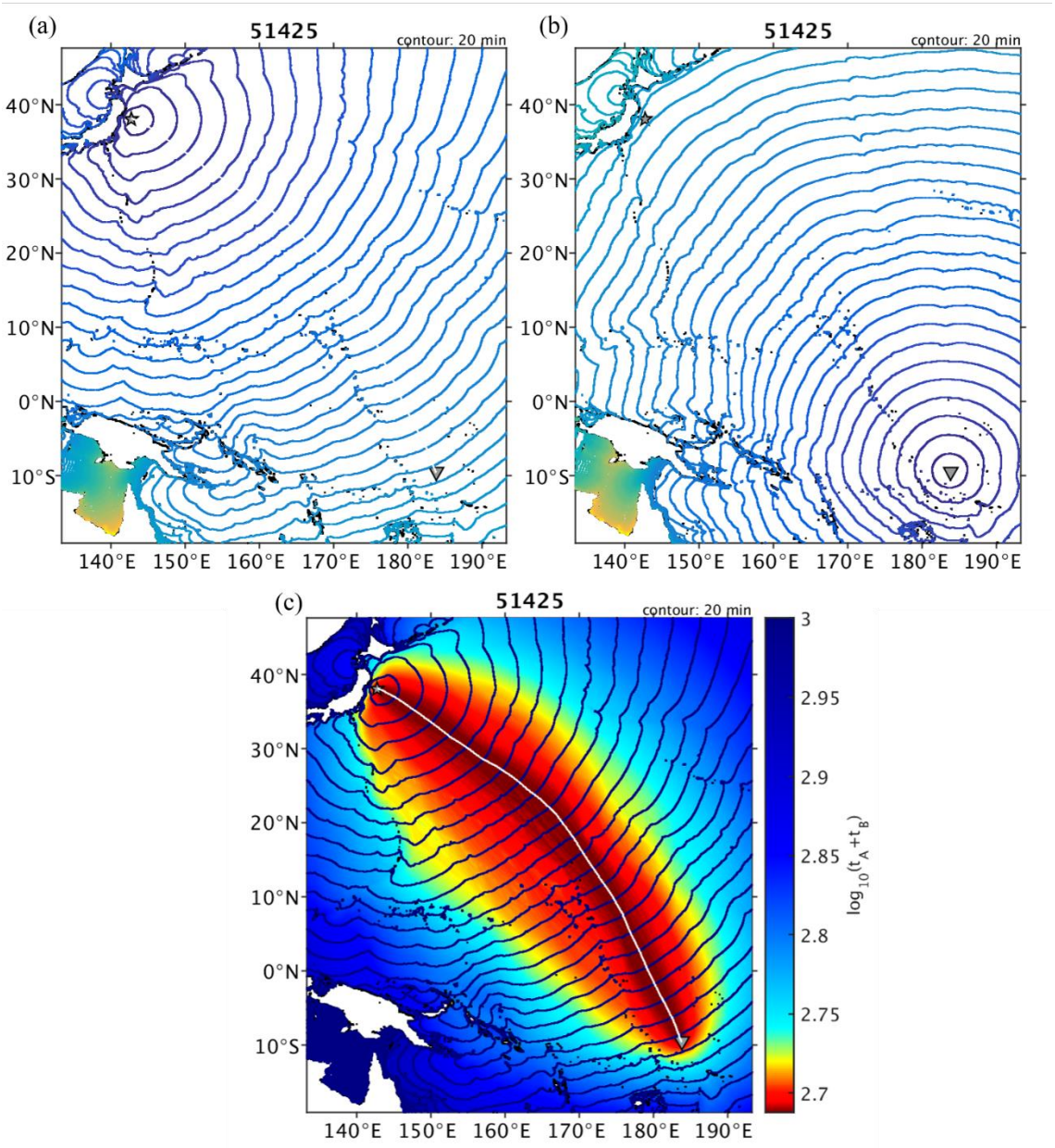

Figure 2.4. (a) Least travel time from A (source) to the entire domain. (b) Least travel time from B (station) to the entire domain. (c) Map of $t_A + t_B$. The color bar indicates $log_{10}(t_A + t_B)$ in minutes. The white line shows the ray path from A to B. The contour interval is 20 minutes. The gray star indicates the epicenter of the 2011 Tohoku earthquake, and the gray inverse triangle indicates station DART 51425.

2.4 Effect of Actual Bathymetry

In addition to the path length, the actual bathymetry along the path was also considered in our calculation. In Watada et al. (2014), the normalized phase velocity difference was approximated by the constant reference depth of 4 km, as expressed in equation (2.2). Figure 2.5a shows the normalized phase velocity differences in equation (2.2) for various depths. Figure 2.5b indicates the phase velocity reductions at different depths. Slight differences between the normalized depth and actual depth are accumulated as the distance increases. In the present study, the actual depth $D(x)$ along the ray path was first obtained. The bathymetry data combining the JTOPO30, M7000, and GEBCO_14 30″ was regarded as the actual bathymetry. Note that for depth $D(x)$ smaller than 100 m, $D(x)$ was set to 100 m. The phase difference over a small distance dx on actual bathymetry was calculated using equation (2.1). In equation (2.1), the phase velocity difference $\Delta c(D(x),\omega)$ for the actual depth $D(x)$ was interpolated from $\Delta c(D_i,\omega)$, where D_i = 0.1 km, 0.5 km, and every 1.0 km from 1.0 km to 10.0 km.

After we calculated the actual ray path, the phase difference $\Delta\Psi(x,\omega)$ for the actual depth along the ray path was obtained by integrating $\Delta\Psi(dx,\omega)$:

$$\Delta\Psi(x,\omega) = \int_0^x \Delta\Psi(dx,\omega)\,dx = \int_0^x \frac{\Delta c(D(x),\omega)\omega}{gD(x)}\,dx. \qquad (2.7)$$

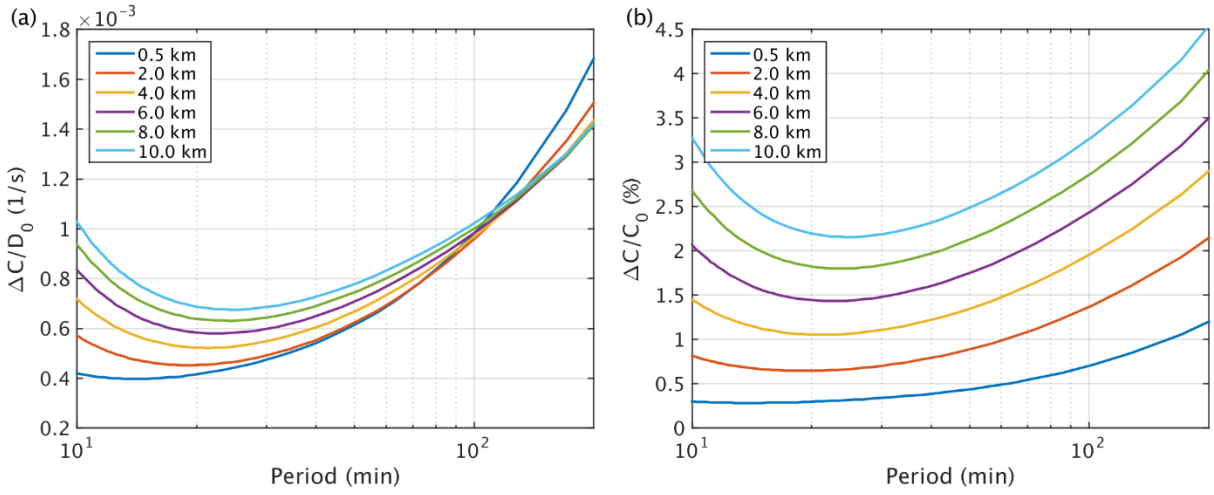

Figure 2.5. (a) Normalized phase velocity differences as expressed in equation (2.2) for D_0= 0.5 km and every 2.0 km from 2.0 km to 10.0 km. (b) Phase velocity difference normalized by long wave velocity ($\sqrt{gD_0}$) at different ocean depths. Note that the density stratification effect is included.

2.5 Comparison of the Above Effects

For the 2011 Tohoku tsunami, Figure 2.6 shows the observed waveform, the synthetic waveforms obtained by the LLW theory, and the waveforms obtained using four different phase correction schemes at station DART 43412 located approximately 11,000 km from the source region.

1. $\Delta\Psi(x,\omega) = \frac{\Delta c_0(D_0,\omega)\omega}{gD_0} L_{GC}$. Great circle length L_{GC} for reference depth D_0 = 4 km without ocean density stratification. (Same as Watada et al. (2014).)
2. $\Delta\Psi(x,\omega) = \frac{\Delta c_0(D_0,\omega)\omega}{gD_0} L_{GC}$. Great circle length L_{GC} for reference depth D_0 = 4 km with ocean density stratification.
3. $\Delta\Psi(x,\omega) = \frac{\Delta c_0(D_0,\omega)\omega}{gD_0} L_{path}$. Actual ray path L_{path} for reference depth D_0 = 4 km with ocean density stratification.
4. $\Delta\Psi(x,\omega) = \int_0^x \frac{\Delta c(D(x),\omega)\omega}{gD(x)} dx$. Actual ray path L_{path} for actual bathymetry $D(x)$ with ocean density stratification.

We determine the time shift by searching the shifted time, which shows the maximum correlation coefficient for the time interval used for inversion between a waveform and its reference waveform. We regard the time shift as positive when the waveform is late compared to its reference waveform. For scheme 1, the time shift of the corrected waveforms (magenta line) relative to the linear long wave (cyan line) is approximately 8.5 minutes. From scheme 1 to scheme 2, the ocean density stratification accounts for a time shift of approximately 1.5 minutes. The difference in length between the actual ray path and the great circle length for this station is 425 km, which was further reduced by approximately 0.4 minutes (time shift for scheme 3 relative to scheme 2). The time shift of scheme 4 relative to scheme 3 shows that replacing the phase correction at the reference ocean depth by that of actual bathymetry along the ray path accounts for an additional approximately 0.9 minutes.

The time shifts corrected by the four schemes for all stations are shown in Figure 2.7. Figure 2.7a shows the time shifts of schemes 1 and scheme 4 relative to the LLW for all stations. The time difference between schemes 1 and 4 increases with travel time.

Figure 2.7b shows the time shift caused by the density stratification effect by comparing the waveforms corrected using scheme 2 to that corrected using scheme 1. The density stratification effect slows by more than 1 minute when the travel time exceeds 8 hours and slows by more than 2 minutes when the travel time exceeds 17 hours.

Figure 2.7c indicates the travel time shifts caused by the increasing of distance (scheme 3 relative to scheme 2), which accounts for approximately 0.1 minutes per 100 km.

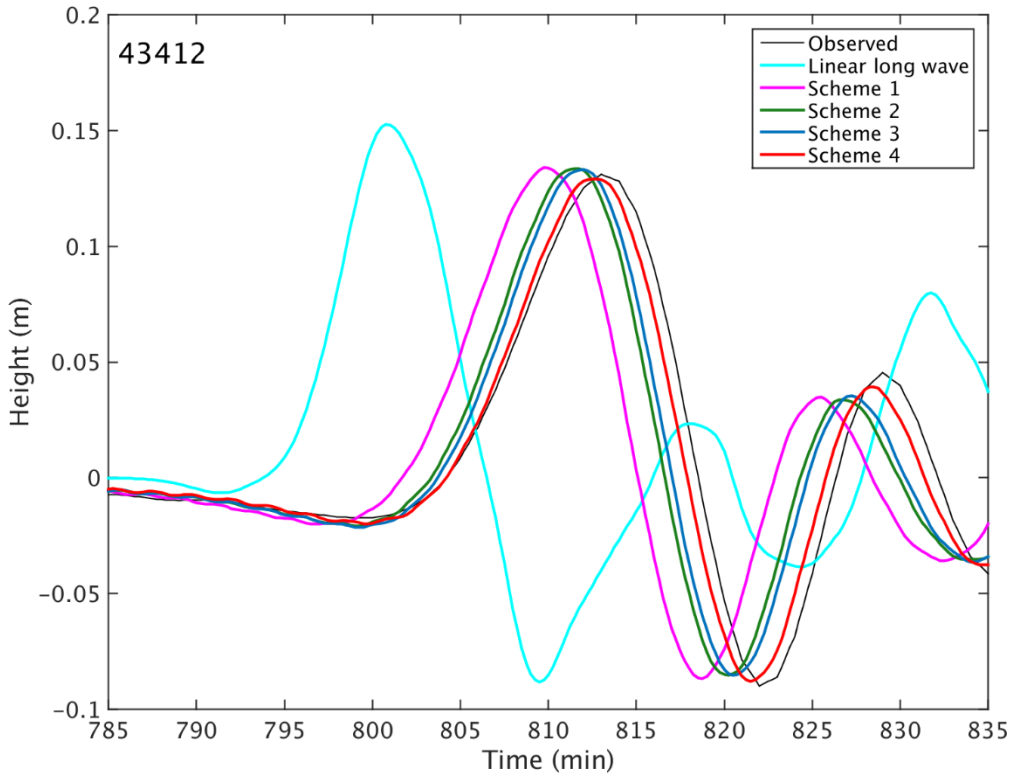

Figure 2.6. Observed waveform (black) and synthetic waveforms with different phase correction schemes (described in text) at DART 43412 off the west coast of Mexico for the 2011 Tohoku tsunami. The cyan line indicates the predicted long waves computed using the inverted result of the present study (described in section 5.2). The magenta line indicates the predicted waveform corrected using scheme 1. The waveform corrected using scheme 2 is indicated by the green line. The blue line indicates the waveform corrected using scheme 3. The red line indicates the waveform corrected by scheme 4. The effect of ocean density stratification is included in schemes 2, 3, and 4.

Figure 2.7d shows the travel time shift differences of the phase corrections of actual bathymetry relative to that of a reference depth of 4 km. The different symbols indicate different average depths along the path, D_{avg}. The Δt increases more rapidly with larger D_{avg}. For stations with D_{avg} smaller than 4 km, the travel time shifts are negative, which means that using a constant depth of 4 km overestimates the travel time delays for those stations.

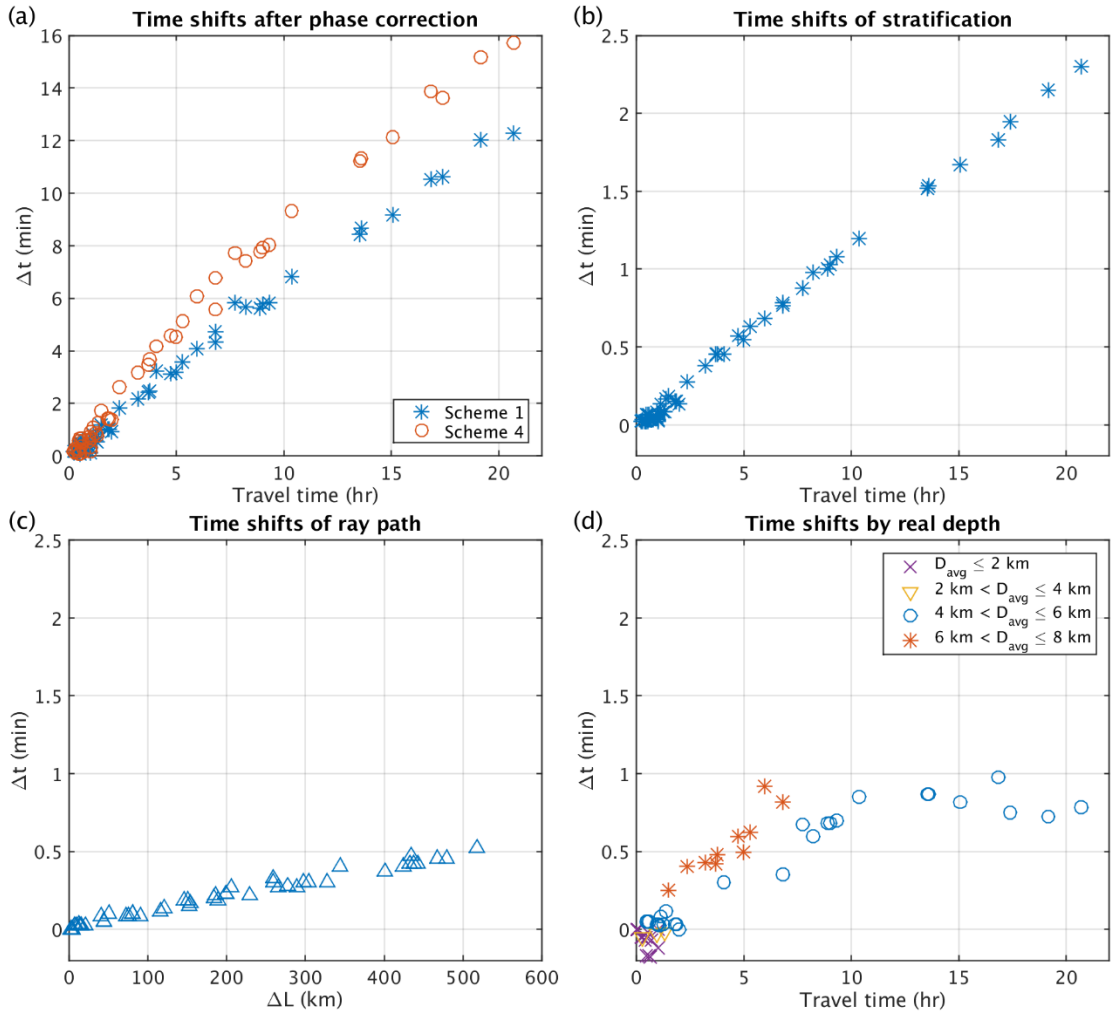

Figure 2.7. Travel time shifts corrected by the four schemes for all stations. (a) Travel time shifts of scheme 1 and scheme 4 relative to LLW. (b) The travel time shift of scheme 2 relative to scheme 1 ($\Delta t_{scheme2} - \Delta t_{scheme1}$) shows the density stratification effect. (c) The travel time shift of scheme 3 relative to scheme 2 is caused by the distance difference $\Delta L = \left(L_{path} - L_{GC}\right)$. (d) The travel time shifts of scheme 4 relative to scheme 3 ($\Delta t_{scheme4} - \Delta t_{scheme3}$) shows the difference between the actual bathymetry and a constant depth. The symbols indicate different average depths D_{avg} along the path.

For far-field stations, the effects of the elasticity of the Earth, seawater compressibility and the gravitational potential change associated with the tsunami motion, included in scheme 1, slowed the tsunami by approximately 6.6 min for a travel time of 10 hours (approximately 1.1%), compared to the synthetic waveforms of the LLW. The scheme 4 includes ocean density stratification, the actual path, and the actual bathymetry, and these effects slowed the tsunami by approximately 9 min for a travel time of 10 hours (approximately 1.5%).

The improvement from each factor was roughly estimated with the assumption that the improvement of each scheme is coming from the added factor. The scheme 2 reduced by 1.29%, the scheme 3 reduced by 1.36%, and the scheme 4 slowed ~1.5% travel time. By

subtracting the reduction of scheme 1 from scheme 2 (1.29%-1.1%), we obtained the stratification effect, which accounted for ~0.19%. And the difference between scheme 3 and scheme 2 was ~0.07% (1.36%-1.29%), which was due to the additional distance from the actual path. The effect of actual depth slowed ~0.14%, which was the difference between scheme 4 and scheme 3 (1.5%-1.36%).

Among the effects considered in the present study, the effects included in scheme 1 accounted for approximately 73% (1.1/1.5) on average of the travel time delay at far-field stations. The ocean density stratification accounted for ~13% on average. The actual ray path and actual bathymetry accounted for approximately 4.5% and 9.5%, respectively. Note that the effect of actual depth is larger with larger average depth. It means that this effect depends on the location of tsunami source and station locations.

2.6 Summary

In this chapter, we have improved the existing phase correction method and analyzed the contribution of each correction factor. The accuracy of the phase correction method was improved by the inclusion of the effects of ocean density stratification, the actual ray path, and actual bathymetry. The improved method (scheme 4) corrects the LLW travel time by approximately 1.5% on average at the far-field station, which improves the matches between the observed data and the synthetic waveforms. Our analysis showed that, for the case of the 2011 Tohoku earthquake tsunamis, approximately 73% of the correction is from the effects of elasticity of the Earth and the ocean, and the geopotential change associated with the tsunami motion, which was included in the original method of Watada et al. (2014). The ocean density stratification contributes to a correction of approximately 13%, which is the primary factor in the improvement. Moreover, corrections of approximately 4.5% and 9.5% are explained by the effects of the actual ray path and actual bathymetry, respectively.

Chapter 3
Validation: the 2011 Tohoku Earthquake Tsunami

Systemic travel time delays of up to 15 minutes relative to the linear long waves for transoceanic tsunamis have been reported. A phase correction method, which converts the linear long waves into dispersive waves, was previously proposed to consider seawater compressibility, the elasticity of the Earth, and gravitational potential change associated with tsunami motion. We improved the existing method in the previous chapter and applied the improved method to the 2011 Tohoku earthquake tsunami as a validation. We performed single and multiple time window inversions for the 2011 Tohoku tsunami using the far-field data (> 3 hours travel time) to investigate the initial sea surface displacement. The inversion result from only far-field data was similar to but smoother than that from near-field data and all stations, including a large sea surface rise, increasing toward the trench followed by a migration northward along the trench. For the forward simulation, our results showed good agreement between the observed and computed waveforms at both near-field and far-field tsunami gauges, as well as with satellite altimeter data. This chapter demonstrates that the improved method provides a more accurate estimate for the waveform inversion and forward prediction of far-field data.

3.1 Introduction

The 2011 Tohoku earthquake occurred at 5:46:18.1 UT on 11 March 2011 at epicenter 38°06.2′ N and 142°51.6′ E at depth 24 km (determined by JMA) with M 9.0. A huge slip (> 30 m) near the trench was estimated.

Ide et al. (2011) inverted 50 broadband GSN (Global Seismographic Network) stations and indicated that the rupture initiated in a deep rupture downdip-ward for about 40 sec, followed by an extensive shallow rupture toward the shallow region to the trench at 60 to 70 sec. Then a deep rupture spread lasted over 100 sec. The major rupture time was about 100 sec. The fault plane was 440 km long and 220 km wide, and the strong slip up to 30 m concentrated in the shallow region near the trench. They suggested two rupture modes: the shallow, strong, and quiet rupture; and deep rupture radiates high-frequency waves. These two modes reflected the friction characteristic at the subduction interface.

Shao et al. (2011) first conducted multiple double couple analysis then used broadband seismic data from IRIS and long period surface waves to constrain the spatiotemporal rupture history. Their preferred rupture model showed a rupture first propagated downdip and then rupture up-dip toward the trench generated an asperity up to 60 m slip after 45 sec. Following this near-trench rupture, two subevents occurred at 70-95 sec and after 110 sec. The most energy released from 45 sec to about 100 sec, and the rest until over 150 sec. The total seismic moment is 5.75×10^{22} Nm. Their result was consistent with the result of Ide et al. (2011).

Fujii et al. (2011) performed tsunami waveform inversion using OBP and GPS gauges to estimate the slip distribution. They indicated a large slip with more than 40 m appeared along the trench axis. Around the epicenter, their result showed large slip (28-34 m) at the epicenter and slip 9-23 m in the deep region. The total seismic moment was 3.8×10^{22} Nm.

Koketsu et al. (2011) constructed a unified source model by performed the joint inversion of teleseismic, strong motion, and geodetic datasets. Their result showed a rupture of about 480 km long and 150 km wide with seismic moment 3.8×10^{22} Nm. The source model indicated three main ruptures: first propagated to northeast and east at the origin time 50-60 sec; then propagated westward at 70-80 sec; finally propagated to southward at 90-100 sec. The first and second rupture resulted in bilateral rupture along dip direction, and the first and third rupture resulted in bilateral rupture along strike direction. Total rupture time was 120 sec. A tsunami inversion had also been carried out separately. For tsunami inversion, the extended 30 km (compared to the joint inversion) in width toward the trench is required to have to good agreement with the observed waveforms. The tsunami inversion showed a comparable seismic moment to the joint inversion, but the slip concentrated near the trench that did not hold the common feature of inversion from other data (teleseismic, strong motion, and geodetic) and joint inversion. This result suggested that the first rupture propagated toward the trench was tsunamigenic.

Satake et al. (2013) is the first one performing the multiple time window inversion using tsunami data. The rupture started from hypocenter with a small slip in the first 60 sec and spread out within 150 sec. This process was similar to the estimate from seismic waves

(e.g., Ide et al., 2011; or Shao et al., 2011). Then the large shallow slip propagated bilaterally along the trench after 180 sec. They estimated a large slip of ~25 m at deep region off Miyagi and a huge delayed slip of ~69 m in the shallow region near the trench at about 180 sec. The estimated seismic moment was 4.2×10^{22} Nm.

In the previous chapter, we replaced the great circle paths with the actual ray paths and the constant-depth ocean with actual bathymetry when calculating the phase correction along a tsunami ray path. In this chapter, we apply the improved method to single and multiple time window waveform inversions, which account for an instantaneous and a finite-time source process, respectively (Satake et al., 2013), to investigate the initial sea surface displacement of the 2011 Tohoku tsunamis using the near-field data, far-field data, and both near-field and far-field data (all stations).

3.2 Data

3.2.1 Tsunami Waveform Data

The huge slip triggered the strong tsunami. Run-ups of more than 30 m were observed in the Tohoku area (Mori et al., 2011). The 2011 Tohoku earthquake tsunami was recorded by numerous high-quality stations of diverse types spread throughout the entire Pacific Ocean, including off the coasts of Alaska, Hawaii, Oceania, and North and South America.

We used 28 near-field stations and 23 far-field stations for tsunami inversion and forward prediction, and the altimeter data from three satellites for forward prediction. The station locations are indicated in Figure 3.1, and the types and distances from the epicenter are listed in Tables 1 and 2. Only DART stations were used for far-field stations. For near-field stations (Figure 3.1), we used eight GPS buoys, 12 Ocean Bottom Pressure (OBP) type gauges, including five DART gauges, and eight wave gauges. Two OBP gauges were from the University of Tokyo and five were from the Japan Agency for Marine-Earth Science Technology (JAMSTEC). All of the GPS buoys and seven of the wave gauges were maintained by the Nationwide Ocean Wave information network for Ports and HArbourS (NOWPHAS). One wave gauge was operated by the Tokyo Electric Power Company. The station details have been summarized by Satake et al. (2013).

The observed data for all stations were resampled in 15-second intervals. We removed the tidal components by fitting a polynomial function and subtracting this function from the original records. In addition, we applied a three-minute low-pass filter to remove the high-frequency noise. Moreover, some stations located in the source area were influenced

by the seafloor deformation during the rupture process. Hence, we performed elevation corrections for these stations as described below.

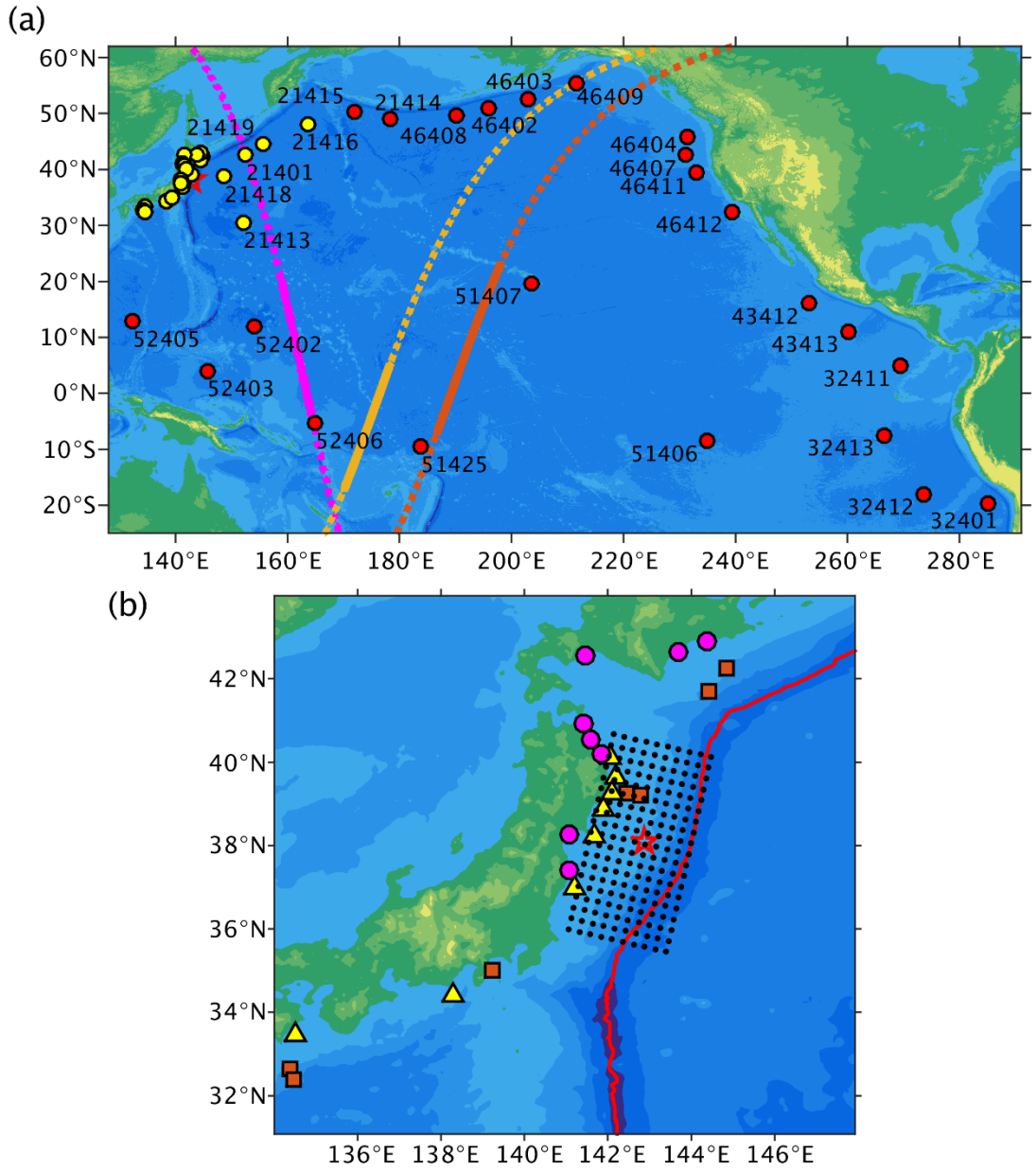

Figure 3.1. (a) Entire simulation domain and (b) source area. In (a), the far-field stations are indicated by red dots, and the near-field stations are indicated by yellow dots. The magenta, orange, and yellow dashed paths indicate the satellite tracks of ENVISAT, Jason-1, and Jason-2, respectively. The solid line of each path shows the intervals used in the present study. In (b), the OBP-type stations, the GPS buoys, and the wave gauges are indicated by orange rectangles, yellow triangles, and magenta circles, respectively. The black dots indicate the locations of unit sources, and the red line represents the trench.

Table 3.1 Near-Field Tsunami Stations Used in The Present Study

Station	Lon.	Lat.	Type	Depth (m)	L_{path}	L_{GC}	ΔL	$\frac{\Delta L}{L_{GC}}(\%)$	D_{avg}
21401	152.58	42.62	OBP	5,263	978.1	963.1	15.0	1.6	5,217.6
21413	152.12	30.53	OBP	5,825	1,217.1	1,196.8	20.3	1.7	5,755.4
21418	148.70	38.72	OBP	5,663	528.1	512.6	15.5	3.0	5,287.5
21419	155.74	44.46	OBP	5,292	1,400.1	1,284.6	115.5	9.0	6,786.8
21416	163.49	48.04	OBP	5,737	2,117.2	1,996.3	120.9	6.1	6,808.8
Iwate_N	142.07	40.12	GPS	125	275.1	234.2	41.0	17.5	1,537.7
Iwate_M	142.19	39.63	GPS	200	190.8	178.2	12.6	7.0	1,264.7
Iwate_S	142.10	39.26	GPS	204	147.8	144.1	3.7	2.6	1,136.3
Miyagi_N	141.89	38.86	GPS	160	122.1	118.5	3.7	3.1	960.4
Miyagi_M	141.68	38.23	GPS	144	105.8	102.8	3.0	2.9	832.6
Fukushima	141.19	36.97	GPS	137	269.8	193.6	76.2	39.4	2,275.7
Omaezaki	138.28	34.40	GPS	120	765.7	581.3	184.4	31.7	4,717.6
Tokushima Kaiyo	134.50	33.46	GPS	430	1,172.9	914.2	258.7	28.3	4,235.0
KPG2	144.85	42.24	OBP	2,210	533.1	489.4	43.7	8.9	5,825.4
KPG1	144.44	41.70	OBP	2,218	466.6	422.3	44.3	10.5	5,791.8
TM-2	142.44	39.25	OBP	1,013	133.0	131.1	1.9	1.5	1,312.1
TM-1	142.77	39.23	OBP	1,618	133.5	124.4	9.2	7.4	1,639.7
HPG1	139.22	35.00	OBP	1,176	678.6	473.3	205.3	43.4	5,241.0
MPG2	134.36	32.64	OBP	1,507	1,180.4	980.8	199.6	20.4	4,584.7
MPG1	134.48	32.39	OBP	2,308	1,176.3	991.0	185.3	18.7	4,637.1
Kushiro Port	144.40	42.91	Wave	50	620.9	549.1	71.8	13.1	5,111.9
Tokachi	143.69	42.65	Wave	23	590.9	510.7	80.2	15.7	4,766.9
Tomakomai Port	141.45	42.54	Wave	50.7	658.0	507.2	150.8	29.7	3,821.0
Mutsuogawara Port	141.40	40.93	Wave	43.8	535.7	336.9	198.8	59.0	3,596.9
Hachinohe Port	141.57	40.56	Wave	27.7	374.9	293.9	81.1	27.6	1,550.0
Kuji Port	141.86	40.22	Wave	49.5	301.5	250.6	50.9	20.3	1,449.0
Sendai New Port	141.07	38.25	Wave	21.3	161.7	158.0	3.7	2.3	561.2
Fukushima-1	141.05	37.41	Wave	C	184.3	176.3	8.0	4.5	634.6

Note. The station type is indicated in the "Type" column. The L_{path} and L_{GC} columns show the distances (km) from the epicenter to each station of the minimum travel time path and the path along the great circle, respectively. The ΔL column shows the distance difference (km) between L_{path} and L_{GC} ($\Delta L = L_{path} - L_{GC}$), and the $\frac{\Delta L}{L_{GC}}(\%)$ column shows the distance difference percentage with respect to the great circle distance.

The D_{avg} column shows the spatial average depth (m) along the path. Note that DART gauges are regarded as OBP gauges. The water depths of DARTs are from NOAA, and the other depths are from Satake et al. (2013) (C: coastal point).

Table 3.2 Far-Field Tsunami Stations Used in The Present Study

Station	Lon.	Lat.	Type	Depth (m)	L_{path}	L_{GC}	ΔL	$\frac{\Delta L}{L_{GC}}$(%)	D_{avg}
21414	178.25	48.94	OBP	5465	3,250.1	3,061.6	188.5	6.2	6,373.5
21415	171.85	50.18	OBP	4710	2,801.9	2,647.7	154.2	5.8	6,471.6
32401	285.19	-19.55	OBP	4799	16,262.0	15,862.0	400.0	2.5	4,958.4
32411	269.35	4.95	OBP	3166	13,246.0	12,728.0	518.0	4.1	5,102.3
32412	273.61	-17.99	OBP	4325	15,083.0	14,779.0	304.0	2.1	4,988.0
32413	266.50	-7.40	OBP	3893	13,770.0	13,442.0	328.0	2.4	5,012.4
43412	253.00	16.03	OBP	3232	11,011.0	10,586.0	425.0	4.0	5,304.3
43413	260.14	11.07	OBP	3,404	11,997.0	11,529.0	468.0	4.1	5,157.2
46402	195.99	51.07	OBP	4,719	4,616.0	4,338.5	277.5	6.4	6,500.1
46403	203.08	52.65	OBP	4,513	5,157.5	4,812.6	344.9	7.2	6,540.5
46404	231.23	45.86	OBP	2,738	7,449.0	6,970.4	478.6	6.9	5,774.3
46407	231.10	42.54	OBP	3,266	7,574.2	7,137.3	436.9	6.1	5,722.5
46408	190.15	49.62	OBP	5,379	4,191.8	3,925.5	266.3	6.8	6,449.0
46409	211.51	55.30	OBP	4,189	5,756.5	5,322.6	433.9	8.2	6,462.2
46411	233.00	39.33	OBP	4,259	7,899.6	7,457.1	442.5	5.9	5,681.0
46412	239.44	32.46	OBP	3,717	8,796.7	8,364.2	432.5	5.2	5,642.5
51406	234.97	-8.48	OBP	4,449	11,012.0	10,782.0	230.0	2.1	5,268.4
51407	203.49	19.62	OBP	4,682	6,398.8	6,139.9	258.9	4.2	5,245.5
51425	183.77	-9.50	OBP	4,979	6,944.4	6,791.6	152.8	2.2	5,688.2
52402	154.11	11.88	OBP	5,861	3,413.5	3,125.1	288.4	9.2	7,123.6
52403	145.60	4.03	OBP	4,431	4,100.7	3,802.6	298.1	7.8	6,906.2
52405	132.33	12.88	OBP	5,923	3,140.5	2,994.1	146.4	4.9	5,893.0
52406	165.00	-5.29	OBP	1,798	5,436.4	5,345.1	91.3	1.7	5,310.0

Note. The columns are the same as for Table 1.

3.2.2 Elevation Correction for GPS Buoy Data

For the GPS buoys located close to the source area, the observed data were affected by the coseismic deformation on land. GPS buoys were deployed approximately 20 km offshore along the coasts at depths of 100 m to 400 m. The wave heights were obtained by measuring the relative position of the buoy with respect to a reference GPS station, which was located on land and near the coast (Kato et al., 2011). Based on GPS Earth Observation Network System (GEONET) observations, the 2011 Tohoku earthquake caused large coseismic deformation in northeast Japan (Nishimura et al., 2011; Ozawa et al., 2012). The coseismic vertical movement of the reference GPS stations led to a vertical offset for the tsunami observation. According to Kawai et al. (2012), five GPS buoys showed a higher mean tide anomaly after the earthquake, varying from 0.25 to 0.95 m. These offsets were adopted by Satake et al. (2013). In the present study, we removed the deformation effect according to the estimation by Kawai et al. (2012). The estimated relative uplifts of the five GPS buoys are listed in Table 3.

Table 3.3 Estimated Vertical Offsets for GPS Buoys

Station	Iwate M	Iwate S	Miyagi N	Miyagi M	Fukushima
Offset (m)	0.24	0.54	0.66	0.95	0.38

3.2.3 Seafloor Deformation Correction for OBP Gauges

The OBP gauges located at the source area were either uplifted or lowered by the permanent seafloor deformation, which affected the recorded waveforms. In this case, the observations include both sea surface variation and seafloor deformation, which is different from the numerical simulations that calculate only the sea surface variations. In order to accurately estimate the tsunami source in waveform inversion, Tsushima et al. (2012) incorporated the effect of permanent seafloor deformation into the Green's functions for the OBP gauges located in the source area. By assuming an infinite rupture velocity of the faulting, the relation between the observed waveform of the OBP gauge and the initial sea surface displacement was expressed by a modified two-term Green's function, i.e., the original Green's function and a correction term for water depth change following permanent seafloor deformation.

In the 2011 Tohoku earthquake, two OBP gauges, TM-1 and TM-2, were in the source area, and the observed waveforms were affected by the permanent seafloor deformation. In the present study, we used the initial sea surface displacement as the initial condition to compute the Green's functions used in tsunami inversion (details are shown in section

3.3), and, following the method of Tsushima et al. (2012), the correction term in the Green's function was given by the initial sea surface displacement. The initial displacement $I_i(\mathbf{x}_j)$ in equation (34) in Tsushima et al. (2012) is given by equation (3.4) in section 3.3.2 in the present study.

3.2.4 Satellite Altimeter Data

After the 2011 Tohoku earthquake, three satellites passed the Pacific Ocean and observed the tsunami propagation through altimeters. The satellite tracks are shown in Figure 3.1a. The National Aeronautics and Space Administration and Centre National d'Études Spatiales (NASA-CNES) Jason-1 passed over and observed the tsunami on pass 147 of cycle 338 about 7.5 hours after the earthquake, and the NASA-CNES Jason-2 passed over and observed the tsunami on pass 21 of cycle 99 about 8.3 hours after the earthquake. The European Space Agency (ESA) ENVISAT observed the tsunami on orbit 210 of cycle 100 about 5.3 hours after the earthquake.

The tsunami waves observed by altimeters were recorded as the sea surface height anomaly (SSHA), which includes many different effects, such as tides, ocean current, and so on. To extract the tsunami signals, we used the averaged SSHA from the previous and next cycles as the reference. Since the sampling points along the tracks differ slightly between cycles, we applied the moving average method for distances of about 500 km along the tracks and interpolated them to the same sampling points. The tsunami wavefields were obtained by subtracting the reference SSHA from the observations. The satellite altimeter data were used only in forward simulation for validating the estimated tsunami source models and the improved method.

3.3 Tsunami Simulation and Inversion

3.3.1 Tsunami Simulation

We computed the tsunami waveforms by solving the linear shallow water equations in spherical coordinates:

$$\frac{\partial \eta}{\partial t} = -\frac{1}{R\sin\theta}\left[\frac{\partial P}{\partial \varphi} + \frac{\partial (Q\sin\theta)}{\partial \theta}\right] \tag{3.1}$$

$$\frac{\partial P}{\partial t} = -\frac{gD}{R\sin\theta}\frac{\partial \eta}{\partial \varphi} - fQ \tag{3.2}$$

$$\frac{\partial Q}{\partial t} = -\frac{gD}{R}\frac{\partial \eta}{\partial \theta} + fP, \tag{3.3}$$

where η is the wave height, D is the water depth, t is time, R is Earth's radius, P and Q are the depth-integrated flow along longitude φ and latitude θ, respectively, f is the Coriolis coefficient (= $2\Omega cos\theta$), and Ω is the angular frequency of the Earth's rotation. Equation (3.1) is the continuity equation, and equations (3.2) and (3.3) are the horizontal momentum equations in spherical coordinates. We used the JAGURS finite difference solver (Baba et al., 2015) but excluded the nonlinear and dispersion terms.

We used a 1' grid bathymetry with domain 128°E-69°W (291°E) and 25°S-62°N (Figure 3.1a) for tsunami computation. The bathymetry was resampled from the data of GEBCO_14 (Weatherall et al., 2015) 30'' grids, except for the area around Japan. For the area around Japan, the bathymetry grid was sampled from the data of JTOPO30 and M7000, which was provided by the Marine Information Research Center (MIRC). The M7000 data are the digitized contours covering the domain of 135°E-145°E and 35°N-40°N, and the JTOPO30 data are 30'' grids covering the domain of 128°E-150°E and 18°N-48°N. Since the domain of M7000 is also covered by JTOPO30, the overlapping area was resampled based on the grids created from M7000.

3.3.2 Inversion Method

Initial sea surface displacement may be triggered by both seismic and non-seismic phenomena. Hence, in the present study, we consider the displacement on the sea surface instead of the slip on a fault. Since the detailed parameters on a fault plane are not required, the Green's functions can be pre-computed in advance. To estimate the spatial and temporal change of the initial sea surface displacement, single and multiple time window inversions were implemented on the 2011 Tohoku tsunami using the far-field and near-field data.

We set 190 unit sources over the source area based on the location of the epicenter and the dimension from Satake et al. (2013). The unit source is a two-dimensional Gaussian sea surface displacement with the characteristic length $\sigma = 8'$. For the *j*th unit source located at (φ_j, θ_j), the sea surface displacement η_j is expressed as follows:

$$\eta_j(\varphi, \theta) = exp\left[-\frac{(\varphi - \varphi_j)^2 + (\theta - \theta_j)^2}{2\sigma^2}\right]. \tag{3.4}$$

The interval between the two unit sources is $16'$. The locations of the unit sources are indicated by the black dots in Figure 3.1b.

The simulated waveforms for the unit sources given as the initial conditions with a rise time of 30 seconds were used as the Green's functions. Since the near-field wave amplitude (few meters) is much larger than the far-field wave amplitude (few centimeters), we normalized the waveforms by multiplying the observed waveform and the Green's functions for each station by the weight w_i. For the ith station, the weight w_i is the inverse RMS value of the observed waveform b_i. $\frac{1}{w_i} = \sqrt{\frac{\int_0^\gamma [b_i(t)]^2 dt}{\gamma}}$, where b_i is the observed waveform at the ith station, and γ is the data length. We allow negative solutions of the initial sea surface displacement.

For the single time window inversion, the rupture on the source area is assumed to be instantaneous. We solved the following observation equation using the least squares method:

$$\begin{bmatrix} \mathbf{b} \\ \mathbf{0} \end{bmatrix} = \begin{bmatrix} \mathbf{G} \\ \alpha \mathbf{I} \end{bmatrix} \boldsymbol{X}^{\boldsymbol{T}} \tag{3.5}$$

where $\mathbf{b}$ $(= w_i b_i)$ is the column vector of the observed waveforms b_i at the ith station weighted by w_i, $i = 1\ to\ N$, where N is the number of stations; $\boldsymbol{X} = [x_j]$ is the unknown raw vector of the height for the jth unit source, $j = 1\ to\ M$, where M is the number of unit sources; $\mathbf{G}$ is the matrix of Green's functions g_{ij} weighted by w_i; $\mathbf{I}$ is the identity matrix for damping, and α, which is set to 1 in the present study, is the weighting factor for the identity matrix. To obtain a stable solution, we added the damping for the solutions using an identity matrix, but no smoothing was used.

For the multiple time window inversion, following Satake et al. (2013), we used five time windows and set the time window to $\Delta t = 30$ seconds. The shifted time for the jth unit source at the kth time window, $k = 1$ to 5, is $t_j^k = (k-1)\Delta t + \frac{R_j}{V}$, where R_j is the shortest distance between the epicenter and the edge of 1/10 the maximum height of the jth unit source. The rupture velocity V is set as 2.0 km/s. In equation (3.5), $\boldsymbol{X}$ is $[x_{jk}]$, and $\mathbf{G}$ is given by $w_i g_{ijk}$, where g_{ijk} for $k = 1$ to 5 are equal to g_{ij} with time shift t_j^k. Note that, in this subsection, i indicates the row, and j and k indicate columns.

3.4 Inversion for the 2011 Tohoku Earthquake Tsunami

3.4.1 Single Time Window Inversion

To clarify the effects of the improved phase correction method on the results for different distant stations, we performed the inversions with Green's functions corrected by scheme 1 and 4 using different station groups: only near-field stations (including wave gauges,

GPS buoys, and OBP gauges), only far-field stations (OBP gauges only), near-field and far-field deep-ocean stations (including GPS buoys and OBP gauges, denoted as deep-ocean stations), and all stations (including wave gauges, GPS buoys, and OBP gauges). Note that the group of deep-ocean stations is composed of 20 near-field stations and 23 far-field stations.

For inversion using non-phase-corrected Green's functions (Figure 3.2a through Figure 3.2d), only near-field stations can reconstruct the tsunami source well (Figure 3.2a). In Figure 3.2a, large sea surface displacement spans from the epicenter to the trench with a peak area of more than 6 m located in the middle of the area. This is similar to the results of other studies (e.g., Gusman et al., 2012; Hossen et al., 2015; Satake et al., 2013) and is considered to be realistic. When using only near-field data, the phase correction has an insignificant effect on the results (Figure 3.2a, Figure 3.2e, and Figure 3.2i), because the phase change at near-field stations is very small. However, when far-field data are used in the inversion (station groups of only far-field stations, deep-ocean stations, and all stations), scattered sea surface displacements appear to the west of the epicenter (Figure 3.2b through Figure 3.2d), which is different from other estimates and is considered to be less reliable. This indicates that the tsunami source cannot be accurately estimated without phase correction if far-field data are used.

For inversion with Green's functions corrected by scheme 1, the results from four station groups were well converged to the east of the epicenter (Figure 3.2f and Figure 3.2h). Figure 3.2f shows the results obtained using only far-field stations with a narrow source to the east of the epicenter extending southwest. Inversion with deep-ocean stations and all stations show similar features, whereby the displacement is concentrated to the east of the epicenter and extends northward along the trench (Figure 3.2g and Figure 3.2h).

For inversions with Green's functions corrected by scheme 4, the peak areas are shifted slightly toward the trench (Figure 3.2i through Figure 3.2l) compared to those corrected by scheme 1 (Figure 3.2e through Figure 3.2h). In Figure 3.2j, a smoothed tsunami source is retrieved by only far-field data. For inversion with deep-ocean stations or all stations, large displacements (approximately 4 m) between the epicenter and the trench are shown in Figure 3.2k and Figure 3.2l. The tsunami sources are well constrained, and the agreement between the synthetic and observed waveforms improved with scheme 4.

A smooth sea surface displacement was obtained by using only far-field data. Because of the dispersion, the initial portion of the waveform at far-field stations used for the inversion contains dominantly long-period waves. Therefore, only long wavelength sea surface change could be retrieved. In contrast, due to the well-recorded waveforms at near-field stations, detailed sea surface variations were retrieved with near-field data.

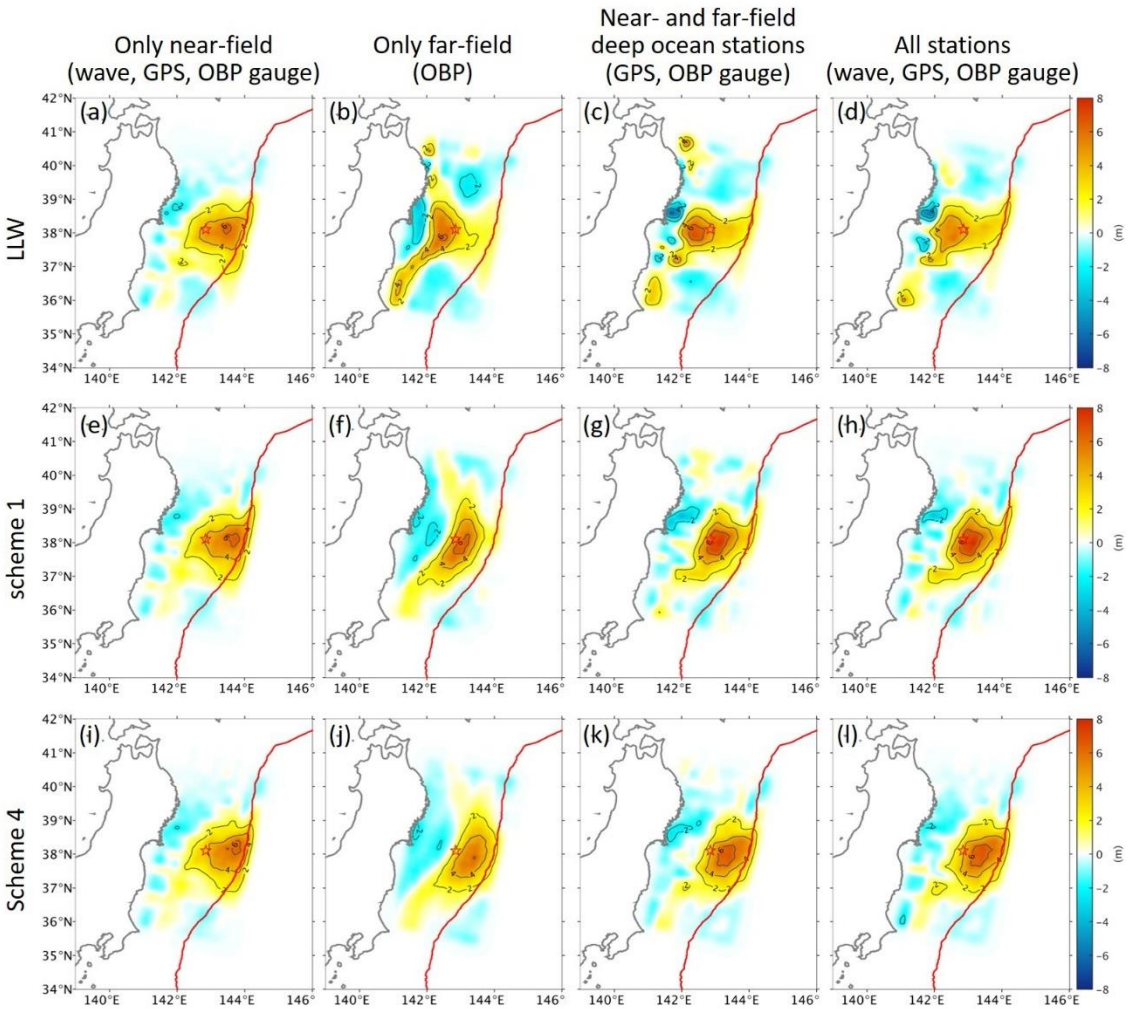

Figure 3.2. Inverted sea surface displacements using Green's functions of different station groups and different correction schemes. (a)-(d) LLW without phase correction, (e)-(h) phase corrected using scheme 1, and (i)-(l) phase corrected using scheme 4. Each column shows a different station group. (a), (e), and (i) Near-field stations only, (b), (f), and (j) far-field stations only, (c), (g), and (k) near-field and far-field deep-ocean stations, and (d), (h), and (l) all stations.

To estimate the misfit of the inversion, we calculated the normalized RMS (NRMS) between the observed and synthetic waveforms. The NRMS error (NRMSE) for the ith station is given by

$$NRMSE_i = \frac{\sqrt{\int_0^\gamma [obs(t) - syn(t)]^2 dt}}{\sqrt{\int_0^\gamma \left[obs(t) - \overline{obs}\right]^2 dt}} \qquad (3.6),$$

$$\overline{obs} = \frac{\int_0^\gamma obs(t)dt}{\gamma}.$$

where $obs(t)$ and $syn(t)$ are the observed and synthetic waveforms, and γ is the data length used for the inversion. Then, we average the NRMSE to obtain the NRMS misfit for the result, as follows:

$$NRMS\ misfit = \frac{\sum_{i=1}^{N} NRMSE_i}{N}, \tag{3.7}$$

where N is the number of stations.

Figure 3.3 shows the NRMS misfit for inversions with all stations, as shown in Figure 3.2d, Figure 3.2h, and Figure 3.2l, respectively. Large misfit (approximately 0.59) was estimated for inversion with non-corrected waveforms, and the misfit was reduced to approximately 0.33 and 0.27 for inversion with waveforms corrected by schemes 1 and 4, respectively.

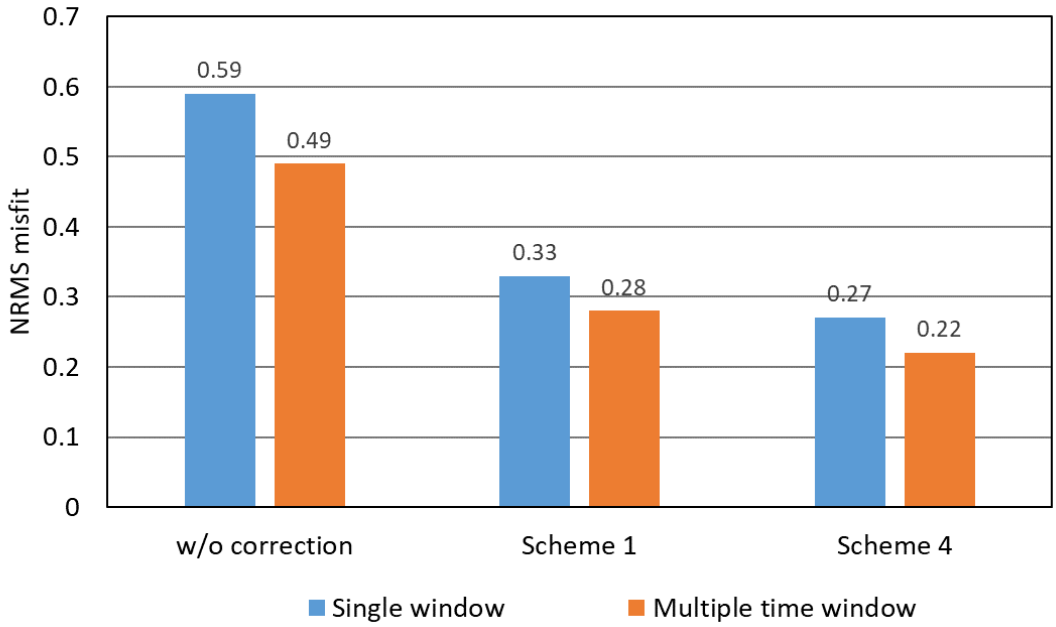

Figure 3.3. NRMS misfit between observed and inverted synthetic waveforms for single and multiple time window inversion (described in section 5.3) using all stations. The single time window inverted sea surface displacements correspond to Figure 3.2d, Figure 3.2h, and Figure 3.2l, respectively.

3.4.2 Forward Prediction from Inverted Results

To further examine the inversion results, we used the inverted sea surface displacements as the initial conditions to perform the forward prediction. The inverted models were obtained using four different station groups, where the Green's functions corrected using scheme 4 were used as the initial conditions for forward predictions. The near-field

stations inverted model (NIM) and far-field stations inverted model (FIM) are shown in Figure 3.2i and Figure 3.2j, respectively. The deep-ocean stations inverted model (DIM) and all-stations inverted model (AIM) are shown in Figure 3.2k and Figure 3.2l, respectively. The tsunami propagations were computed by solving the linear shallow water wave equations with each initial condition, and the computed waveforms were phase corrected using scheme 4. Figure 3.4 shows the synthetic waveforms computed using AIM and the observed waveforms. The phase correction improved the waveform agreement for some near-field stations and for all far-field stations. Moreover, the waveforms corrected using scheme 4 showed better agreement than those corrected using scheme 1.

Figure 3.5 shows the NRMS misfit between the observed and predicted waveforms at all stations, near-field stations, and far-field stations which are corrected by scheme 4. The AIM shows the minimum average misfit for all stations. Because of the abundant high-quality near-field data, the prediction by the near-field inverted model (NIM) agrees well with the waveforms at both near-field and far-field stations. The far-field inverted model (FIM) provides the best prediction at far-field stations but provides poor prediction at near-field stations. As discussed in section 3.4.1, since long wavelength sea surface change was retrieved using only far-field data, the detailed or short-wavelength feature was not well predicted from only far-field data. This is why the NIM has good agreement with the waveforms at far-field stations, but the FIM cannot well predict the waveforms at near-field stations. The misfits of the FIM, DIM, and AIM reveal that adding more near-field stations in the inversion decreases the misfit at near-field stations and maintains the low misfit at far-field stations.

The travel time difference between the observed and predicted waveforms was estimated by applying the cross-correlation (Figure 3.6). Without phase correction, the difference increases with travel time. A difference of more than 12 minutes was estimated when the travel time exceeds 15 hours (1.4% of the travel time). The differences were greatly reduced to less than 4 minutes (approximately 0.4% of the travel time) with correction using scheme 1. After applying the correction of scheme 4, the differences were reduced to less than 2.5 minutes, regardless of travel time.

The forward prediction using the AIM was also compared to the observation of satellite altimeter data. Figure 3.7 shows the synthetic and observed sea surface heights along the track of ENVISAT (Figure 3.7a), Jason-1 (Figure 3.7b), and Jason-2 (Figure 3.7c). The satellite tracks are shown in Figure 3.1a, and the intervals plotted in Figure 3.7 are indicated by the solid lines. The synthetic wavefields of the LLW are located southward compared to the observed wavefield, indicating that they are earlier than the observed wavefields. After we performed the phase correction, the corrected wavefields show good agreement with the observed wavefields. The synthetic wavefields corrected using

scheme 4 show slightly better agreement than those corrected using scheme 1. The tsunami wavefields observed by satellite altimeter were compared by Song et al. (2012). Their model showed good agreement with the altimeter data but exhibited a delay at more distant DART gauges. Our forward simulation shows good agreement with the observed data obtained by the OBS gauges, GPS buoys, and wave gauges, as well as the altimeter data.

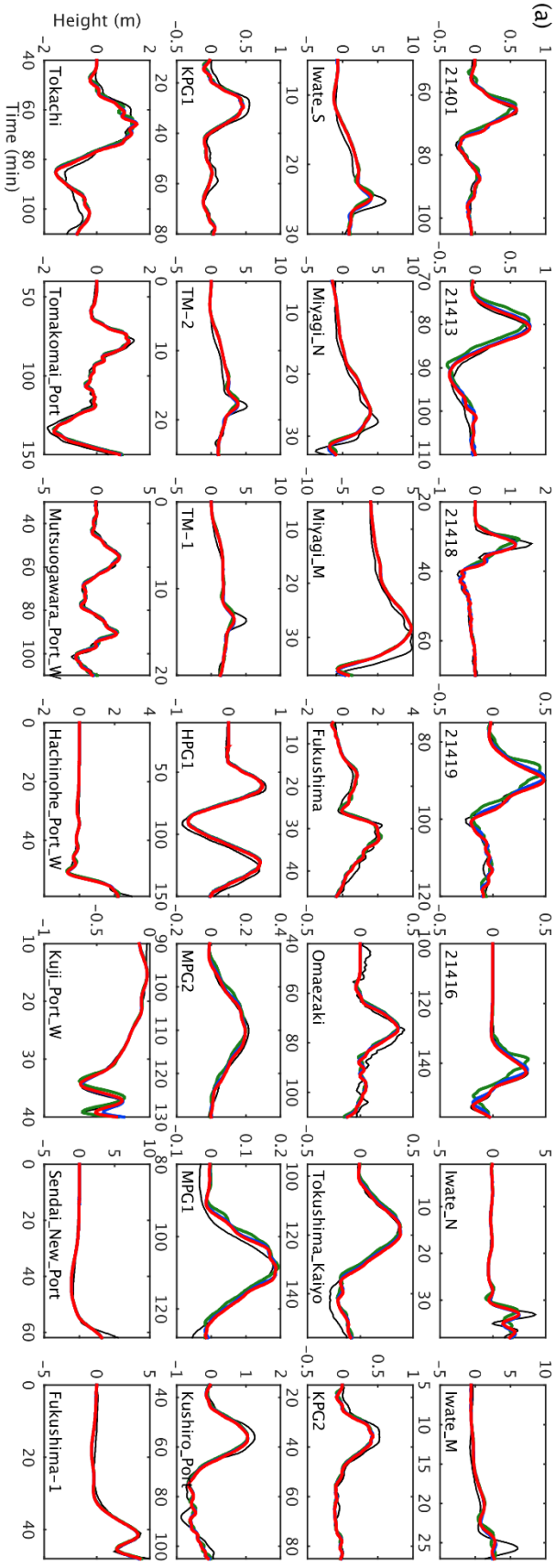

Figure 3.4. Forward simulation results using the AIM and observed waveforms (black line) for (a) near-field stations and (b) far-field stations. The green lines indicate linear long waves. The blue lines indicate the synthetic waveforms corrected using scheme 1, and the red lines indicate the waveforms corrected using scheme 4.

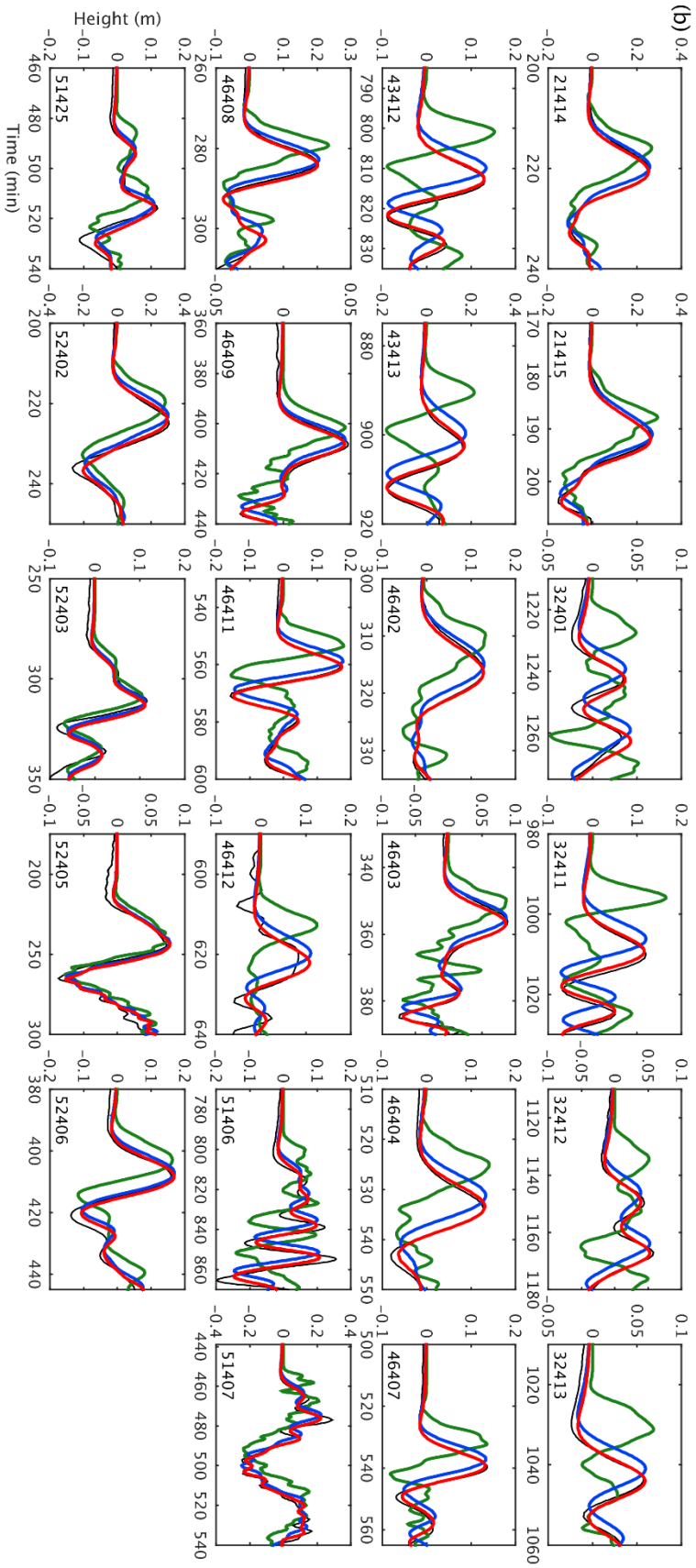

Figure 3.4. (Continued.) Forward simulation results using the AIM and observed waveforms (black line) for (a) near-field stations and (b) far-field stations. The green lines indicate linear long waves. The blue lines indicate the synthetic waveforms corrected using scheme 1, and the red lines indicate the waveforms corrected using scheme 4.

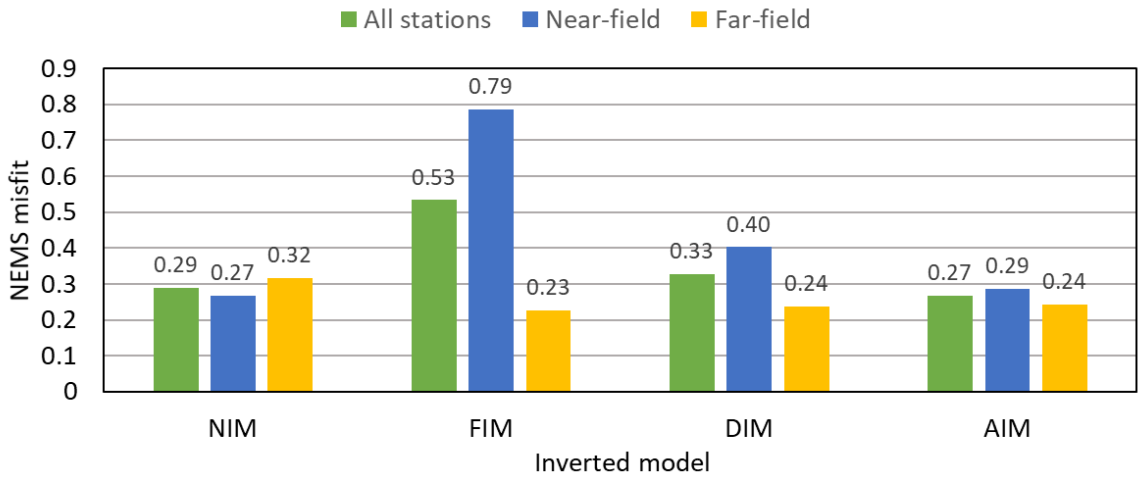

Figure 3.5. NRMS misfits of forward predictions from four inverted models (NIM, FIM, DIM, and AIM). The green, blue, and yellow bars indicate the misfits of forward simulation at all stations, near-field stations, and far-field stations, respectively.

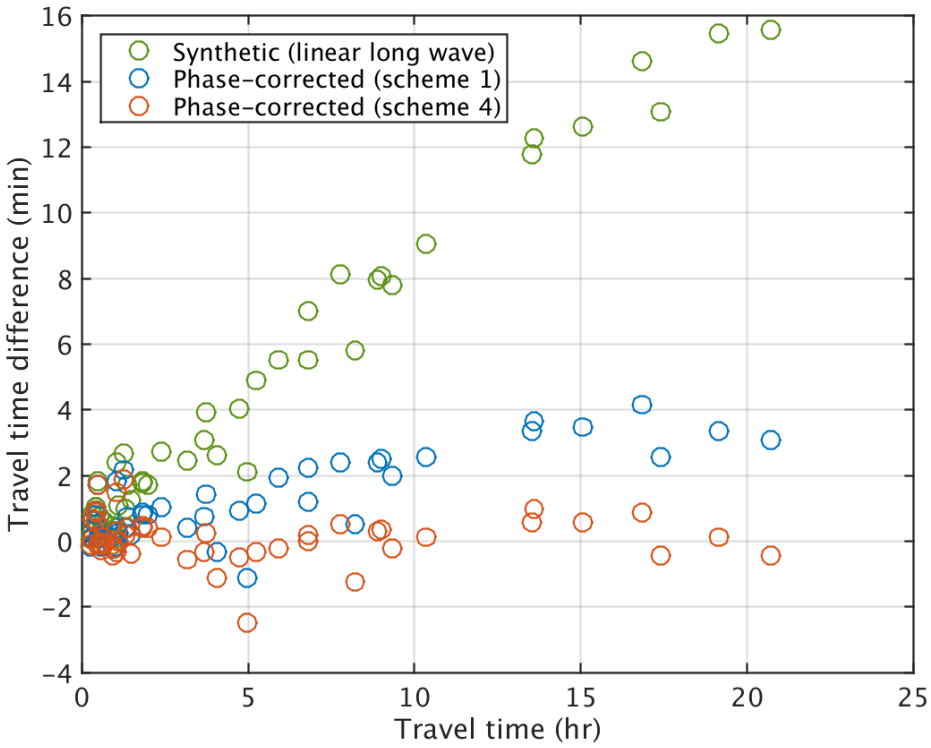

Figure 3.6. Travel time difference between observed and predicted waveforms for all stations. The predicted waveforms are computed using the AIM. The green circles indicate the differences between linear long waves and the observations. The blue circles indicate the differences between the synthetic waveforms corrected using scheme 1 and the observations. The red circles indicate the differences between synthetic waveforms corrected using scheme 4 and the observations.

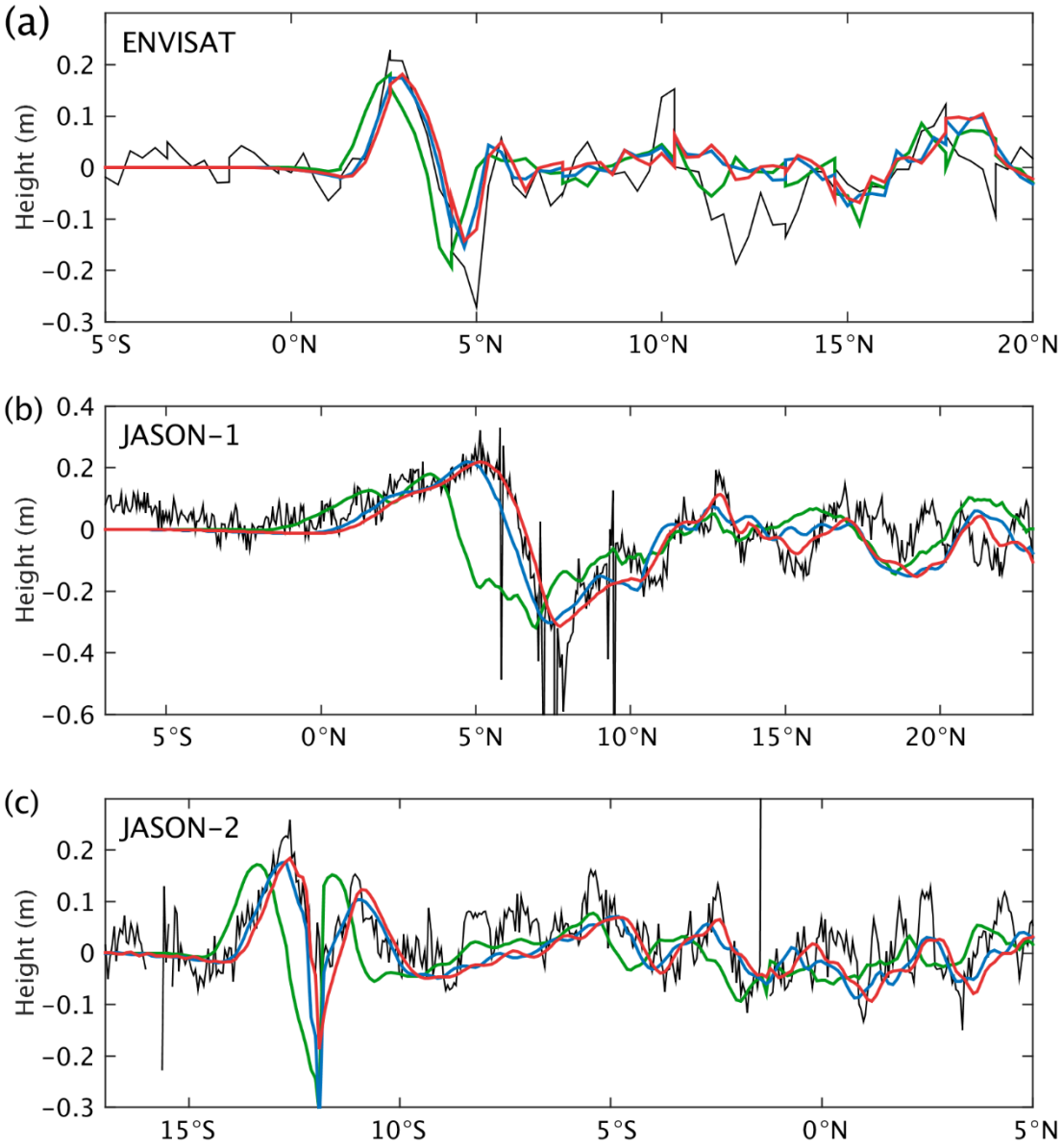

Figure 3.7. Observed (black line) and synthetic tsunami wavefields obtained using the AIM along the tracks. The green lines indicate the synthetic wavefields of the LLW. The blue and red lines indicate the phase-corrected wavefields using schemes 1 and 4, respectively. The horizontal axes indicate the latitude along each track.

3.4.3 Multiple Time Window Inversion

To better understand the potential of far-field data in source inversion, we performed multiple time window inversions using three different station groups, i.e., near-field stations, far-field stations, and all stations, where the Green's functions were corrected using scheme 4. We followed the method of Satake et al. (2013) in performing the multiple time window inversion. The rupture velocity is assumed to be 2.0 km/s, and the time window is 30 seconds with five windows.

The results of multiple time window inversions are shown in Figure 3.8. Figure 3.8a through Figure 3.8c shows the snapshots for different time windows and the cumulated sea surface displacements inverted from data of only near-field stations, only far-field stations, and all stations.

In Figure 3.8a through Figure 3.8c, similar temporal processes were obtained, where the large sea surface displacements initially occur between the epicenter and the trench and then propagate to the trench before 60 sec. From 60 to 150 seconds, the displacement propagates northward along the trench. Most displacements occur within the initial 150 seconds. The spatiotemporal process is similar to the results of (Ide et al., 2011; Shao et al., 2011), but our results take longer time and larger initial displacements. Our pattern change is similar to those estimated by Satake et al. (2013), but our result shows shorter rupture time.

Figure 3.8a and Figure 3.8c show similar displacement patterns in which a peak displacement appears close to the trench from 0 to 90 seconds. The cumulated displacement shows a peak of greater than 6 m located between the epicenter and the trench, and approximately 2-m displacements extending northward along the trench to over 39°N. In Figure 3.8b, smooth sea surface displacements appear in all time windows.

The cumulated displacement of Figure 3.8b is similar to those of Figure 3.8a and Figure 3.8c but is smoother and with a lower peak of about 5 m. This is because of the long-distance dispersion, where only very-long-period waves were used in inversion, as discussed in section 3.4.1. The NRMS misfits for inversions with all stations corrected by different schemes are shown in Figure 3.3. Same as single time window inversion, the misfits are significantly improved after we apply the phase correction, and scheme 4 leads to the best misfits.

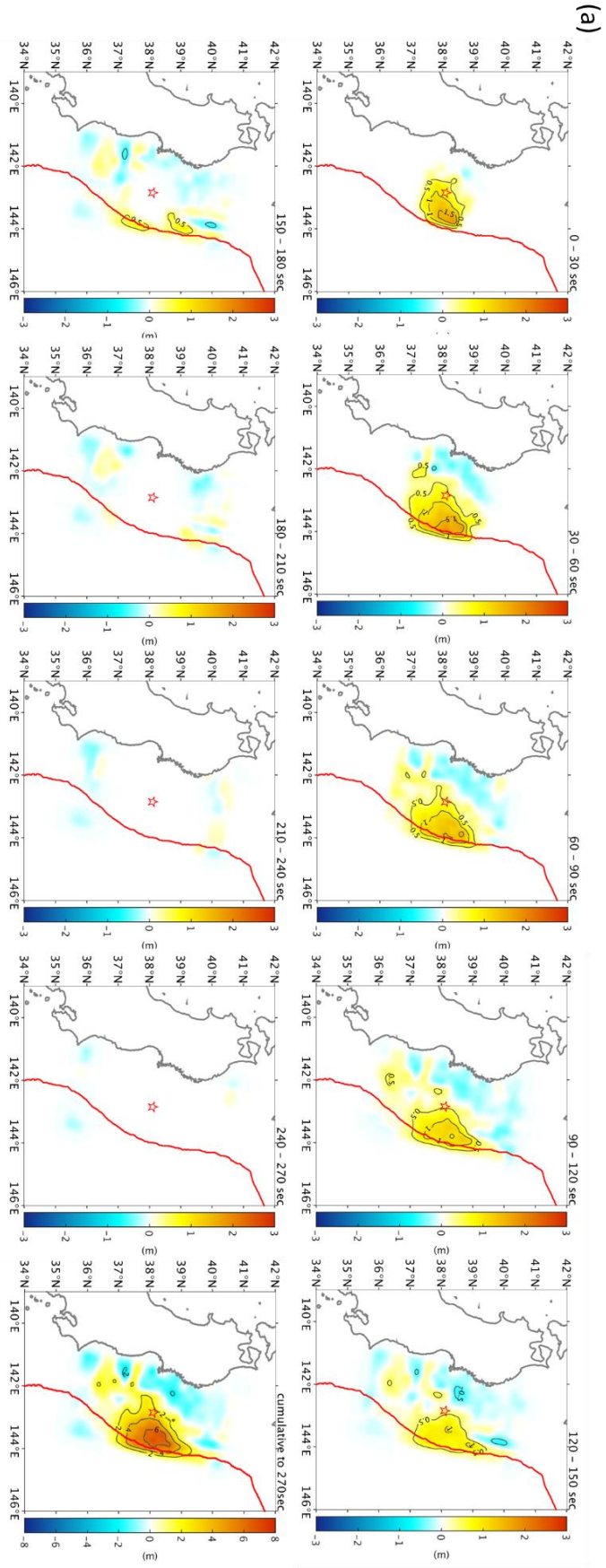

Figure 3.8. Multiple time window inversion results from (a) near-field stations where the waveforms are corrected by scheme 4. The bottom right plot in each figure shows the cumulative displacement of all time windows.

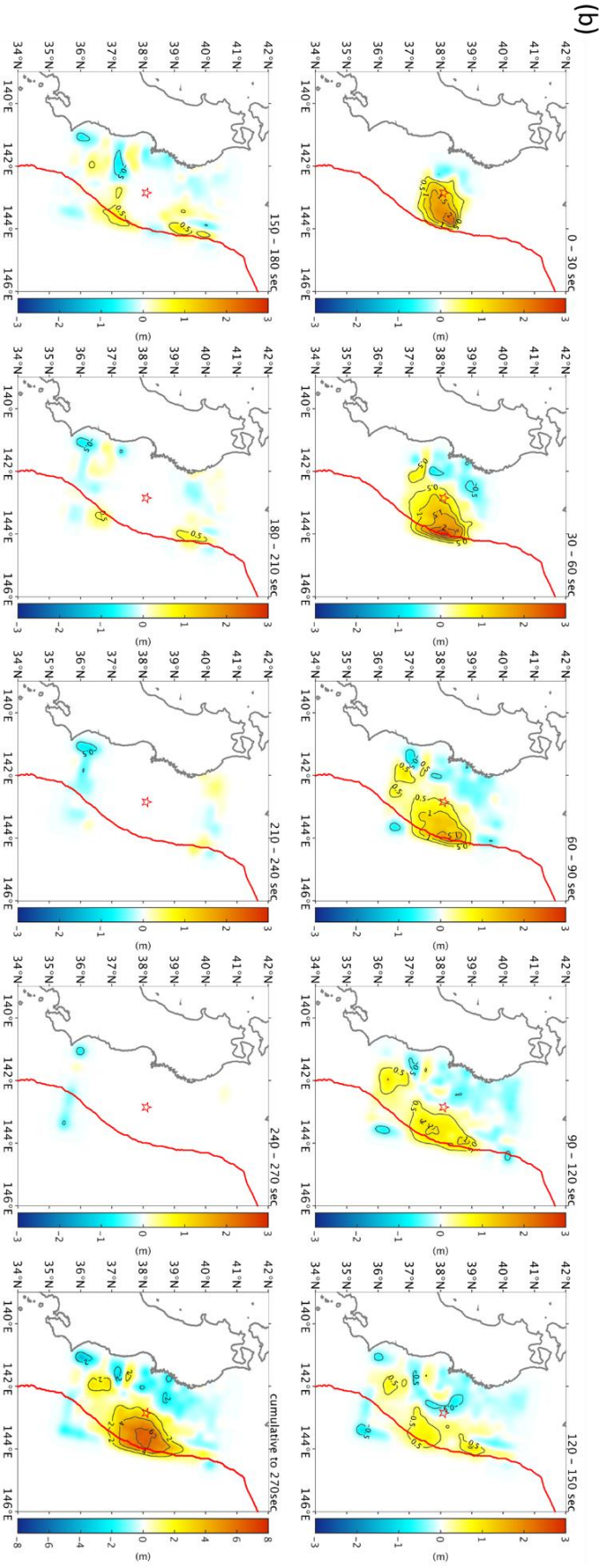

Figure 3.8. (Continued.) Multiple time window inversion results from (b) far-field stations where the waveforms are corrected by scheme 4. The bottom right plot in each figure shows the cumulative displacement of all time windows.

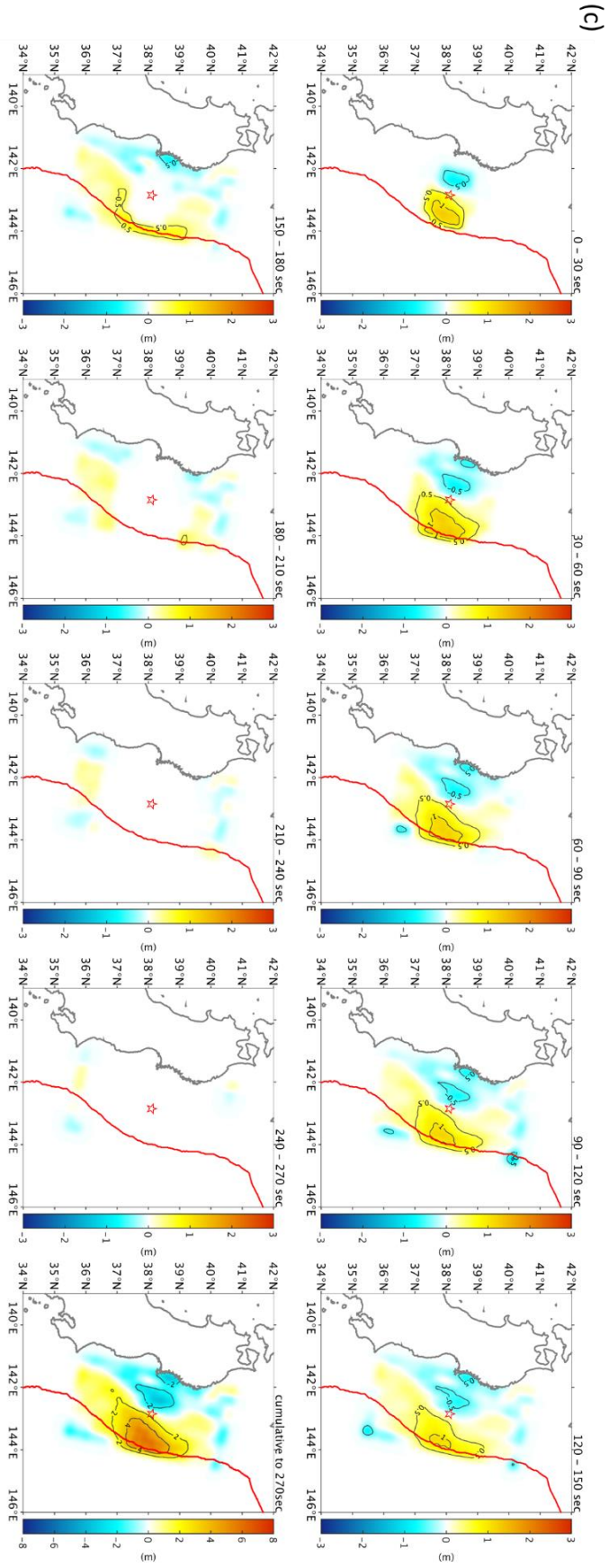

Figure 3.8. (Continued.) Multiple time window inversion results from (c) all stations where the waveforms are corrected by scheme 4. The bottom right plot in each figure shows the cumulative displacement of all time windows.

3.4.4 Forward Prediction from Multiple Time Window Inverted Results

The results of multiple time window inversions were examined by performing forward prediction using the inverted sea surface displacement models. The multiple time window inversion results of the near-field stations inverted model (MW-NIM, Figure 3.8a), the far-field stations inverted model (MW-FIM, Figure 3.8b), the deep-ocean stations inverted model (MW-DIM), and the all-stations inverted model (MW-AIM, Figure 3.8c) were used as the initial conditions for the forward predictions. For the temporal distribution of the initial conditions, the rupture time and sea surface displacements of the five 30-second time windows were resampled linearly every 2 seconds. The initial conditions were then used to compute the tsunami propagation by solving the linear shallow water wave equations, and the computed waveforms were phase corrected using scheme 4.

Figure 3.9 shows the NRMS misfit between the observed and predicted waveforms at all stations, near-field stations, and far-field stations. The MW-NIM and MW-AIM both show better matches than the results from single time window inversions of the NIM and AIM (Figure 3.5), especially at near-field stations. From the NIM and AIM to the MW-NIM and MW-AIM, the NRMS misfits at near-field stations improved by 0.09, but the improvements at far-field stations were only 0.02 and 0.01, respectively. This indicates that the solution of the temporal process is important for near-field stations but only slightly affects far-field stations. This is also shown by the results of the MW-FIM. The NRMS misfit of the MW-FIM was very similar to that of the FIM. The improvement at far-field stations was limited, and a slightly larger misfit was observed at near-field stations. The results of the MW-FIM, MW-DIM, and MW-AIM show that the misfits were improved by adding near-field stations in the inversion, and the improvements were larger than the results of the FIM, DIM, and AIM.

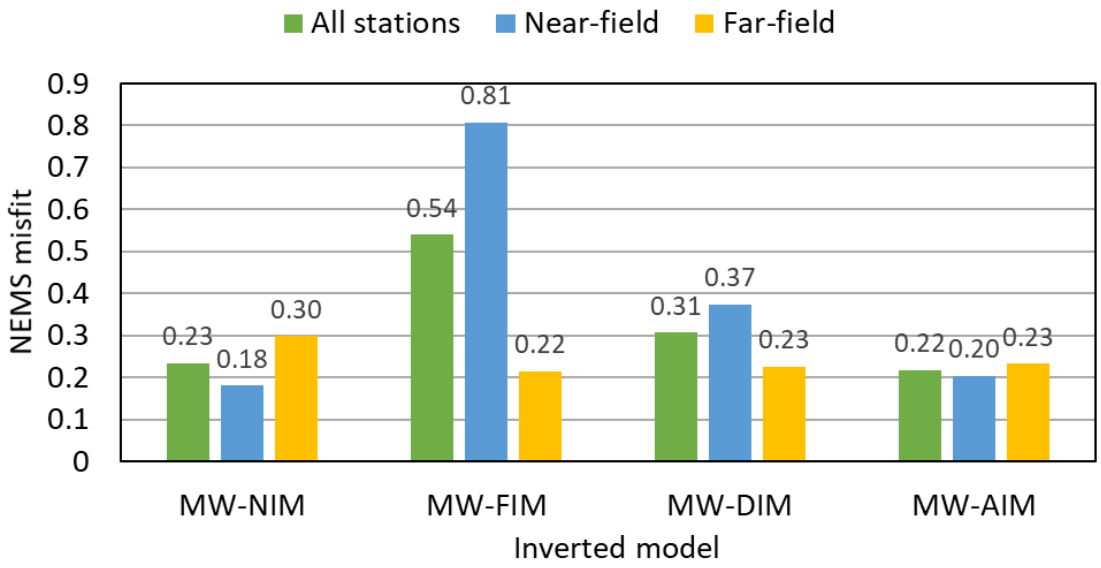

Figure 3.9. NRMS misfits of forward predictions from four multiple time window inverted models (MW-NIM, MW-FIM, MW-DIM, and MW-AIM). The green, blue, and yellow bars indicate the misfits of forward simulation at all stations, near-field stations, and far-field stations, respectively.

3.5 Conclusions

The results of the present study reveal that, when far-field data are used in inversion, more accurate results are obtained using the Green's functions corrected by the improved method. In addition, real-time tsunami forecasting for far-field tsunamis can be significantly improved using the phase correction method. Furthermore, the single and multiple time window inversions with only far-field data incorporating the improved phase correction demonstrate that sea surface displacements similar to those from near-field and all stations data, only smoother and with longer wavelengths, are obtained. Due to the long-distance dispersion, only the long-period waves were used at far-field stations. As a result, only long-wavelength displacement could be retrieved.

Comparisons of the observed data and forward prediction demonstrate the refinement of the waveform misfit and travel time difference by the improved method. The travel time discrepancy between the observed and synthetic waveforms is reduced to less than 2 min for almost all stations, and less than 1 min for most stations, even at stations with travel times longer than 15 hours. Comparison of the satellite altimeter data confirms that the phase correction method provides a better match for the altimeter data and is feasible for the study of the spatial sea surface variation caused by tsunamis.

We also demonstrated the potential of far-field data in single and multiple time window inversion. Using the improved method, a more accurate tsunami source can be inverted

from the waveform data at far-field, as well as a more accurate forward prediction can be made at far-field stations, for the single time window inversion. The multiple window inversion improves the fits for near-field stations, for which the effects of improved phase corrections are small. But the improvements by multiple time window method are limited for far-field stations, for which the effects of the improved phase correction method are significant.

Based on the results of the present study, the tsunami source study of transoceanic tsunamis can benefit from the use of far-field data, especially for many areas without abundant observing facilities. Moreover, the improved phase correction method provides an efficient way to correct linear long waves, which are suitable for existing tsunami forecasting and real-time tsunami prediction systems.

Chapter 4
Application: the 1960 Chile Earthquake Tsunami

The source of the 1960 Chile earthquake was estimated using the geodetic data, local tsunami data, and the newly usable transoceanic tsunami data. The 1960 Chile earthquake is known as the largest earthquake ever recorded. Following the earthquake, a large tsunami was observed by the tide gauges over the entire Pacific Ocean. To estimate the source of this event, we used 301 coastal geodetic data (Plafker and Savage, 1970) together with five near-field tsunami stations from South America, and 44 far-field tsunami stations from North America, Asia, and Oceania. Due to the arrival time differences between long-wave simulations and observations after long distance traveling, the far-field data could not be used for waveform inversions until the arrival problems were well solved by the phase correction method of Watada et al. (2014) and improved and validated in Chapter 2 and 3. In addition, to consider the inaccurate arrival time due to local bathymetry, structure, instrument clock, station position, or even digitalization error from paper records, we applied the nonlinear optimization by the mesh adaptive direct search method (NOMAD) with optimal time alignment (OTA, Romano et al., 2016), which included a time shift parameter for each station. Our results showed a rupture extended about 800 km with a width about 150 km, concentrated at location shallower than 50 km depth. The estimated magnitude was about Mw 9.4. We recovered three asperities at north, central, and south area. Our results also indicated that the south peak has a significant effect on the geodetic data measured in the south as well as the high later tsunami wave phase at some far-field stations.

4.1 Introduction

The 1960 Chile earthquake occurred at southern Chile on 22 May 1960, which is known as the largest recorded earthquake. This event was the main shock which occurred about 15 min following a strong foreshock (Ms 7.8). The extremely strong motion caused severe damage and significant ground movement in Chile. In addition, the rupture led to strong seafloor displacements and triggered a large tsunami, inducing damages to many cities around the Pacific Ocean, e.g., Japan, Hawaii, and Philippine.

Plafker and Savage (1970) analyzed the vertical displacement data, horizontal strain, and teleseismic evidence. They suggested a simple uniform slip dislocation model dipping eastward at a moderate angle with slip at least 20 m on a fault plan of roughly 1000 km long and at least 60 km wide based on the.

Kanamori and Cipar (1974) used surface waves, R2 and G2 waves, recorded by a strain seismograph at Pasadena to determine fault process. They estimated a thrust fault with dip about 10° and rupture length 800 km. For the main shock, a seismic moment 2.7×10^{23}Nm with the fault area 1.6×10^{5} km and average slip 24 m were evaluated. They also suggested a foreshock of a large slow deformation with slip 30 m and time 300-600 sec, and the seismic moment was comparable to the mainshock.

The free oscillations excited by the earthquake were analyzed to evaluate the rupture model. Kanamori and Anderson (1975) analyzed the free oscillation data from UCLA, Pasadena, and Isabella. They indicated that a mainshock and a slow precursory source, occurred 15 min before the mainshock, can interpret the observed data. The estimated total moment was $4 - 5 \times 10^{23}$Nm. Their result also suggested that the seismic moment of the mainshock was $\sim 2 \times 10^{23}$Nm, and the moment of the precursor was close to the mainshock as proposed by Kanamori and Cipar (1974).

Cifuentes and Silver (1989) performed the normal mode analysis of the amplitude data recorded at eight long period vertical component seismograms. They proposed a source model of total seismic moment 5.5×10^{23}Nm and a duration of 1500 sec. The source model consisted of three events: a slow precursor with moment 1.9×10^{23}Nm and rise time of 300 sec occurred 1150 sec before the main shock; the seismic moment of the main shock was 3.2×10^{23}Nm, and followed by an afterslip, with moment 0.4×10^{23}Nm.

The slip distribution was estimated using the observed geodetic data with an assumed fault plane. Barrientos and Ward (1990) assumed a planar slab geometry and used the geodetic data (Plafker and Savage, 1970) to estimate a uniform slip plantar model (USP) and a variable slip plantar model (VSP). Both models showed a comparable seismic moment $9.4 - 9.5 \times 10^{22}$ Nm. The VSP model showed a shallow slip in a 900 km long and 150 km wide band parallel to the coast, most slips concentrated offshore. The three isolated deep patches at 80-110 km depth were presumably aseismic slip.

Moreno et al. (2009) applied a 3D finite element model with a precise slab geometry to invert the geodetic dataset of Plafker and Savage (1970). Their results indicated the slip distribution was limited to the offshore shallow region of the plate interface. The rupture area was comparable to the result of Barrientos and Ward (1990). The seismic moment was $9.1 - 10.2 \times 10^{22}$Nm.

Fujii and Satake (2013) jointly used tsunami and geodetic data to estimate the slip distribution. They used 12 tide gauges in South America together with the geodetic data (Plafker and Savage, 1970). Their result showed a main slip on the shallow region with a seismic moment 7.2×10^{22}Nm. This moment is slightly smaller than other estimates from geodetic data (Barrientos and Ward, 1990; Moreno et al., 2009). Although tsunami data were included in the joint inversion, the stations used in Fujii and Satake (2013) are all located north of the source region along the South American continent.

From above. the estimated magnitude varies from the different data source and different studies. For example, seismic moments of the order of $2 - 3 \times 10^{23}$ Nm were estimated from free oscillation (Kanamori and Anderson, 1975; Cifuentes and Silver, 1989), and surface waves (Kanamori and Cipar, 1974). However, the estimated seismic moments are much smaller from the geodetic data of the order of 1×10^{23}Nm (Barrientos and Ward, 1990; Moreno et al., 2009), and the estimate from the joint tsunami and geodetic data (Fujii and Satake, 2013) also showed a smaller seismic moment.

The inversion using geodetic data estimated the slip distribution that concentrated offshore at a shallow region. However, the geodetic data are all measured on land. The tsunami data provide additional information for the offshore sources, and the transoceanic data can provide better data azimuthal encompassment. The tsunami triggered by the 1960 Chile earthquake impacted the entire Pacific Ocean and recorded by the tide gauges around the coasts on the Pacific Ocean (Berkman and Symons, 1964), in addition to the tide gauges in South America. Fujii and Satake (2013) indicated the distant stations were not used because of the arrival time discrepancy between observed and computed waveforms.

Recently, the systematic arrival time discrepancy between observed and computed waveforms at far-field was well explained (Allgeyer & Cummins, 2014; Tsai et al., 2013; Watada et al., 2014). The phase correction method proposed by Watada et al. (2014) converts the linear long waves into dispersive waveforms. This characteristic of linear leads to the practical source estimate from far-field observation.

In the present study, tide gauge data from South America, North America, Asia, and Oceania were inverted jointly with the geodetic data. We applied the phase correction method (Watada et al., 2014), which was further improved by Ho et al. (2017), to solve the systematic travel time delay and initial phase reversal. The tide gauge azimuthal

problem has been solved and the quantity of tsunami data is improved. As a result, the slip distribution at the shallow region is well reconstructed.

4.2 Data

4.2.1 Tsunami Waveform Data

The 1960 Chile earthquake triggered a large tsunami and impacted the entire Pacific Ocean. The tsunami waves were observed by tens of tide gauges in Chile, Peru, Ecuador, Colombia, Mexico, USA, Canada, Australia, New Zealand, Philippines, Japan, islands in the Pacific Ocean, etc. (Berkman and Symons, 1964).

This tsunami caused 3 m high waves in Talcahuano (Chile). For far-field gauges, the largest wave was recorded in Hakodate (Japan) with up to 2 m. Gauges in the west coast of USA, Hawaii, and New Zealand also recorded strong waves of about 1 m high. The near-field waveforms were used to estimate the source in Fujii and Satake (2013), but the far-field waveforms were used only for comparison. Fujii and Satake (2013) digitalized the historical documents, and we resampled the data into 15-sec intervals. In the present study, five near-field gauges in Chile and 44 far-field gauges were used to estimate the tsunami source (Figure 4.1).

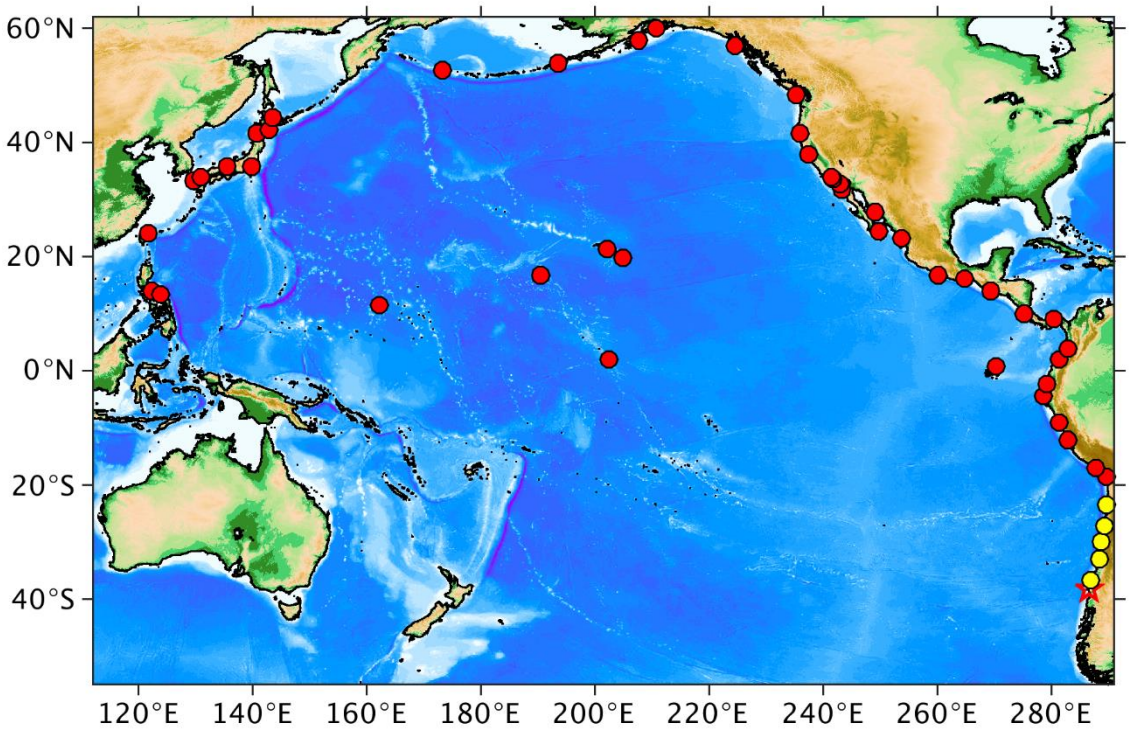

Figure 4.1. The entire computation domain. The red star shows the epicenter of the 1960 Chile earthquake. Red dots indicate far-field stations and yellow dots for near-field stations.

4.2.2 Geodetic Data

The coastal elevation data and leveling data along a highway (Plafker and Savage, 1970) were used jointly with tsunami data (Figure 4.2). The coastal elevation data were measured in 1968 at 155 locations from about 36°S to 46°S. According to Plafker and Savage (1970), the coastal elevation data were the evaluated vertical displacements along the coast based on pre- and post-earthquake changes of: the lower growth limit of terrestrial vegetation, the upper growth limits of mussels, and high tide level reported by residents. The estimated accuracies of the observations were noted as good (±0.2m), fair (±0.4m), poor (±0.6m), and unknown. The largest uplift was recorded in the Guamblin Island with about 5.7 m, and the largest subsidence was recorded in Valdivia city with -2.7 m. The leveling data are the vertical displacements along the Interamerican Highway of post-earthquake (1957-1959) relative to pre-earthquake (1963-1964). The leveling data were drawn by Plafker and Savage (1970) and digitalized with 146 points (Fujii and Satake, 2013). Although post-earthquake effects may affect the observations, this effect can be reduced by joint inversion with tsunami data.

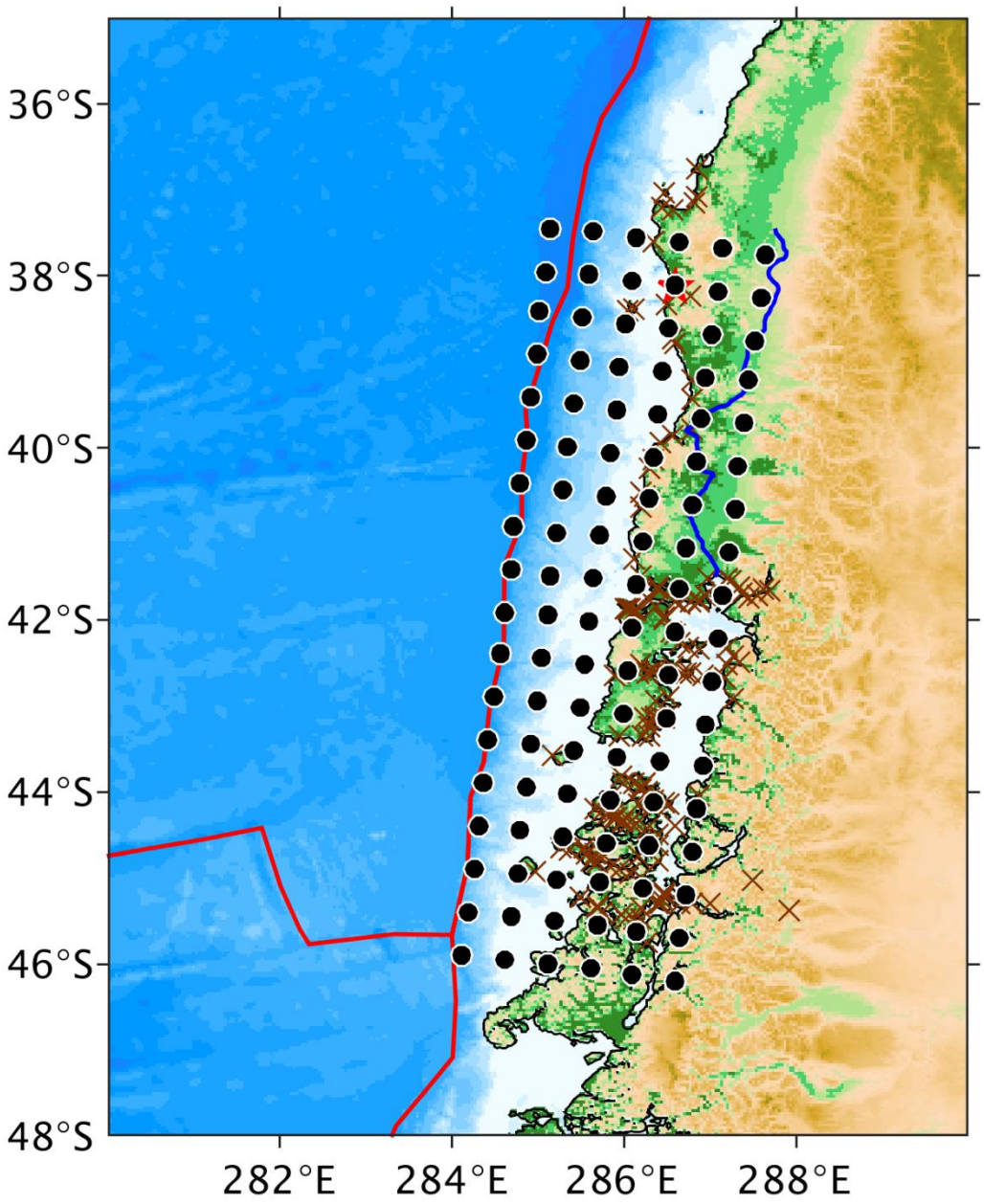

Figure 4.2. Distribution of unit sources (black dots), and geodetic data of coastal elevation positions (brown crosses) and leveling data along a highway (blue line). Red lines indicate the trenches.

4.3 Methods

4.3.1 Tsunami Simulation

The linearized long wave theory has been commonly used to calculate the tsunami propagation. In the present study, we used the linear shallow water equations in spherical coordinates:

$$\frac{\partial \eta}{\partial t} = -\frac{1}{Rsin\theta}\left[\frac{\partial P}{\partial \varphi} + \frac{\partial (Qsin\theta)}{\partial \theta}\right] \quad (4.1)$$

$$\frac{\partial P}{\partial t} = -\frac{gD}{Rsin\theta}\frac{\partial \eta}{\partial \varphi} - fQ \quad (4.2)$$

$$\frac{\partial Q}{\partial t} = -\frac{gD}{R}\frac{\partial \eta}{\partial \theta} + fP, \quad (4.3)$$

where η is the wave height, D is the water depth, t is time, R is Earth's radius, P and Q are the depth-integrated flow along longitude φ and latitude θ, respectively, f is the Coriolis coefficient (= $2\Omega cos\theta$), and Ω is the angular frequency of the Earth's rotation. Equation (4.1) is the continuity equation, and equations (4.2) and (4.3) are the horizontal momentum equations in spherical coordinates. We solve the linear shallow water equations applying a well-developed and verified finite difference solver JAGURS (Baba et al., 2015; Baba et al., 2017).

We used a nested grid scheme for our calculation: A 2' bathymetry with domain 120°E-69°W (291°E) and 55°S-62°N (Figure 4.1) for the entire domain, and 40'' bathymetry for the area near each station. The bathymetry was resampled from the data of GEBCO_14 (Weatherall et al., 2015) 30'' grids.

4.3.2 Phase Correction

To incorporate the dispersion effect after long distance traveling, we applied the phase correction method (Watada et al., 2014; Ho et al., 2017) to the Green's functions of tsunami waveforms. Note that only stratification effect was considered in this chapter. The travel time delay of actual ray path and actual depth are incorporated by the OTA method. The tsunami wave phase change by those two effects is very small and can be neglected (Figure 2.6). The details had been introduced in Chapter 2.

4.3.3 Inversion Method

We set 6 by 18 Gaussian-shaped vertical displacements on the potential source region as our initial unit sources (Figure 4.2). We assumed the strike is 7°. For a unit source j located at φ_j and θ_j is expressed by

$$\eta_j(\varphi,\theta) = exp\left[-\frac{\left(\varphi-\varphi_j\right)^2+\left(\theta-\theta_j\right)^2}{2\sigma^2}\right] \quad (4.4)$$

where the characteristic length σ is 15'. The interval of unit sources is 30'. We calculated the Green's function from each unit source to each station and used them to estimate the tsunami source.

To incorporate the possible random arrival time shift which may be caused by instrument clock problem, inaccurate station position, bay effect, harbor effect, or unknown instrument response, we applied the mesh adaptive direct search (MADS) algorithm (Audet & Dennis, 2006) with the optimal time alignment (OTA) method (Romano et al., 2016).

In the OTA method, a time shift $\boldsymbol{T}$ was used to minimize the misfit between observed and synthetic waveforms. The cost function for station i is

$$E_i(T_i) = 1 - \frac{2\int_{t1}^{t2} obs_i(t)syn_i(t-T_i)dt}{\int_{t1}^{t2} obs_i^2\,(t)\,dt + \int_{t1}^{t2} syn_i^2(t-T_i)dt} \quad (4.5)$$

where E_i is the misfit for station i, T_i is the time shift, obs_i and syn_i are the observed and synthetic waveforms, respectively. The syn_i is given by

$$syn_i = \mathbf{G_i} * \mathbf{X}$$

where $\mathbf{G_i}$ is the Green's functions for station i, $\mathbf{X}$ is the unknown column vector of the height of unit sources. For geodetic data, we used a slightly different cost function

$$\epsilon = N_{TG} * \frac{\sum_{i=1}^{N}\left(obs(x_i)-syn(x_i)\right)^2}{\sum_{i=1}^{N} obs^2\,(x_i) + \sum_{i=1}^{N} syn^2(x_i)} \quad (4.6)$$

where x_i indicates the data position, N is the geodetic data number. The N_{TG} is the number of tidal gauges as the weighting for geodetic data.

We applied the optimization algorithm of mesh adaptive direct search method (MADS, Audet & Dennis, 2006) to obtain the $\mathbf{X}$ and $\boldsymbol{T}$ that minimize the sum of E_i and ϵ. This algorithm is implemented by the optimization solver - nonlinear optimization by mesh adaptive direct search (NOMAD, Audet et al., 2009; Le Digabel, 2011). The MADS iteratively search the point on the mesh, the space of variables, that improves the current best solution. When it fails to obtain a better solution, the algorithm refines the mesh and search the point on the finer mesh.

4.4 Resolution Analysis

We analyzed the robustness and resolution of our inversion method by performing checkerboard tests. We built an initial source composed of 2 by 6, positive and negative staggered blocks (Figure 4.3a). Each block was composed of 3 by 3, 2-m amplitude unit sources (Figure 4.2, 2 m for positive blocks -2 m for negative blocks). The maximum amplitudes at the overlapped area were about 3.3 m and -3.3 m, respectively. We computed the tsunami propagation as described in section 4.3.1. The assumed synthetic waveforms were observed by the virtual tide gauges at the same positions of the real case. The assumed synthetic geodetic data were also observed by the virtual observation points.

4.4.1 Resolution Test

We added 5% Gaussian noise (the σ of noise is 5% of the maximum amplitude of synthetic waveform in the used time window) to the assumed synthetic waveforms and the synthetic geodetic elevations. Figure 4.3b shows the estimated displacement of joint inversion. The assumed displacement was well recovered, except for the offshore blocks between 42°S to 44°S were slightly overestimated. It also excellently fitted the assumed synthetic geodetic data (Figure 4.4) and tsunami waveforms (Figure 4.5 and Figure 4.6).

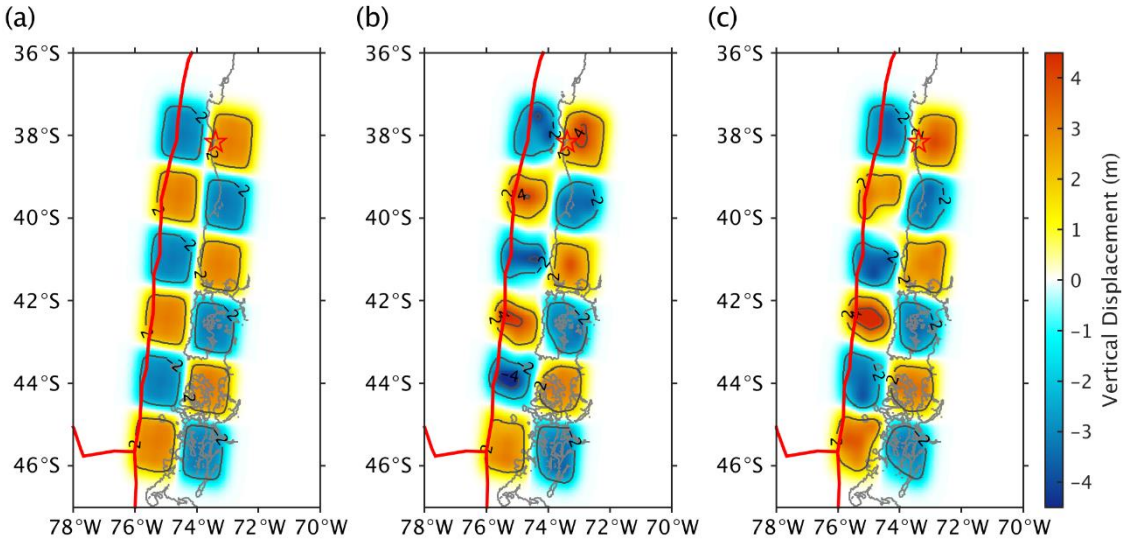

Figure 4.3. The vertical displacement of (a) assumed checkerboard source and joint inversion result of (b) without assumed time shifts and (c) with assumed time shifts.

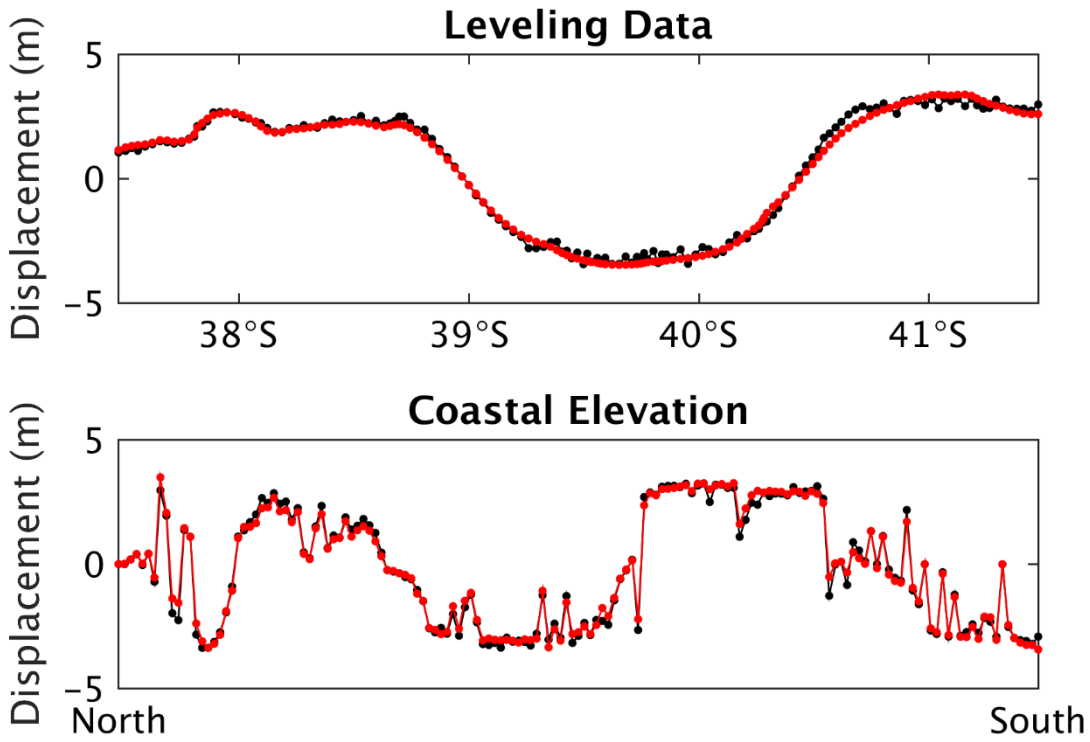

Figure 4.4. The synthetic geodetic data from the assumed source (black) and inversion (red).

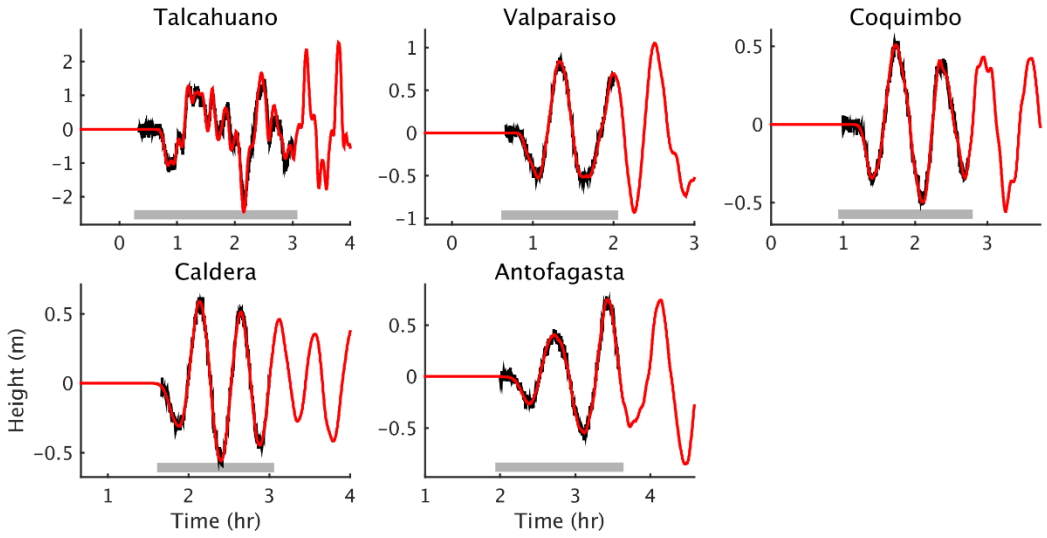

Figure 4.5. The synthetic waveforms from assumed source (black) and inversion (red) at near-field.

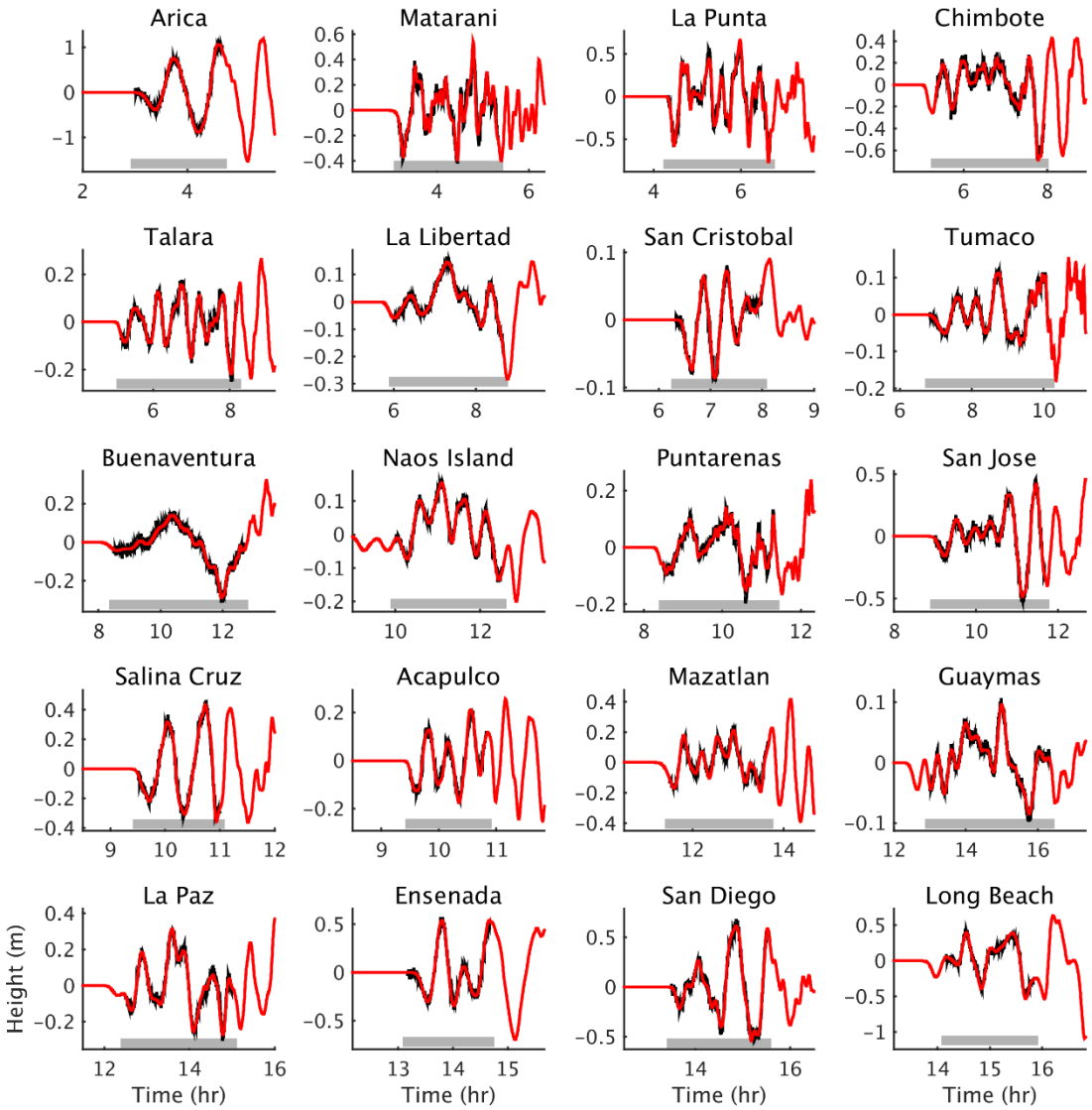

Figure 4.6. The synthetic waveforms from assumed source (black) and inversion (red) at far-field.

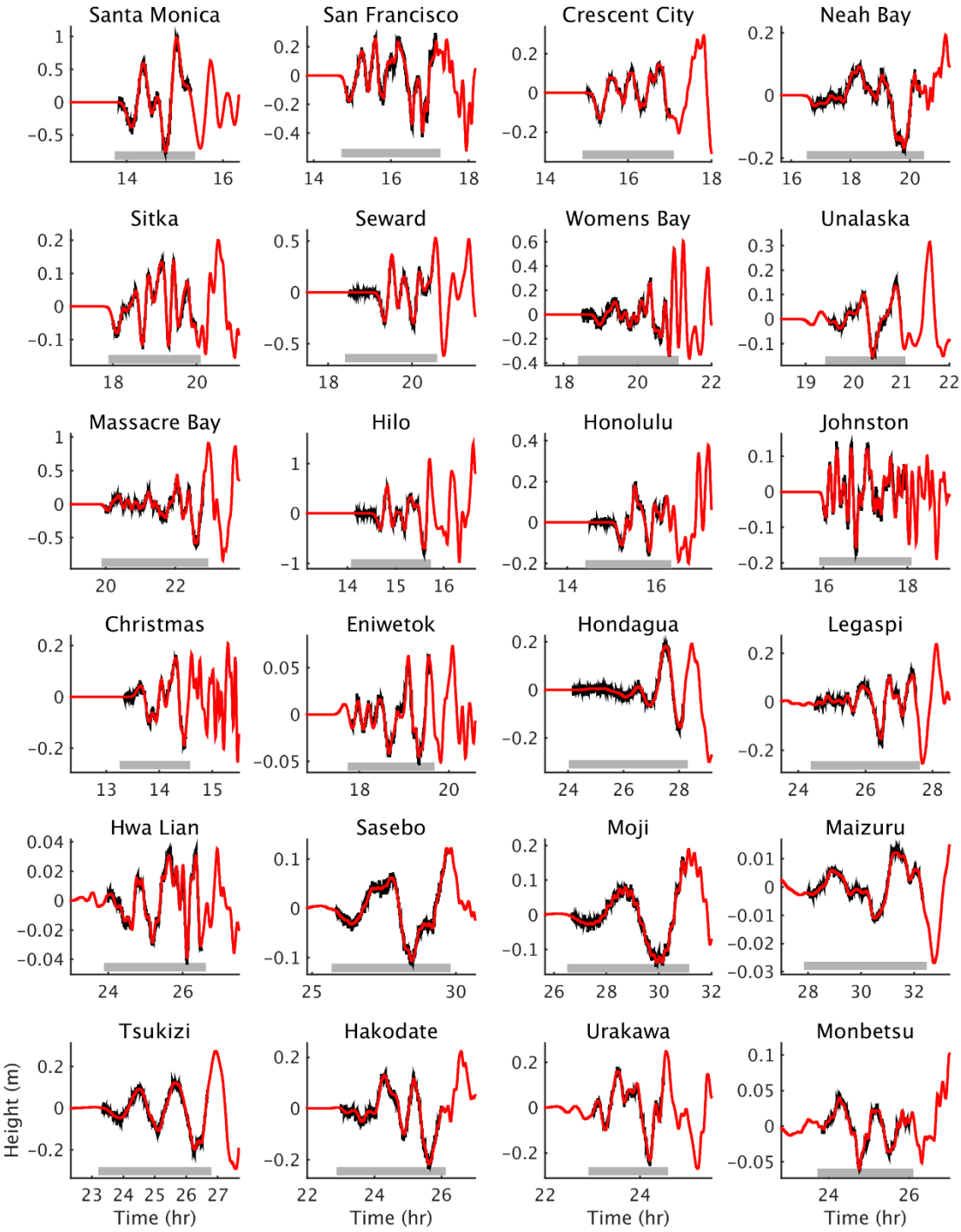

Figure 4.6. (Continued.) The synthetic waveforms from assumed source (black) and inversion (red) at far-field.

4.4.2 Optimal Time Alignment (OTA) Test

We tested the OTA method by randomly assigning a time shift to each assumed synthetic waveform. The random time shift was uniformly distributed on the interval -50 to 50 min. A 5% Gaussian noise was also added to the time-shifted waveforms.

Figure 4.3c shows the inversion result for the OTA test. It well recovered the assumed displacement and the assumed synthetic geodetic data (Figure 4.7). Figure 4.8 and Figure 4.9 show the assumed and inverted synthetic waveforms. Our inversion excellently fitted the assumed synthetic waveforms. And the random pre-assigned time shift was also excellently predicted, except Tumaco and Unalaska showed 1 min error.

In this section, we had successfully inverted the assumed checkerboard source and fitted the assumed synthetic geodetic data and tsunami waveforms. In the OTA test, we also excellently predicted the random pre-assigned time shifts. Our inversion method was then used to estimate the source of the 1960 Chile earthquake.

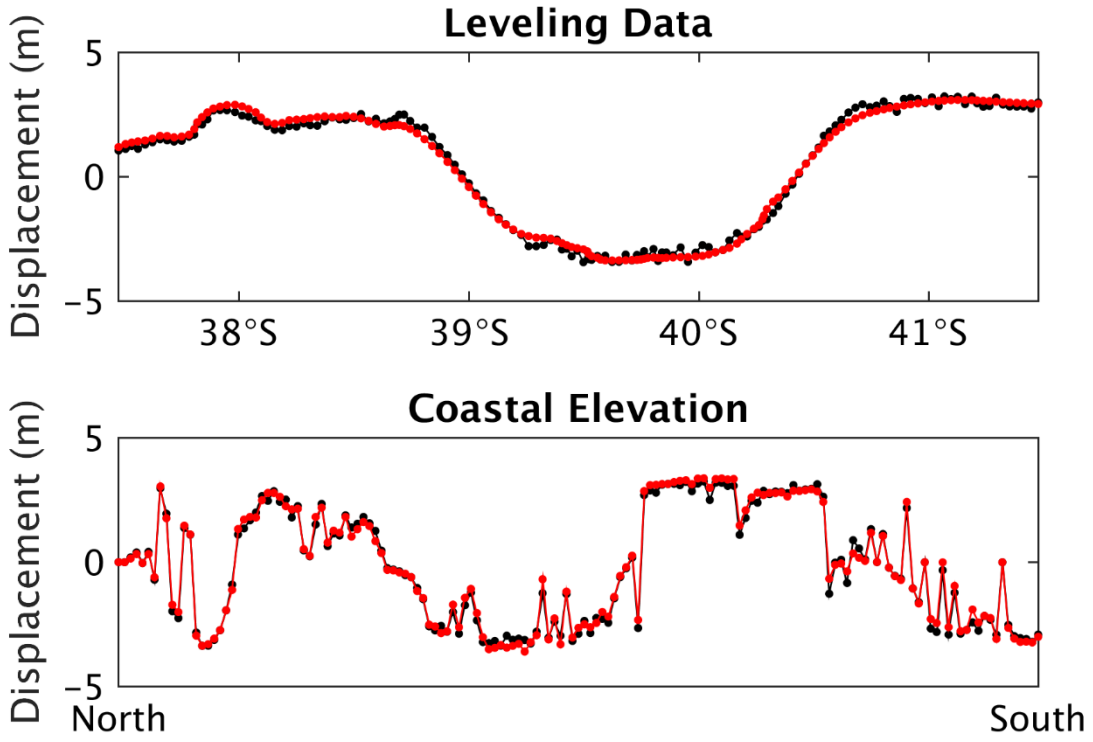

Figure 4.7. The synthetic geodetic data from the assumed source (black) and inversion (red).

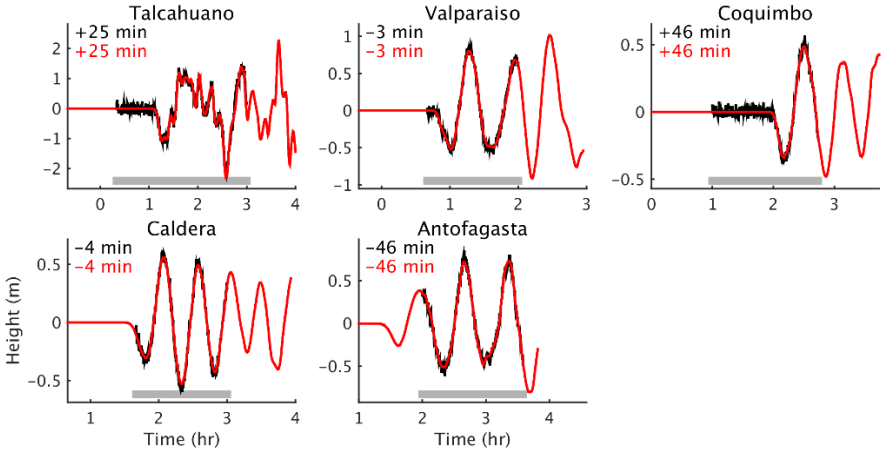

Figure 4.8. The synthetic waveforms from assumed source (black) and inversion (red) at near-field. The numbers at upper left corner indicate the random pre-assigned time shift (black) and predicted time shift by OTA (red).

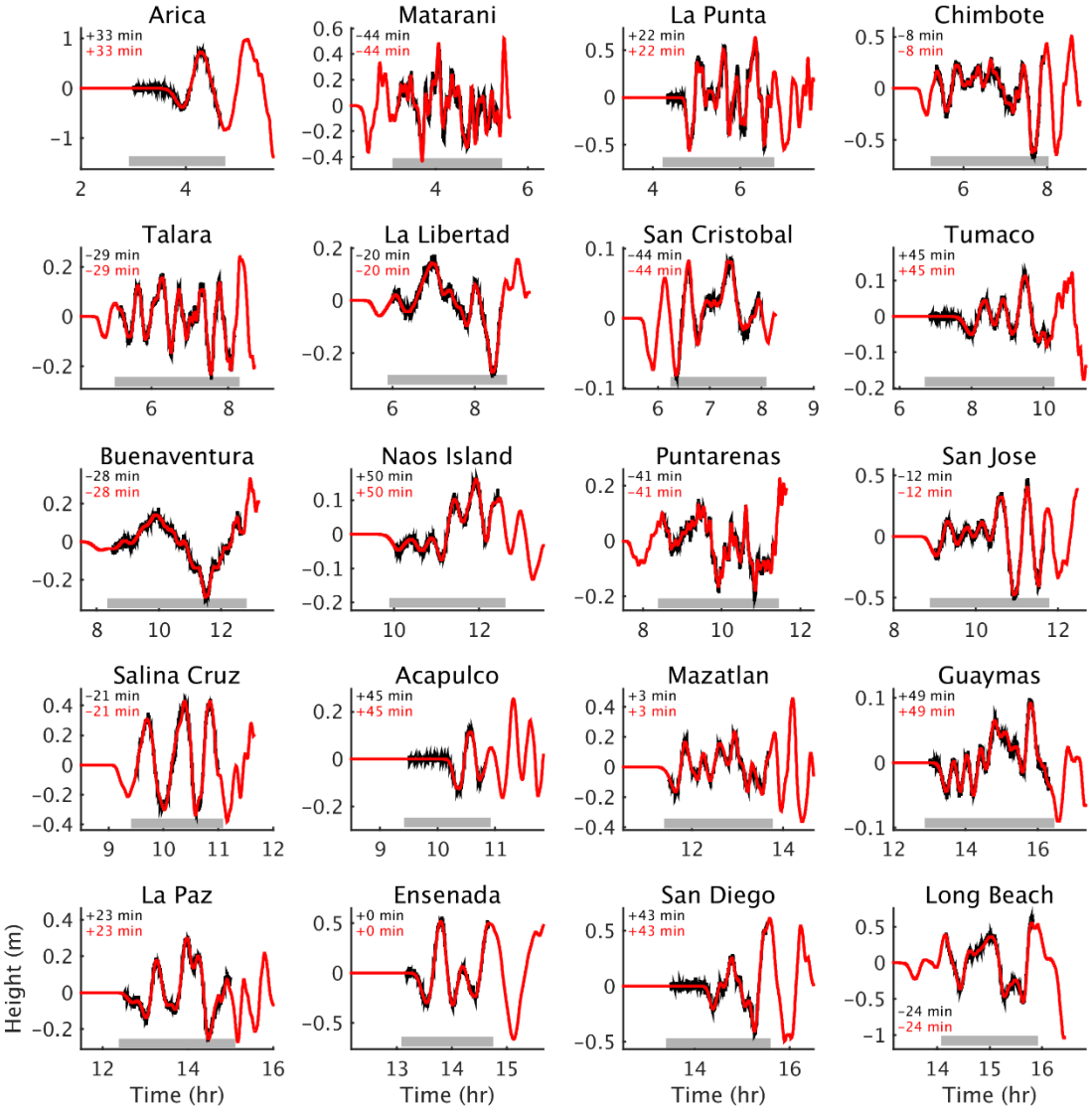

Figure 4.9. The synthetic waveforms from assumed source (black) and inversion (red) at far-field. The numbers at upper left corner indicate the random pre-assigned time shift (black) and predicted time shift by OTA (red).

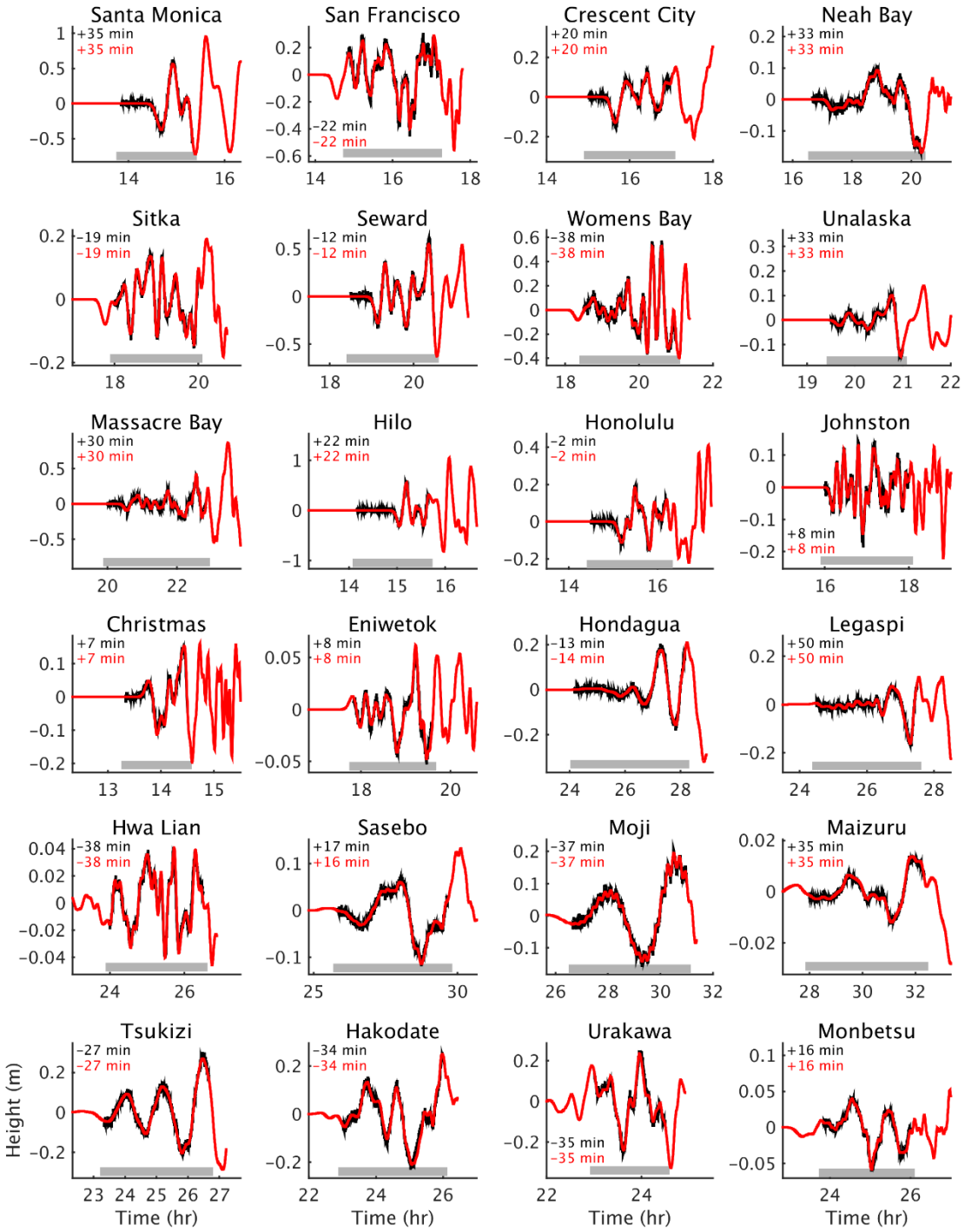

Figure 4.9. (Continued.) The synthetic waveforms from assumed source (black) and inversion (red) at far-field. The numbers at upper left corner indicate the random pre-assigned time shift (black) and predicted time shift by OTA (red).

4.5 Source Estimation for the 1960 Chile Earthquake

4.5.1 Joint Inversion of Tsunami Waveforms and Geodetic Data

In this section, we performed the source estimation using tsunami waveforms and geodetic data jointly. Both near-field and far-field tsunami waveforms are used. The estimate using nonlinear inversion with OTA method (Figure 4.10b) is compared with the one without the OTA method (Figure 4.10a).

Figure 4.10a shows three patches from about 38°S to 46°S. When we applied the inversion with the OTA method, the result shows a similar pattern, but a smaller central patch is presented (Figure 4.10b). Both results recovered a high amplitude south patch. The large south displacement with more than 6 m contributed to the large coastal elevation observed in Guamblin Island.

Figure 4.11 and Figure 4.12 show the observed and synthetic waveforms of inversion without the OTA method at near-field and far-field. Obvious arrival time discrepancy appears at many stations including near-field, e.g. Talcahuano and Valparaiso, and far-field stations, e.g. San Diego, Johnston, and Tsukizi (Tsukiji). In addition, due to the inaccurate inversion, inaccurate synthetic wave periods appear in some stations, e.g. Acapulco, Ensenada, and Long Beach.

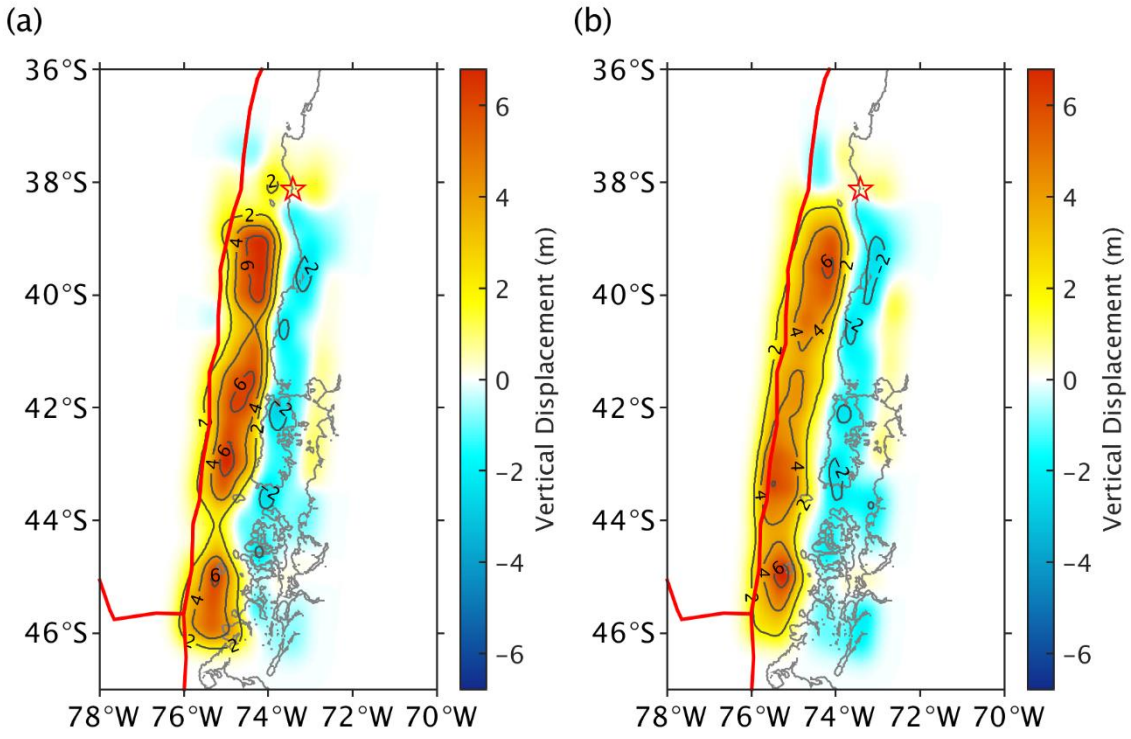

Figure 4.10. Estimated vertical displacements from the joint tsunami and geodetic data (a) without the OTA method, and (b) with the OTA method.

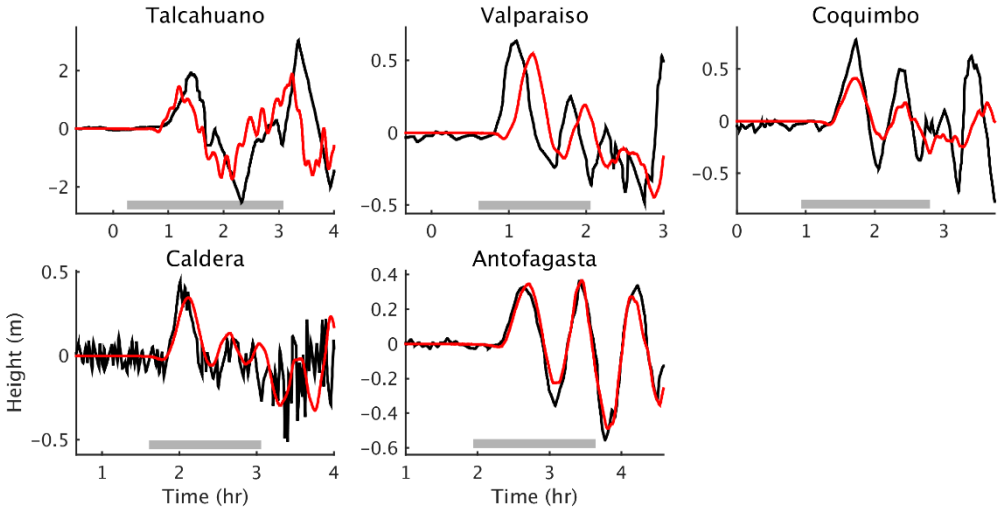

Figure 4.11. The observed (black) and synthetic (red) tsunami waveforms at near-field. The gray bars indicate the used time window for inversion.

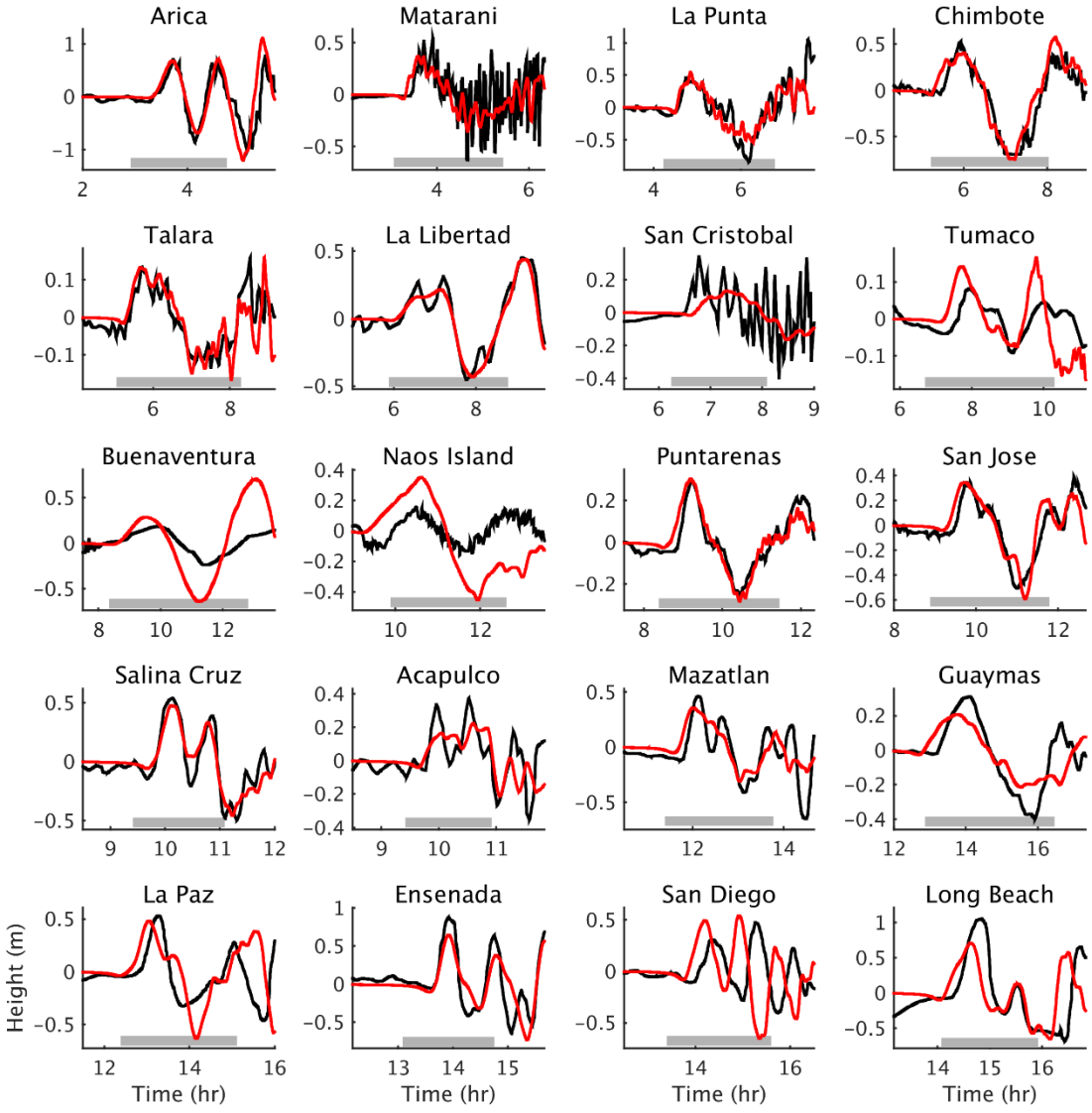

Figure 4.12. The observed (black) and synthetic (red) tsunami waveforms at far-field. The gray bars indicate the used time window for inversion.

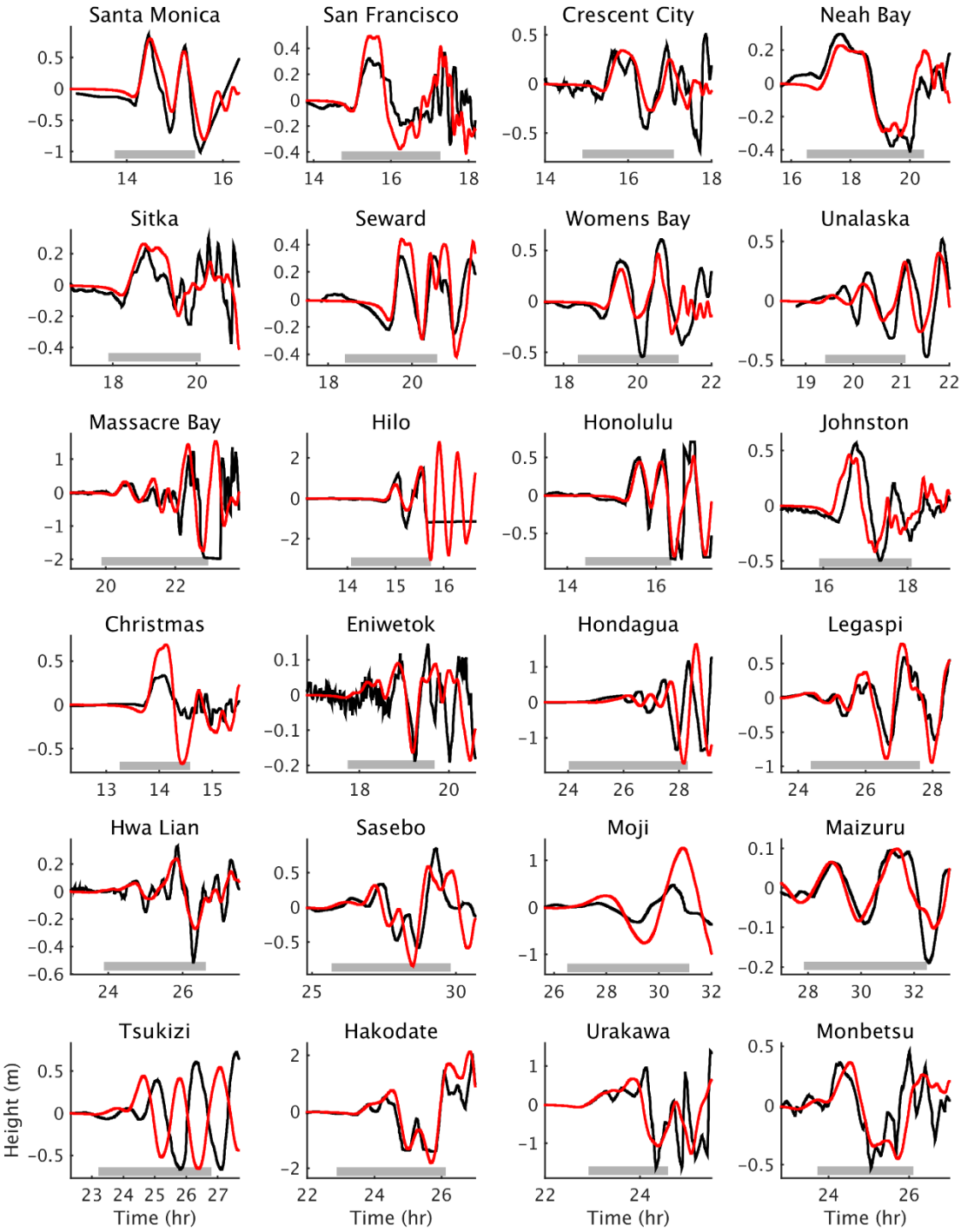

Figure 4.12. (Continued.) The observed (black) and synthetic (red) tsunami waveforms at far-field. The gray bars indicate the used time window for inversion.

With the OTA method, we well reproduced all observed waveforms (Figure 4.14 and Figure 4.15). In Figure 4.13, the observed coastal elevation and leveling data were also well reconstructed.

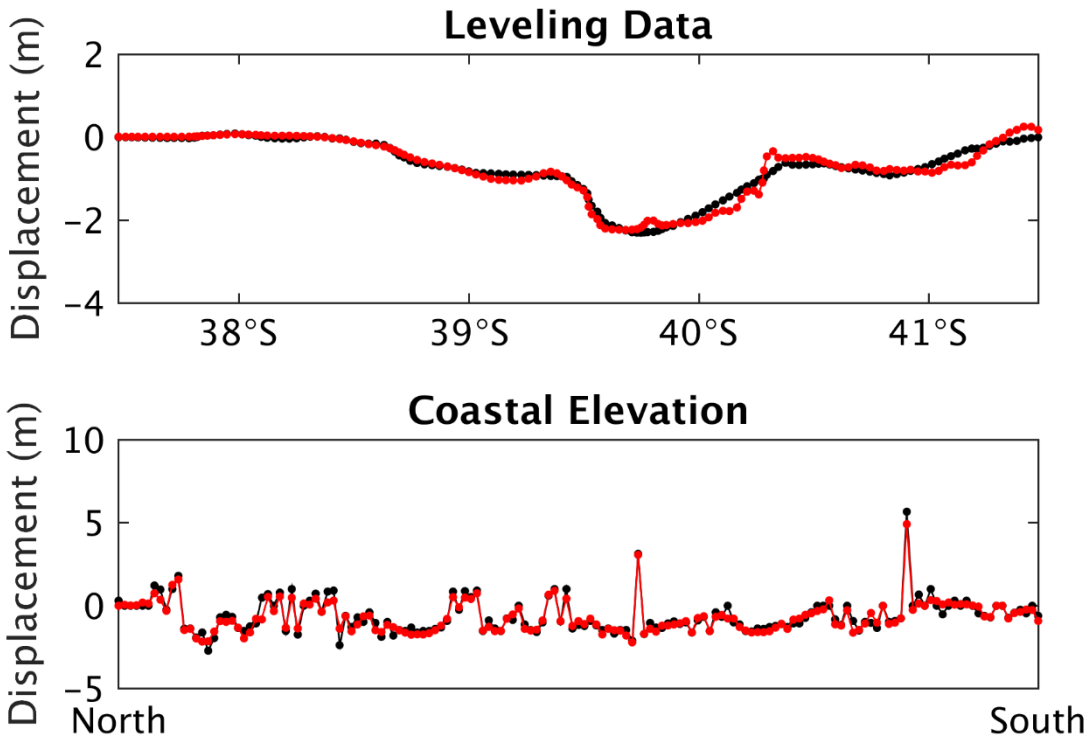

Figure 4.13. Coastal elevation and leveling data of observed (black) and synthetic (red).

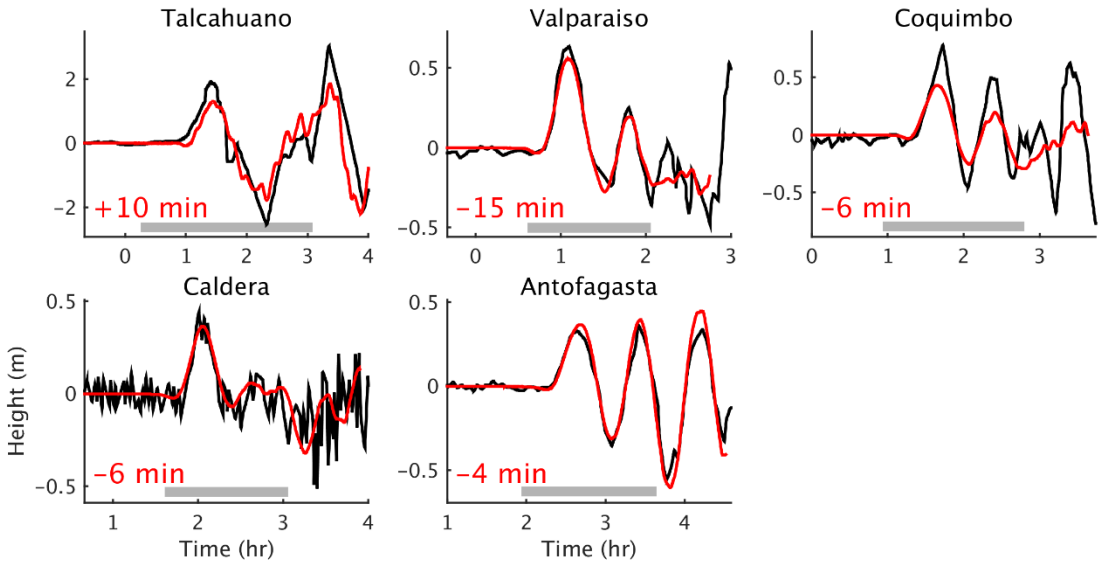

Figure 4.14. The observed (black) and synthetic (red) tsunami waveforms at near-field. The gray bars indicate the used time window for inversion. The red numbers at lower left corner indicate the estimated time shift by OTA.

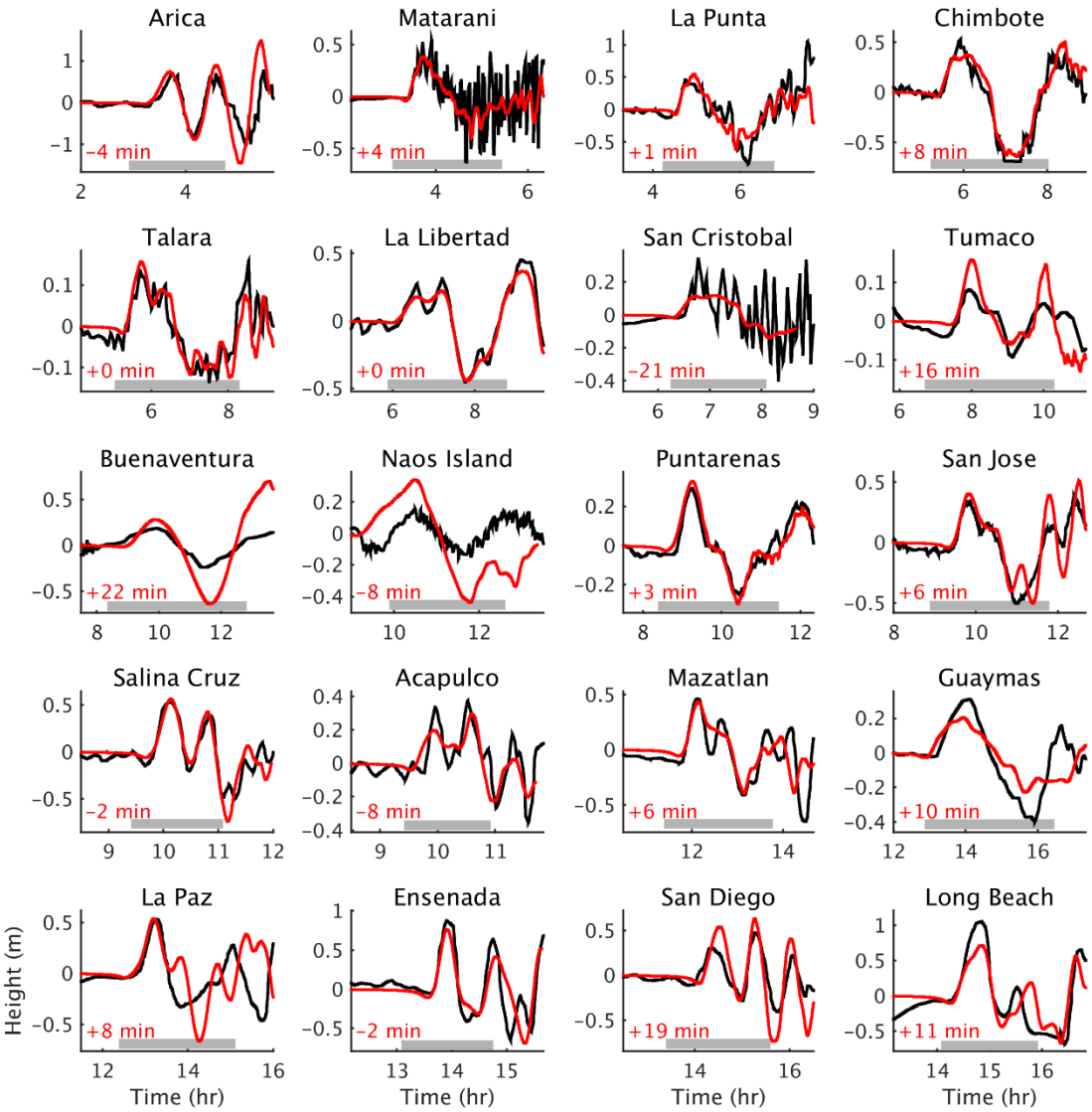

Figure 4.15. The observed (black) and synthetic (red) tsunami waveforms at far-field. The gray bars indicate the used time window for inversion. The red numbers at lower left corner indicate the estimated time shift by OTA.

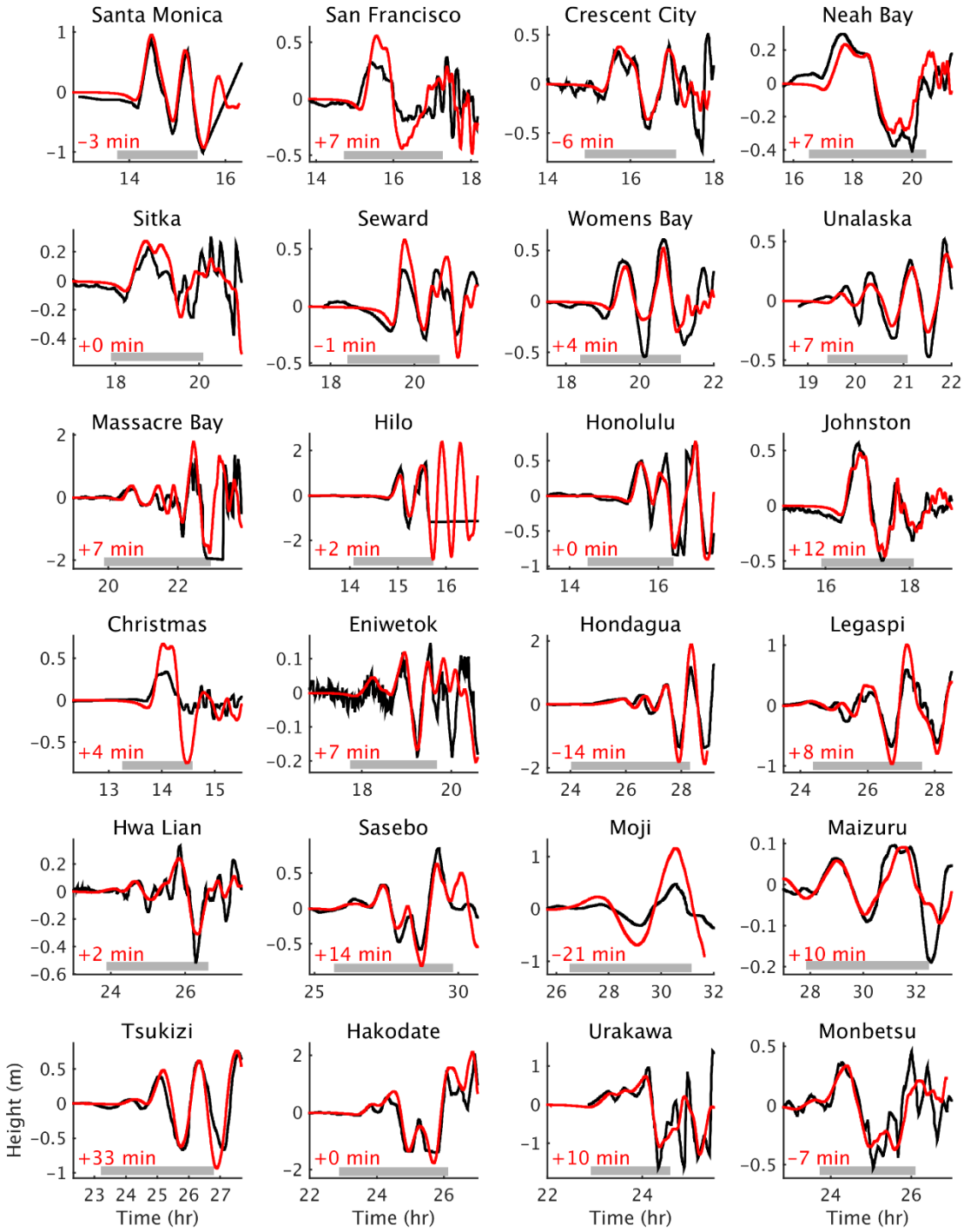

Figure 4.15. (Continued.) The observed (black) and synthetic (red) tsunami waveforms at far-field. The gray bars indicate the used time window for inversion. The red numbers at lower left corner indicate the estimated time shift by OTA.

To prove the south patch contributed not only the geodetic data but also the tsunami waveforms, we compared the synthetic waves from patches of north+central to the waves from the south. The result showed that the south patch contributed to the later wave phase in some stations, e.g. Acapulco, Salina Cruz, Honolulu, and Eniwetok. (Figure 4.16).

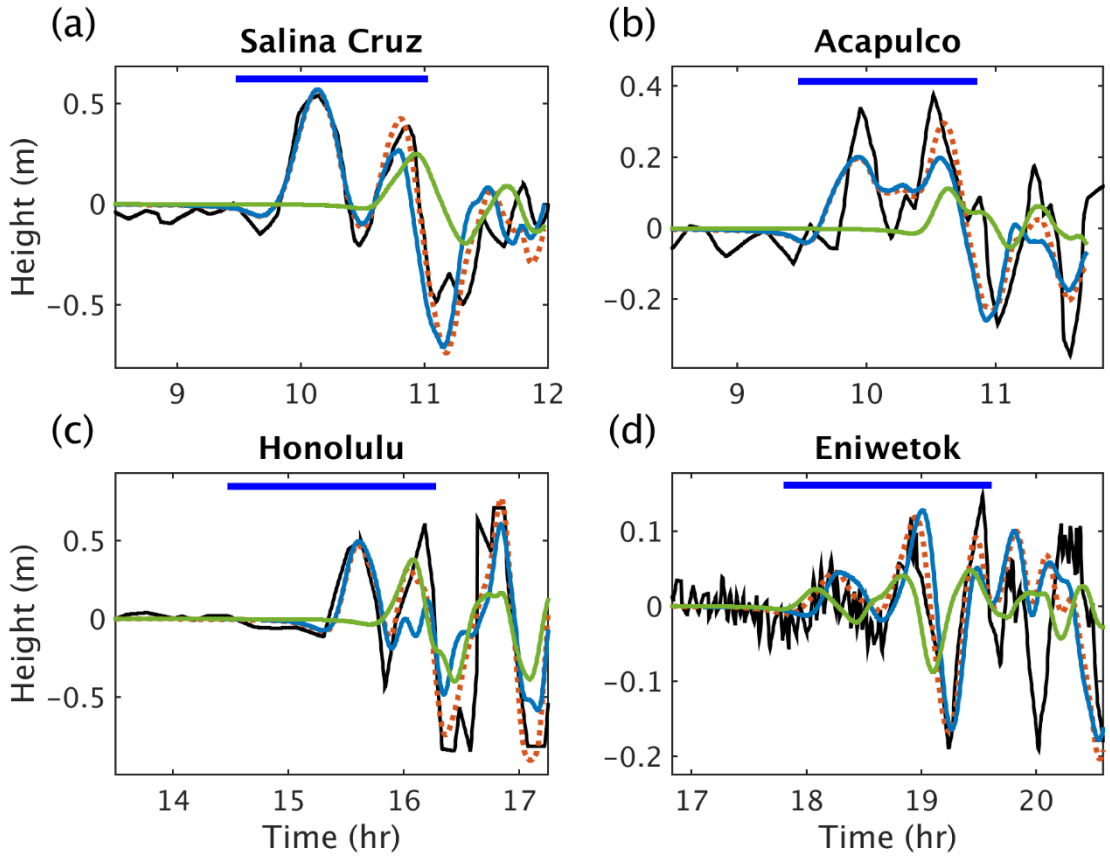

Figure 4.16. The observed (black) and synthetic waveforms (dotted red line), and the synthetic waveforms from the north+central patch (blue) and south patch (green) at far-field. The blue bars indicate the used time window for inversion.

4.5.2 The Slip Distribution

Because we used Gaussian shape initial sources to calculate the Green's functions, our inversion estimated the vertical displacement at the source area. To understand the slip distribution that caused the vertical displacement, we estimated the slip distribution on the fault plane by the estimated vertical displacement. We first created finite faults on the fault plane. The fault plane was based on the slab model 1.0 (USGS). Second, we calculated the vertical displacement corresponding to the to the finite fault (Okada, 1985). The rake angle was assumed to 90°. Finally, we applied the least square method to estimate the slip distribution of the finite faults.

Figure 4.17 shows the estimated slip distribution corresponding to the vertical displacement in Figure 4.10b. It shows a slip extended about 800 km from south of the epicenter to almost 46°S with a width of about 160 km. The peak slips are about 33 m at the north (40°S) and south asperity (45°S). And the asperity between 42°S to 44°S shows about 29 m slips.

We set the shear module following the slab parameter of Moreno et al. (2009) ($E = 120\text{Gpa}$, $\nu = 0.3$, and $\mu = 4.6 \times 10^{10}\text{Pa}$). The estimated moment is $1.27 \times 10^{23}\text{Nm}$, $Mw \approx 9.3$.

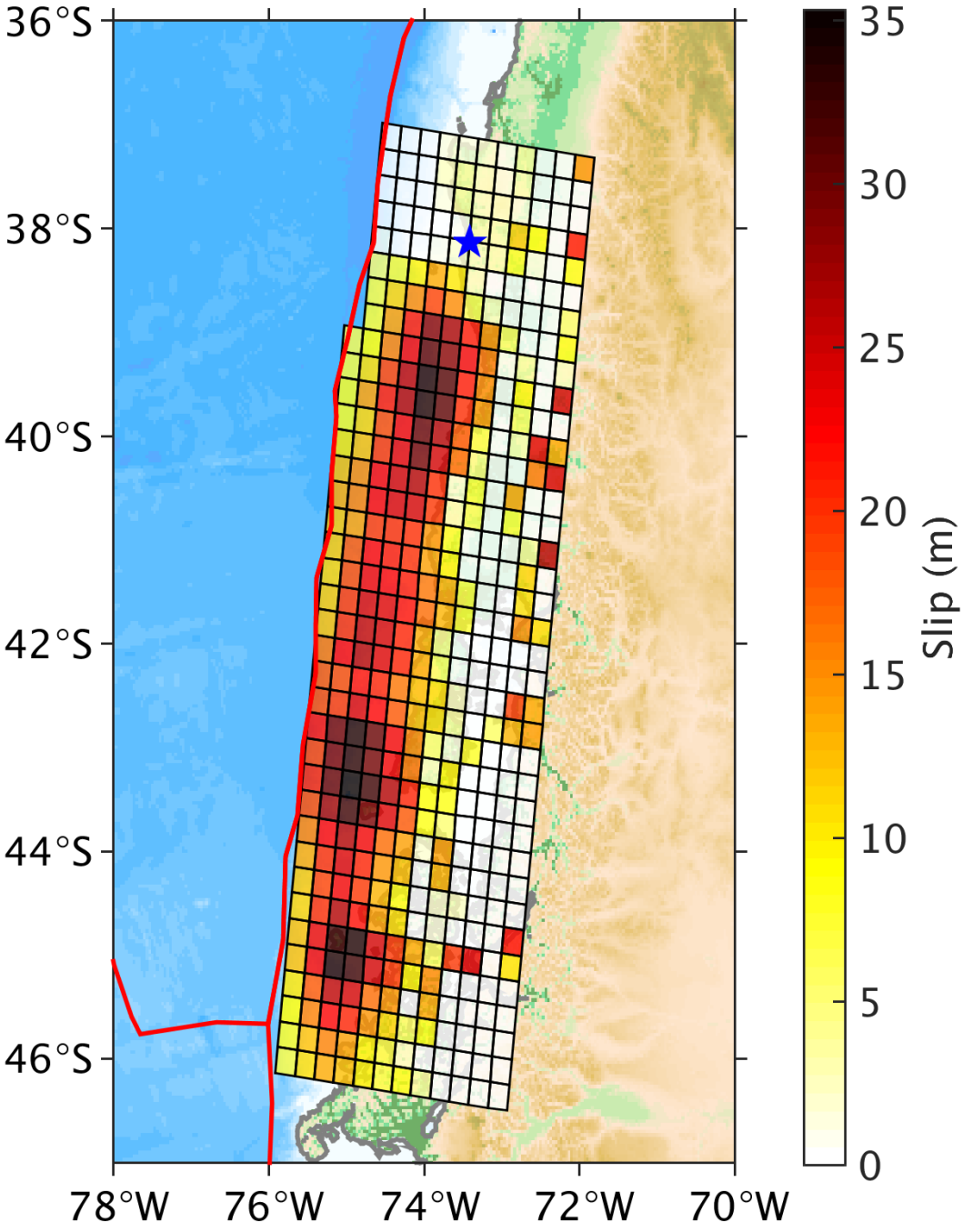

Figure 4.17. Slip distribution estimated from the inverted vertical displacement. The blue star shows the epicenter. The red lines represent the trenches.

4.6 Conclusions

We have re-estimated the source of the 1960 Chile earthquake by applying the joint inversion of near-field and far-field tsunami data and geodetic data. We list our conclusions as follows.

1. With the joint inversion of geodetic data and near-field and far-field tsunami data, the tsunami source, as well as the earthquake source, were well estimated in this study. We estimated a seismic moment 1.27×10^{23}Nm (Mw 9.3). It is slightly larger than the estimate of Barrientos and Ward (1990), Moreno et al. (2009), and Fujii and Satake (2013).
2. We have estimated three asperities. The south asperity caused the large vertical displacement at the south region, which contributed not only to the large coastal elevation at Guamblin Island but also to the high amplitude later phase of tsunami waveforms at some far-field stations (e.g., Honolulu).

We successfully inverted the source of the 1960 Chile earthquake using far-field tsunami waveforms. Previous studies indicate the slip concentrated at the shallow region of the slab (Barrientos and Ward, 1990; Moreno et al., 2009; Fujii and Satake, 2013). The offshore shallow slip caused the seafloor deformation and triggered the tsunami. We exploited the far-field tsunami data which provide supplementary information for estimating the seafloor deformation.

For the systematic arrival time discrepancy between the observed and computed waveforms, we applied the phase correction method (Watada et al., 2014; Ho et al., 2017). And we performed the OTA method (Romano et al., 2016) to solve the random arrival time discrepancy caused by instrumental inaccurate information (e.g. time or location), local effect, or unknown response. With those methods, we well inverted the tsunami waveforms and geodetic data. Slip distribution in the shallow region has also been well recovered.

Chapter 5

Summary

We have demonstrated the source estimation from transoceanic tsunami waveforms in the present study. We first derived the improved phase correction method and analyzed the contributions of our improvements. Then we validated the improved method by the 2011 Tohoku earthquake tsunami. After validation, we applied the improved method to recover the source of the 1960 Chile earthquake.

We list our conclusion as follows:

1. In Chapter 2, we have improved the accuracy of the existing phase correction method. The improved method corrects the LLW travel time by about 1.5% at the far-field station, and the existing method accounts for 1.1% (about 73 percent of the 1.5% correction). Besides, the new considered effects of ocean density stratification, actual ray path, and actual bathymetry, contribute to about 13, 4.5, and 9.5 percent, respectively.
2. In Chapter 3, we have validated the improved method and the application of far-field tsunami data by the 2011 Tohoku earthquake tsunami. We performed single and multiple time window inversion using different datasets (near-field, far-field, and all) and corrected by different methods (non-corrected, original method, and improved method). The results show that the far-field data provide a very long period, smoothed source information. However, without detailed source information, the improvement is limited when performing multiple time window inversion with only far-field data.
3. We have proved the improved method provides more accurate results for source inversion and forward prediction. We applied the improved method to forward

simulation, and it shows more accurate predictions at both near-field and far-field tsunami gauges, as well as satellite altimeter data.

4. In Chapter 4, we have estimated the source of the 1960 Chile earthquake by inverting the geodetic data, near-field tsunami data and far-field tsunami data. We have recovered more source information using far-field tsunami waveforms. The south asperity explained the large coastal elevation at Guamblin Island as well as the high amplitude later phase of tsunami waveform in Honolulu. Our estimate shows a moderate magnitude of Mw 9.4 among the studies about this earthquake.

We have shown that the far-field tsunami data provide supplementary source information. And we are able to exploit this information as we solve the arrival time discrepancy problems. In our inversion method, both systematic and random arrival time discrepancies were solved.

Our study reveals the advantage of far-field data. We have demonstrated a common process of applying far-field tsunami data in source inversion as well as waveform prediction. We aim to provide a reference for who may want to use far-field tsunami data to study a tsunami source or for who want to perform tsunami predictions or forecasts for distant locations.

Some topics should be discussed as future works. We successfully recovered the tsunami source by inverting only far-field data in Chapter 3. However, the position of recovered tsunami source was slightly shifted from the one by near-field data. The small inaccuracy in far-field stations may explain this problem. Watada et al. (2014) mentioned the elliptic Earth and the smaller gravity in the equatorial region cause a delay of a few minutes. This may explain the small inaccuracy in the very far-field stations. Besides, we calculated the ray path using LLW theory. However, the ray paths should be slightly frequency-dependent. Those small effects should be included to accomplish a more accurate prediction.

Chapter 6 References

Allgeyer, S., & Cummins, P. (2014). Numerical tsunami simulation including elastic loading and seawater density stratification. *Geophysical Research Letters*, 41(7), 2368-2375. http://doi.org/10.1002/2014GL059348

An, C., & Liu, P. L. (2016). Analytical solutions for estimating tsunami propagation speeds. *Coastal Engineering*, 117, 44-56.

Audet, C., & Dennis Jr, J. E. (2006). Mesh adaptive direct search algorithms for constrained optimization. *SIAM Journal on optimization*, 17(1), 188-217.

Audet, C., Le Digabel, S., & Tribes, C. (2009). NOMAD user guide. Technical Report G-2009-37, Les cahiers du GERAD.

Baba, T., Takahashi, N., Kaneda, Y., Ando, K., Matsuoka, D., & Kato, T. (2015). Parallel implementation of dispersive tsunami wave modeling with a nesting algorithm for the 2011 Tohoku tsunami. *Pure and Applied Geophysics*, 172(12), 3455-3472. http://doi.org/10.1007/s00024-015-1049-2

Barrientos, S. E., & Ward, S. N. (1990). The 1960 Chile earthquake: inversion for slip distribution from surface deformation. *Geophysical Journal International*, 103(3), 589-598.

Berkman, S. C., & Symons, J. M. (1964). The tsunami of May 22, 1960 as recorded at tide stations, U. S. Department of Commerce, *Coast and Geodetic Survey*, pp. 79.

Boyer, T. P., & S. Levitus (Ed.) (2009). World Ocean Database 2009., NOAA Atlas NESDIS 66, U.S. Gov. Printing Office, Wash. D.C., 216 pp., DVD.

Cifuentes, I. L., & Silver, P. G. (1989). Low-frequency source characteristics of the great 1960 Chilean earthquake. *Journal of Geophysical Research: Solid Earth*, 94(B1), 643-663.

Dziewonski, A. M., & Anderson, D. L. (1981). Preliminary reference Earth model. *Physics of the earth and planetary interiors*, 25(4), 297-356.

Eblé, M. C., Mungov, G. T., & Rabinovich, A. B. (2015). On the leading negative phase of major 2010–2014 tsunamis. *Pure and Applied Geophysics*, 172(12), 3493-3508. https://doi.org/10.1007/s00024-015-1127-5

Fujii, Y., & Satake, K. (2013). Slip distribution and seismic moment of the 2010 and 1960 Chilean earthquakes inferred from tsunami waveforms and coastal geodetic data. *Pure and Applied Geophysics*, 170(9-10), 1493-1509.

Fujii, Y., Satake, K., Sakai, S. I., Shinohara, M., & Kanazawa, T. (2011). Tsunami source of the 2011 off the Pacific coast of Tohoku Earthquake. *Earth, planets and space*, 63(7), 55. http://doi.org/10.5047/eps.2011.06.010

Gusman, A. R., Murotani, S., Satake, K., Heidarzadeh, M., Gunawan, E., Watada, S., & Schurr, B. (2015). Fault slip distribution of the 2014 Iquique, Chile, earthquake estimated from ocean-wide tsunami waveforms and GPS data. *Geophysical Research Letters*, 42(4), 1053-1060. http://doi.org/10.1002/2014GL062604

Gusman, A. R., Mulia, I. E., Satake, K., Watada, S., Heidarzadeh, M., & Sheehan, A. F. (2016). Estimate of tsunami source using optimized unit sources and including dispersion effects during tsunami propagation: The 2012 Haida Gwaii earthquake. *Geophysical Research Letters*, 43(18), 9819-9828.

Gusman, A. R., Tanioka, Y., Sakai, S., & Tsushima, H. (2012). Source model of the great 2011 Tohoku earthquake estimated from tsunami waveforms and crustal deformation data. *Earth and Planetary Science Letters*, 341, 234-242. http://doi.org/10.1016/j.epsl.2012.06.006

Ho, T.-C., Satake, K., & Watada, S. (2017). Improved phase corrections for transoceanic tsunami data in spatial and temporal source estimation: Application to the 2011 Tohoku earthquake. *Journal of Geophysical Research: Solid Earth*, 122, 10,155–10,175. https://doi.org/10.1002/2017JB015070

Hossen, M. J., Cummins, P. R., Dettmer, J., & Baba, T. (2015). Tsunami waveform inversion for sea surface displacement following the 2011 Tohoku earthquake: Importance of dispersion and source kinematics. *Journal of Geophysical Research: Solid Earth*, 120(9), 6452-6473. http://doi.org/10.1002/2015JB011942

Ide, S., Baltay, A., & Beroza, G. C. (2011). Shallow dynamic overshoot and energetic deep rupture in the 2011 Mw 9.0 Tohoku-Oki earthquake. *Science*, 332(6036), 1426-1429.

Imamura, F., Nagano, O., Goto, T., & Shuto, N. (1987). Trans-oceanic tsunami propagation computation for the 1960 Chilean tsunami [in Japanese]. *Proc. Coast. Eng.*, 34, 172–176.

Imamura, F., Shuto, N., & Goto, C. (1990). Study on numerical simulation of the Transoceanic propagation of tsunami Part 2: Characteristics of tsunami propagating over the Pacific [in Japanese]. *Zisin*, 43, 389–402.

Jacob, K. H. (1970). Three-dimensional seismic ray tracing in a laterally heterogeneous spherical Earth. *Journal of Geophysical Research*, 75(32), 6675-6689.

Kanamori, H., & Anderson, D. L. (1975). Amplitude of the Earth's free oscillations and long-period characteristics of the earthquake source. *Journal of Geophysical Research*, 80(8), 1075-1078.

Kanamori, H., & Cipar, J. J. (1974). Focal process of the great Chilean earthquake May 22, 1960. *Physics of the Earth and Planetary Interiors*, 9(2), 128-136.

Kato, T., Terada, Y., Nishimura, H., Nagai, T., & Koshimura, S. I. (2011). Tsunami records due to the 2010 Chile Earthquake observed by GPS buoys established along the Pacific coast of Japan. *Earth, Planets and Space*, 63(6), e5-e8. http://doi.org/10.5047/eps.2011.05.001

Kawai, H., Satoh, M., Kawaguchi, K., & Seki, K. (2012). Recent tsunamis observed by GPS buoys off the Pacific coast of Japan. *Coastal engineering proceedings*, 1(33), 1. http://doi.org/10.9753/icce.v33.currents.1

Koketsu, K. (1991). Three-dimensional ray tracing in a subduction zone. *Journal of the Seismological Society of Japan*, 44, 165-176. In Japanese.

Koketsu, K., & Sekine, S. (1998). Pseudo-bending method for three-dimensional seismic ray tracing in a spherical earth with discontinuities. *Geophysical Journal International*, 132(2), 339-346.

Koketsu, K., Yokota, Y., Nishimura, N., Yagi, Y., Miyazaki, S. I., Satake, K., ... & Okada, T. (2011). A unified source model for the 2011 Tohoku earthquake. *Earth and Planetary Science Letters*, 310(3-4), 480-487.

Lay, T., & Wallace, T. C. (1995). Modern global seismology (Vol. 58). Academic press, San Diego, Calif.

Liu, P. L.-F. (2009), Tsunami modeling: Propagation, in The Sea, vol. 15, Tsunamis, edited by E. Bernard et al., chap. 3, pp. 295–320, Harvard Univ. Press, Cambridge, Mass.

Le Digabel, S. (2011). Algorithm 909: NOMAD: Nonlinear optimization with the MADS algorithm. *ACM Transactions on Mathematical Software (TOMS)*, 37(4), 44. https://doi.org/10.1145/1916461.1916468

McDougall, T. J., & Barker, P. M. (2011). Getting started with TEOS-10 and the Gibbs Seawater (GSW) oceanographic toolbox. SCOR/IAPSO WG, 127, 1-28, ISBN 978-0-646-55621-5.

Moreno, M. S., Bolte, J., Klotz, J., & Melnick, D. (2009). Impact of megathrust geometry on inversion of coseismic slip from geodetic data: Application to the 1960 Chile earthquake. *Geophysical Research Letters*, 36(16).

Mori, N., Takahashi, T., Yasuda, T., & Yanagisawa, H. (2011). Survey of 2011 Tohoku earthquake tsunami inundation and run-up. *Geophysical research letters*, 38(7). http://doi.org/10.1029/2011GL049210

Nishimura, T., Munekane, H., & Yarai, H. (2011). The 2011 off the Pacific coast of Tohoku Earthquake and its aftershocks observed by GEONET. *Earth, planets and space*, 63(7), 22. http://doi.org/10.5047/eps.2011.06.025

Okada, Y. (1985). Surface deformation due to shear and tensile faults in a half-space. *Bulletin of the seismological society of America*, 75(4), 1135-1154.

Okal, E. A. (1982). Mode-wave equivalence and other asymptotic problems in tsunami theory. *Phys. Earth Planet. Inter.*, 30, 1–11.

Pereyra, V. W. H. K., Lee, W. H. K., & Keller, H. B. (1980). Solving two-point seismic-ray tracing problems in a heterogeneous medium: Part 1. A general adaptive finite difference method. *Bulletin of the Seismological Society of America*, 70(1), 79-99.

Plafker, G., & Savage, J. C. (1970). Mechanism of the Chilean earthquakes of May 21 and 22, 1960. *Geological Society of America Bulletin*, 81(4), 1001-1030.

Rabinovich, A. B., Titov, V. V., Moore, C. W., & Ebl e, M. C. (2017). The 2004 Sumatra Tsunami in the Southeastern Pacific Ocean: New global insight from observations and modeling. *Journal of Geophysical Research: Oceans*, 22. https://doi.org/ 10.1002/2017JC013078

Rabinovich, A. B., Woodworth, P. L., & Titov, V. V. (2011). Deep-sea observations and modeling of the 2004 Sumatra tsunami in Drake Passage. *Geophysical Research Letters*, 38(16). http://doi.org/10.1029/2011GL048305

Romano, F., Piatanesi, A., Lorito, S., Tolomei, C., Atzori, S., & Murphy, S. (2016). Optimal time alignment of tide-gauge tsunami waveforms in nonlinear inversions: Application to the 2015 Illapel (Chile) earthquake. *Geophysical Research Letters*, 43(21). https://doi.org/10.1002/2016GL071310

Saito, T., Matsuzawa, T., Obara, K., & Baba, T. (2010). Dispersive tsunami of the 2010 Chile earthquake recorded by the high-sampling-rate ocean-bottom pressure gauges. *Geophysical Research Letters*, 37(23).

Saito, T., Satake, K., & Furumura, T. (2010). Tsunami waveform inversion including dispersive waves: the 2004 earthquake off Kii Peninsula, Japan. *Journal of Geophysical Research: Solid Earth*, 115(B6).

Satake, K. (1987). Inversion of tsunami waveforms for the estimation of a fault heterogeneity: Method and numerical experiments. *Journal of Physics of the Earth*, 35(3), 241-254. http://doi.org/10.4294/jpe1952.35.241

Satake, K. (1988). Effects of bathymetry on tsunami propagation: Application of ray tracing to tsunamis. *Pure and Applied Geophysics*, 126(1), 27-36.

Satake, K. (1995). Linear and nonlinear computations of the 1992 Nicaragua earthquake tsunami. *Pure and Applied Geophysics*, 144(3-4), 455-470.

Satake, K., Baba, T., Hirata, K., Iwasaki, S. I., Kato, T., Koshimura, S., ... & Terada, Y. (2005). Tsunami source of the 2004 off the Kii Peninsula earthquakes inferred from offshore tsunami and coastal tide gauges. *Earth, planets and space*, 57(3), 173-178. http://doi.org/10.1186/BF03351811

Satake, K., Fujii, Y., Harada, T., & Namegaya, Y. (2013). Time and space distribution of coseismic slip of the 2011 Tohoku earthquake as inferred from tsunami waveform data. *Bulletin of the seismological society of America*, 103(2B), 1473-1492. http://doi.org/10.1785/0120120122

Shao, G., Li, X., Ji, C., & Maeda, T. (2011). Focal mechanism and slip history of the 2011 M w 9.1 off the Pacific coast of Tohoku Earthquake, constrained with teleseismic body and surface waves. *Earth, planets and space*, 63(7), 9.

Simons, M., Minson, S. E., Sladen, A., Ortega, F., Jiang, J., Owen, S. E., ... & Helmberger, D. V. (2011). The 2011 magnitude 9.0 Tohoku-Oki earthquake: Mosaicking the megathrust from seconds to centuries. *science*, 332(6036), 1421-1425. http://doi.org/10.1126/science.1206731

Song, Y. T., Fukumori, I., Shum, C. K., & Yi, Y. (2012). Merging tsunamis of the 2011 Tohoku-Oki earthquake detected over the open ocean. *Geophysical Research Letters*, 39(5). http://doi.org/10.1029/2011GL050767

Talley, L. D., G. L. Pickard, W. J. Emery, and J. H. Swift (2011), Descriptive Physical Oceanography: An Introduction, 6th ed., Academic Press, London.

Tang, L., Titov, V. V., Bernard, E. N., Wei, Y., Chamberlin, C. D., Newman, J. C., ... & Uslu, B. (2012). Direct energy estimation of the 2011 Japan tsunami using deep-

ocean pressure measurements. *Journal of Geophysical Research: Oceans*, 117(C8). http://doi.org/10.1029/2011JC007635

Tappin, D. R., Grilli, S. T., Harris, J. C., Geller, R. J., Masterlark, T., Kirby, J. T., ... & Mai, P. M. (2014). Did a submarine landslide contribute to the 2011 Tohoku tsunami?. *Marine Geology*, 357, 344-361.

Tsai, V. C., Ampuero, J. P., Kanamori, H., & Stevenson, D. J. (2013). Estimating the effect of Earth elasticity and variable water density on tsunami speeds. *Geophysical Research Letters*, 40(3), 492-496. http://doi.org/10.1002/grl.50147

Um, J., & Thurber, C. (1987). A fast algorithm for two-point seismic ray tracing. *Bulletin of the Seismological Society of America*, 77(3), 972-986.

Yoshimoto, M., Watada, S., Fujii, Y., & Satake, K. (2016). Source estimate and tsunami forecast from far-field deep-ocean tsunami waveforms—The 27 February 2010 Mw 8.8 Maule earthquake. *Geophysical Research Letters*, 43(2), 659-665. http://doi.org/10.1002/2015GL067181

Tsushima, H., Hino, R., Tanioka, Y., Imamura, F., & Fujimoto, H. (2012). Tsunami waveform inversion incorporating permanent seafloor deformation and its application to tsunami forecasting. *Journal of Geophysical Research: Solid Earth*, 117(B3). http://doi.org/10.1029/2011JB008877

Watada, S. (2013). Tsunami speed variations in density-stratified compressible global oceans. *Geophysical Research Letters*, 40(15), 4001-4006.

Watada, S., & Kanamori, H. (2010). Acoustic resonant oscillations between the atmosphere and the solid earth during the 1991 Mt. Pinatubo eruption. *Journal of Geophysical Research: Solid Earth*, 115(B12).

Watada, S., Kusumoto, S., & Satake, K. (2014). Traveltime delay and initial phase reversal of distant tsunamis coupled with the self-gravitating elastic Earth. *Journal of Geophysical Research: Solid Earth*, 119(5), 4287-4310.

Weatherall, P., Marks, K. M., Jakobsson, M., Schmitt, T., Tani, S., Arndt, J. E., ... & Wigley, R. (2015). A new digital bathymetric model of the world's oceans. *Earth and Space Science*, 2(8), 331-345. http://doi.org/10.1002/2015EA000107

Woods, M. T., & Okal, E. A. (1987). Effect of variable bathymetry on the amplitude of teleseismic tsunamis: A ray-tracing experiment. *Geophysical Research Letters*, 14(7), 765-768. https://doi.org/10.1029/GL014i007p00765